TURBULENCE AND MASS MOTION IN GALACTIC MOLECULAR CLOUDS

Thesis by
Stephen Morris Lichten

In Partial Fulfillment of the Requirements
for the Degree of
Doctor of Philosophy

California Institute of Technology
Pasadena, California

1984
(Submitted August 5, 1983)

to Marsha

ACKNOWLEDGEMENTS

My advisor, Peter Wannier, first introduced me to the field of millimeterwave radio astronomy, and I am indebted to him for the many observational and analytical techniques he taught me, as well as for his guidance with this thesis. Chapter 1 originated from a study of line profiles I undertook at his suggestion, and Chapters 4 and 5 grew out of questions I pondered largely because of the work we did together in Chapter 3. It was easy to be inspired by his enthusiasm and energetic approach to research. I will always admire his scientific achievements and value his friendship highly.

The following Caltech faculty and staff are especially thanked for their indefatigable efforts towards building three exceptionally high quality 10m radio telescopes at Owens Valley, where I took many of my observations: Robert Leighton, Tom Phillips, Dave Woody (receivers), Colin Masson (spectrometers), and Steve Scott (computers). I am also grateful to George Seielstad, on-site supervisor at Owens Valley, and to the rest of the OVRO staff for their efforts on my behalf. In the Caltech computing facilities in Pasadena, Tim Pearson and Mike Lesser gave me assistance many times.

At the NRAO 12m site on Kitt Peak Mountain, I thank Rick Howard and the four observers -- Rosalie Douglas, Werner Scharlach, Calvin Sparks, and John Weaver -- for ensuring that my observing runs turned out so successfully. I am particularly indebted to Mark Gorden, director of NRAO Tucson operations, for arranging for me to make crucial observations in 1982 and 1983.

Ron Maddelena, Patrick Thaddeus, and Mark Morris graciously made available to me their coarse-resolution maps of the Orion Molecular Cloud prior to publication. These data provided me with vital large-scale coverage of this source.

Discussions I had with Al Wootten and Anneila Sargent were very helpful while I was writing Chapters 1 and 2, and Peter Goldreich helped me a great deal with some of the issues relating to shock waves and turbulence in Chapter 5. Many of my ideas grew from informal conversations I had at Caltech with other students and faculty and from the many colloquia, seminars, and journal club gatherings I attended. I would like to thank these people collectively here, since they are too numerous to name, for surrounding me with a rich, stimulating atmosphere conducive to creative research.

The financial support for this dissertation was generously provided by the National Science Foundation, several Caltech teaching and research fellowships, and scholarships from ARCS Foundation and the J. Gimbel Estate.

I thank my parents, Bill and Susan, and the rest of my family, for many years of encouragement, moral support, and sacrifice. And finally, I wish to thank my wife, Marsha, for her love, companionship and patience, and for making the past five years as wonderful as they have been.

ABSTRACT

The main subject of this thesis is the origin and maintenance of supersonic gas motions in dense molecular clouds.

In Chapters 1 and 2, we interpret and model millimeter wavelength CO line profiles whose broad wings and self-reversals provide clues about the nature of the observed supersonic motions. Broad molecular line wings provide evidence for high-velocity bipolar gas flows powered by strong stellar winds. The self-reversed CO line profiles are due in part to radiative transfer effects in molecular clouds which, in some cases, are expanding or contracting; Monte Carlo simulations of radiative transfer, however, demonstrate that cloud fragmentation may be responsible for some observed properties of the line profiles. The detection of broad-wing sources in quiescent, dark nebulae, shows that energetic outflows are common in a wide range of molecular clouds.

In Chapter 3, our high resolution maps of molecular and atomic line emission across molecular cloud edges show that these clouds are embedded in warm H I halos which appear in emission against the galactic H I background. We also find that molecular cloud internal motions may be correlated with the H I halo temperature; however, the halo masses are much less than those of the molecular clouds and exert only a limited influence on internal cloud kinematics.

The statistical and autocorrelation analyses of Chapters 4 and 5 show that molecular clouds are clumpy and contain hundreds of turbulent fragments whose relative velocities are supersonic, but whose internal velocity dispersions are not. Shock dissipation processes, clump collisions, and gas compression have major roles in molecular cloud kinematics. Our observations indicate that turbulent energy is supplied at small scales, as opposed to the dissipationless energy transfer from large to small scales which is known to occur in incompressible fluids with high Reynolds numbers. Energetic outflows from embedded young stars may break apart, fragment, and compress portions of molecular clouds, and may be capable of originating and sustaining the supersonic turbulence. Additional observational and theoretical studies of cloud clumpiness and of the rate of energy transfer from stellar outflows to ambient molecular material, are required before this mechanism for cloud support can be evaluated.

TABLE OF CONTENTS

Dedication ii

Acknowledgements iii

Abstract v

Introduction 1

Chapter 1: CARBON MONOXIDE BROAD WINGS AND SELF-REVERSALS IN NGC 2071 5

Chapter 2: HIGH-VELOCITY MOLECULAR GAS IN THE DARK CLOUD L1529 .. 14

Chapter 3: WARM H I HALOS AROUND MOLECULAR CLOUDS 19

Chapter 4: AUTOCORRELATION MEASUREMENTS OF INTENSITY FLUCTUATIONS IN MOLECULAR CLOUDS 35

Chapter 5: VELOCITY FLUCTUATIONS AND TURBULENCE IN MOLECULAR CLOUDS 129

INTRODUCTION

Big whirls have little whirls,
That feed on their velocity;
And little whirls have lesser whirls,
And so on to viscosity.

This rhyme, attributed to L.F. Richardson and recited by S. Chandrasekhar in the Third Henry Norris Russell Lecture of the American Astronomical Society (Ottawa, Canada, June 21, 1949), expresses the basic concepts of the theory of turbulence which was first mathematically described by A.N. Kolmogoroff in the early 1940s.

In the context of hydrodynamics and fluid mechanics, the word turbulence refers to extremely irregular and complex motions of fluid elements in which inertial forces dominate. Because of the complicated and random nature of the motions, the influence of initial conditions disappears and an equilibrium situation results which can be meaningfully described only in statistical terms. The hierarchy of turbulent eddies alluded to above, through which turbulent energy is transferred from large to small scales, can be shown to exist by a simple dimensional analysis, provided the fluid is incompressible and velocities are subsonic. Turbulence of this kind has been confirmed both in the laboratory and in various natural situations, such as portions of the earth's atmosphere.

There have been numerous astrophysical situations in which turbulence has been suggested to play an important role. In most cases, turbulence has been invoked to explain an unresolved velocity dispersion in excess of that attributable directly to thermal motions. Examples are motions observed in the sun, stellar atmospheres, interplanetary matter, galactic atomic hydrogen, and even extragalactic motions.

There are two ways of using the term turbulence in connection with measured velocity dispersions: in the first, turbulence is simply a label for an aspect of the observations which the astronomer does not understand and cannot explain. In the second, the term turbulence is used to attribute specific physical and statistical properties -- most often those of the incompressible Kolmogoroff turbulence -- to the source being observed. The former conveys no information about physical processes in the source, while the latter most assuredly does.

Since the 1970s, the CO ($^{12}C^{16}O$) molecule, and its less abundant isotopes (^{13}CO, $C^{18}O$, $C^{17}O$, and $^{13}C^{18}O$) have proved to be very revealing probes of physical conditions in dense molecular clouds and regions of star formation. The line widths of millimeterwave CO rotational spectra, however, are universally in the 2-5 km s^{-1} range, typically more than an order of magnitude greater than the thermal or sonic speeds of the molecular gas. The molecular gas temperature is one of the better determined quantities in millimeterwave molecular spectroscopy, and it has been confirmed by measurements of multiple transitions of several different molecules (such as CO and NH_3) as well as by far-infrared observations. The kinetic temperatures for most molecular clouds are 10-50 K. This has led to a long-standing debate over whether the highly supersonic velocities could be attributed to turbulence or to large scale mass motions. Most of the early discussions of turbulence in molecular clouds simply referred to an unresolved small-scale random pattern of gas motions; because there was no known physical mechanism to power this supersonic motion , the turbulent hypothesis was heavily criticized. On the other hand, most large-scale mass motions in molecular clouds were attributed to gravitational collapse, which was in contradiction to the observed rate of star formation and to longevity of molecular clouds inferred from observations and theory. The central question which this dissertation addresses is the nature of the universally observed supersonic motions in molecular clouds.

This dissertation is based primarily on molecular spectral line observations at 1-4 mm wavelength which were specifically planned to distinguish between random, ordered, small-scale, and large-scale motions. The aim was not simply to characterize the observed motions, but mainly to determine their origin and energy source. Each of the five chapters was written as an article to be submitted separately to a scientific journal. The first three chapters have been published in The Astrophysical Journal (Ap.J.) and are printed here in their entirety. In Chapters 1 and 2, the CO spectral line shapes were examined for clues as to the nature of the supersonic velocity dispersion. Various effects were identified and attributed to large scale radial motion, cloud fragmentation, an unresolved random turbulent component, and a small-scale collimated high velocity outflow presumably from young stellar objects. In Chapter 3, giant envelopes of atomic hydrogen surrounding molecular clouds were detected, providing a link between molecular cloud interiors and the larger scale atomic gas distribution in the Galaxy. In Appendix A of Chapter 3, the masses of the H I halos are estimated and their possible effects on molecular cloud kinematics are discussed.

In Chapters 4 and 5, we present correlation and statistical analyses of ^{13}CO intensity and line-of-sight velocity variations based on grids containing several hundred positions observed towards molecular clouds. Based on our results, we discuss and evaluate several possible mechanisms by which supersonic turbulence and cloud support can be maintained. The primary conclusion of this thesis is that molecular clouds generally are turbulent with various different kinds of motions superimposed. To a large degree, cloud fragments move in an apparently random pattern, although overall cloud contraction or expansion is present in some portions of the molecular clouds. Molecular cloud internal turbulence, however, is fundamentally different from the Kolmogoroff type of incompressible turbulence in which there is a dissipationless energy cascade from large to small scales due to inertial forces. Molecular cloud turbulence is highly supersonic and highly compressible, and we present the case for maintenance of such turbulence by energetic episodes of mass loss from stars located within the molecular clouds.

CHAPTER 1

CARBON MONOXIDE BROAD WINGS AND SELF-REVERSALS IN NGC 2071

Reprinted from The Astrophysical Journal, 253, 593 (1982)

THE ASTROPHYSICAL JOURNAL, 253:593–600, 1982 February 15 -6-

CARBON MONOXIDE BROAD WINGS AND SELF-REVERSALS IN NGC 2071

STEPHEN M. LICHTEN
Owens Valley Radio Observatory, California Institute of Technology

Received 1981 June 4; accepted 1981 August 24

ABSTRACT

We report and analyze CO spectra of NGC 2071 which exhibit broad wings and prominent self-reversed line profiles. These wings provide evidence for high-velocity bipolar gas flow powered by a strong stellar wind along the axis of a disk. The self-reversed line profiles are due in part to radiative transfer effects in the main body of the cloud, which may be contracting; however, a significant amount of self-absorption also originates in cooler foreground gas at the cloud periphery.

Subject headings: interstellar: molecules — masers — nebulae: individual — nebulae: reflection

I. INTRODUCTION

NGC 2071 is a bright reflection nebula in the northeast portion of the Orion molecular cloud complex and is associated with the I Orionis OB stellar association. At the position of an H_2O maser and a dramatically variable class 1 OH maser (Pankonin, Winnberg, and Booth 1977 and references therein), the ^{12}CO line profiles exhibit unusually broad wings and prominent self-reversals. Two weak radio continuum sources near a central infrared source have been detected by Bally (1981) with the VLA. The CO observations reported here were made in conjunction with a study of turbulence, mass motion, and kinematics in molecular clouds. The unusual CO velocity structure in NGC 2071 is particularly interesting because it may demonstrate the interaction between a molecular cloud and young, embedded stellar objects. Studies of such regions will shed light on the role of molecular clouds in the formation and evolution of stars.

II. OBSERVATIONAL TECHNIQUES

The CO observations were taken between 1980 January and 1981 January with two of the Caltech 10.4 m antennae at the Owens Valley Radio Observatory in Big Pine, California. The central regions of NGC 2071 were mapped in the ^{12}CO($J=1$–0) and ^{13}CO($J=1$–0) rotational transitions at 115 and 110 GHz. In addition, a spectrum was taken at 220 GHz of the ^{13}CO($J=2$–1) line at one position.

The ^{13}CO($J=2$–1) line was observed with a liquid-helium–cooled InSb heterodyne bolometer detector mounted at the Cassegrain focus. A spectrum was obtained by stepping the local oscillator frequency with a 0.4 MHz filter. The ^{12}CO($J=1$–0) spectra were taken with a room temperature receiver also mounted at the Cassegrain focus using a 512 channel autocorrelator at 25 MHz bandwidth. The ^{13}CO($J=1$–0) spectra were taken with a liquid-helium–cooled superconducting-insulating-superconducting (SIS) tunnel junction receiver (Phillips *et al.* 1981*b*) mounted in a sidecab below and to the side of the Cassegrain focus. The back end used with the SIS receiver was an acousto-optic spectrometer designed by Masson (1980) with a 100 MHz bandwidth and 512 channels. Table 1 summarizes the observational techniques used for the data presented in this paper. In all cases, position switching was used to eliminate sky background and instrumental noise; the reference position was tested for any detectable signal and none was found. The values of antenna temperature, T_A^*, given in this paper have been corrected for the atmosphere and include a correction for beam and spillover efficiency as given in Table 1.

III. OBSERVATIONS

Figure 1 displays the ^{12}CO and ^{13}CO($J=1$–0) spectra mapped in NGC 2071. The on source position is at $\alpha(1950)=05^h44^m30\overset{s}{.}3$, $\delta(1950)=00°20'18''$. Figure 2 shows three spectra in more detail at the position $(\Delta\alpha, \Delta\delta)=(0.0, +0.5)$ in order of decreasing opacity.

a) The Self-Reversals

Comparison of the CO lines of differing opacities shows that the temperature dips near 10 km s^{-1} are indeed absorptions. With lines of higher opacity, the self-reversals become more pronounced, as would be expected with cooler foreground gas absorbing emission from hotter material. Phillips *et al.* (1981*a*) and Loren *et al.* (1981) found a still deeper self-reversal in the ^{12}CO($J=2$–1) line, as would be expected for the case of absorption.

It is interesting to note that the velocity centroids for most of the ^{13}CO($J=1$–0) lines (all of which are singly peaked) are slightly redshifted with respect to the ^{12}CO self-reversals; however, this is not true at the (1,0)

TABLE 1

TELESCOPE PARAMETERS FOR CARBON MONOXIDE OBSERVATIONS

Transition	T_{sys} (K)[a]	Filter (km s^{-1})	Beamwidth (arcsec)[b]	Cal[c]	Main Beam and Spillover Efficiency[d]
$^{12}CO(J=1-0)$ ...	2300	0.13	55	CHOP; H/C	0.65
$^{13}CO(J=2-1)$ ...	450	0.34	29	H/C	0.65
$^{13}CO(J=1-0)$ ...	480	0.54	59	NT; H/C	0.58

[a] Single sideband receiver temperature determined from response to ambient temperature absorbers and liquid-nitrogen-cooled loads (hot/cold loads).

[b] FWHM beamwidth determined from scans of Jupiter.

[c] Calibration: H/C = hot/cold loads; NT = noise tube; CHOP = chopper wheel. Sky opacity was monitored with sky dips for all the observations.

[d] Determined from scans of Jupiter and the Sun and from sky dips. The efficiencies are for sources greater in extent than the beamwidth.

position. Note that the self-reversals are not limited to just the central positions; they extend at least 2′ to the east and 1′ north, with some indications of absorption in the spectra to the west.

The $^{13}CO(J=2-1)$ spectrum also shows signs of line inversion, indicating that this transition may have a high opacity. The $^{13}CO(J=2-1)$ spectrum of Loren *et al.* (1981) is not self-reversed. The observations of Loren *et al.*, however, were made with a beam of 72″, while the data presented in this paper were made with a 29″ beam. If the region of $^{13}CO(J=2-1)$ self-reversal is limited in spatial extent, the observations are sensitive to beam dilution and pointing inaccuracies. In any case, the similar intensities of the $^{12}CO(J=1-0)$, $^{13}CO(J=2-1)$, and $^{13}CO(J=1-0)$ lines are indicative of optically thick material for these transitions.

b) *Broad Wings*

The ^{12}CO line wings cover more than 30 km s^{-1} at the central positions. In the northeast, the wings extend to the low-velocity side; in the southwest, the wings extend to the high-velocity side. The existence of broad wings and self-reversed lines in NGC 2071 may be related but do not seem correlated in a simple way; for example, the positions with the broadest wings do not have the deepest self-reversals, and one position (2,0) with a self-reversal lacks broad wings.

IV. DISCUSSION

The nature of self-reversed CO profiles has been debated for a number of years. Snell and Loren (1977) interpret self-reversals as indicative of nonhomologous gravitational collapse of the form

$$V_{\text{collapse}} \propto r^{-0.5}$$

for ^{13}CO lines peaking at a lower velocity than the velocity of the ^{12}CO self-reversal. Collapse models of this kind predict that the ^{12}CO peak at the lower velocity is several degrees stronger than the higher velocity peak. Loren *et al.* (1981) suggest that, for sources in which ^{13}CO line peak is redshifted with respect to the self-reversal dip, expansion may be indicated.

Leung and Brown (1977), on the other hand, emphasize the role of microturbulence and its interaction with systematic contraction or expansion. Another interpretation of self-reversals is that absorption occurs in a separate clump of colder foreground material (White and Phillips 1981; Phillips *et al.* 1981*a*).

The physical origin of broad CO wings in molecular clouds is also a subject of controversy. Rotation, collapse, expansion, and turbulence have all been suggested as possible causes of high-velocity gas motions.

We consider first the relationship between the self-reversals and broad wings. In Mon R2, the self-reversals and broad wings may have a common origin (Loren 1977). In the extended NGC 2071 molecular cloud, the situation is not clear. The CO self-reversals and broad wings are limited to the same central region of about 5 arcmin^2. However, since the map in Figure 1 shows that, within this central region, the self-reversals and broad wings are not spatially correlated in a simple way, we shall model the line wings and line core separately in subsequent analysis.

a) *Line Wings*

Figures 3*a* and 3*b* show the spatial distribution of the red and blue ^{12}CO and ^{13}CO wings in the form of velocity contour plots of V_{wing}, where V_{wing} is defined as the velocity to the 1 K intensity level for ^{12}CO, and as the velocity to the 0.8 K intensity level for ^{13}CO. The ^{12}CO blue wings are more pronounced to the northeast, and the red wings dominate in the southwest. Figure 3*c* displays this phenomenon in a different manner; temperature contours are plotted for ^{12}CO spectra at $V=17$ km s^{-1} and $V=3$ km s^{-1}. In direct contrast to the ^{12}CO

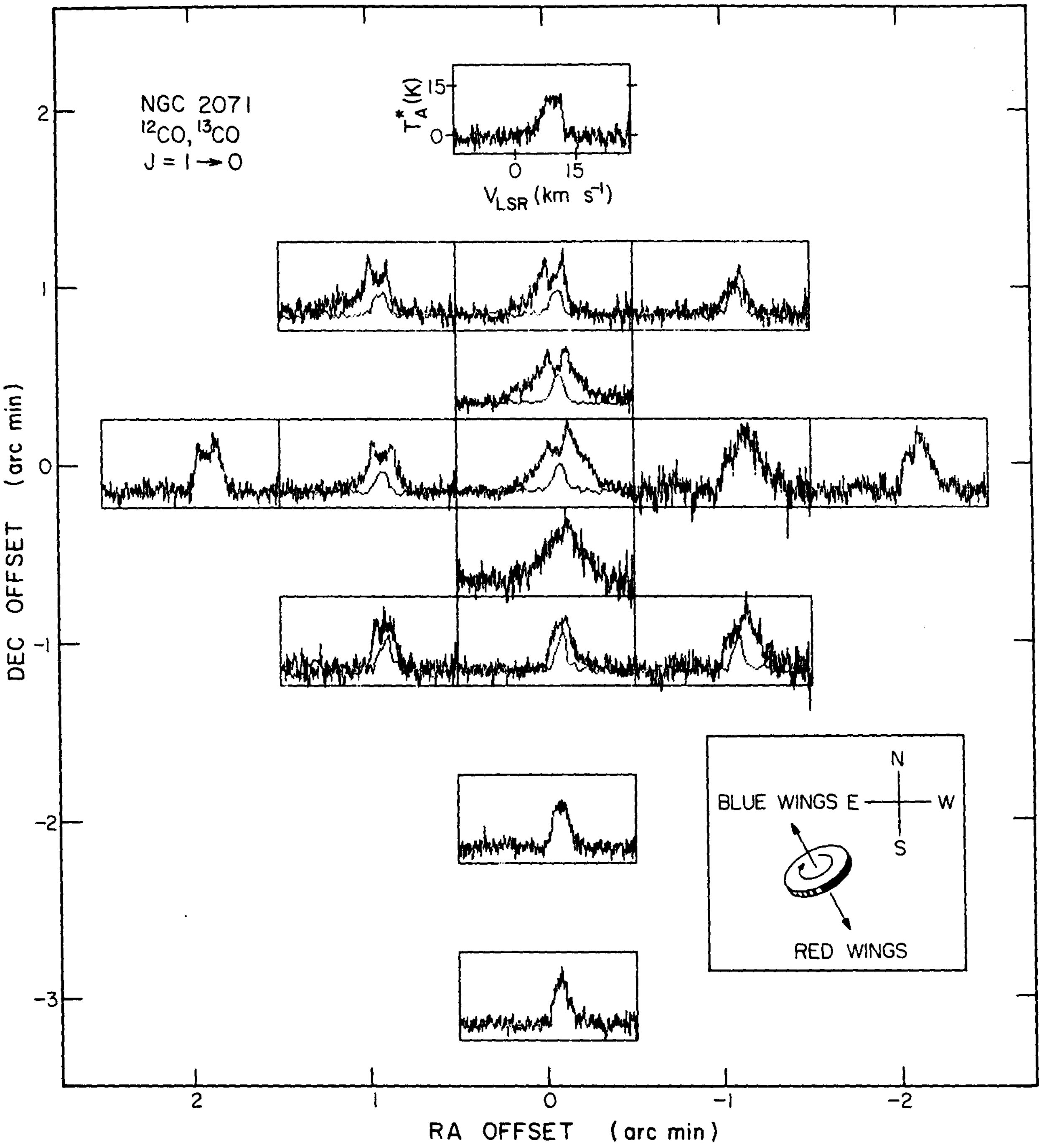

FIG. 1.—CO spectra observed in NGC 2071, with ^{13}CO lines plotted under the ^{12}CO lines. Insert at lower right shows orientation of disk and bipolar gas outflow.

spectra, the ^{13}CO red wings have a spatial distribution similar to that of the ^{13}CO blue wings. Figure 3*d* is a spatial velocity contour plot of V_{ave} for the ^{13}CO lines, defined as the average velocity of integrated emission (an average velocity for the ^{12}CO lines was not determined in this way because of the presence of self-absorption). The values of V_{ave} and of the blue and red components of V_{wing} for the ^{13}CO lines all increase slightly from the northwest to the southeast.

Spherically symmetric collapse or expansion as the cause of the broadened CO lines is ruled out by the anisotropic spatial distribution of the ^{12}CO wings. White and Phillips (1981) model NGC 2071 as a rotating disk with the sense of rotation defined by a NW–SE axis. This model cannot be reconciled with the ^{13}CO velocity patterns in Figure 3 which shows a progression of blue to red velocities from northwest to southeast. Dynamically, the rotating disk model seems unlikely to be a satisfactory explanation for the ^{12}CO wings since a central mass greater than $V^2r/2G \sim 10^4$ solar masses should then be present. Far-infrared measurements of Sargent *et al.* (1981) are compatible with the presence of a B3 star, which would have a mass several orders of magnitude less.

We propose the following explanation for the CO observations in NGC 2071. We interpret the ^{13}CO data as evidence for slow rotation of a disklike object. As shown in Figure 1, the axis of rotation is in the NE–SW direction (this is at right angles to the axis of rotation in the White and Phillips 1981 model). The disk shape of the molecular cloud can be seen in the NH_3 map of Calamai, Felli, and Giardinelli (1982), which shows the NGC 2071 molecular cloud to be elongated in the NW–SE direction with angular dimensions of 17′×5′. Assuming a distance of 450 pc to NGC 2071, we infer a velocity gradient of about 4 km s^{-1} pc^{-1} from Figure 3, corresponding to a turnover time of 7.5×10^5 years (if projection effects are important, the turnover time is somewhat smaller). The crossing time for line widths of about 10 km s^{-1} (30 km s^{-1} in the line wings) is much shorter, about 3×10^4 years (1×10^4 years for the material responsible for the high-velocity wings) over the inner 0.3 pc (2′) region. The ^{12}CO high-velocity features arise in gas streaming out the NE–SW poles of the disk. A strong stellar wind from a young stellar object could be the source of this motion. Bally (1981) arrives at a similar conclusion based on CO, infrared, and radio continuum observations, with an interpretation of mass outflow of at least $10^{-5}\ M_\odot$ yr^{-1}. It would not be surprising for the central star to be young; the OH and H_2O maser observations, and the infrared observations of Strom, Strom, and Vrba (1976) and of Strom *et al.* (1975) are all indicative of active star formation in this region.

This model is similar to models proposed by Snell, Loren, and Plambeck (1980) for L1551 and by Lada and Harvey (1981) for GL 490, and is also consistent with the cloud structure favored by Elmegreen and Morris (1979) for H_2O maser sources. The H_2O maser position in NGC 2071 coincides with the position of the broadest CO wings. The material ejected by the stellar wind is channeled along the poles because of the barrier presented by the dense, rotating disk. Blue wings in the northeast and red wings in the southwest are seen because the axis of the disk is tipped toward the observer. At the central position, the telescope beam covers material moving in both directions.

It is possible to obtain an order of magnitude estimate of the mass and energy in the high-velocity gas from the data in Figure 1. A comparison of the ^{12}CO and ^{13}CO spectra shows that most of the wing emission is optically thin in ^{12}CO; for example, at the (1, 1) position, the ratio of ^{12}CO to ^{13}CO intensities is greater than 50 for velocities less than 5.7 km s^{-1}. From the integrated ^{12}CO intensity in the line wings and using a projected area of 4 arcmin^2 (equal to 0.07 pc^2 at a distance of 450 pc), an excitation temperature of 20 K, and a CO abundance of 5×10^{-5} relative to hydrogen (Dickman 1978), we calculate a mass of approximately 1 $M_\odot$ in the high-velocity material. For different CO abundances or CO excitation temperatures, slightly different masses result from the calculation. The kinetic energy in the high-velocity material, $\frac{1}{2}MV^2$, is about 2×10^{45} ergs.

Several recent independent observations suggest that there is bipolar gas flow in NGC 2071, notably the detection by Persson *et al.* (1981) of a broad (total width$\sim$100 km s^{-1}) H_2 $V = 1\text{–}0$ $S(1)$ 2 μm line in NGC 2071. This line probably originates in high-velocity material near a shock which forms when the stellar wind pushes into the molecular cloud. In addition, the two small radio continuum sources detected by Bally (1981) are consistent with ionization of gas by a stellar wind.

Lada and Harvey (1981) have suggested that broad-winged CO sources with bipolar flow patterns may represent a new class of young objects characterized by CO velocity dispersions of 30 km s^{-1} or more, dynamical time scales of 10^3–3×10^4 years, kinetic energies of 10^{45}–10^{48} ergs, and anisotropic, bipolar outflow of material around an embedded infrared source. Although a disk geometry has been suggested as the mechanism constraining the gas flow to a bipolar pattern, observational evidence for disks in these sources, up to now, has been lacking; the ^{13}CO observations of NGC 2071 are the first that exhibit the velocity pattern expected from such a rotating disk. Although the shape of the molecular cloud cannot be deduced from the limited ^{13}CO coverage in Figure 1, its disk orientation is clearly visible in the NH_3 map of Calamai, Felli, and Giardinelli (1982).

b) *Line Cores*

Loren *et al.* (1981) categorize NGC 2071 as a self-reversal source with characteristics of overall cloud ex-

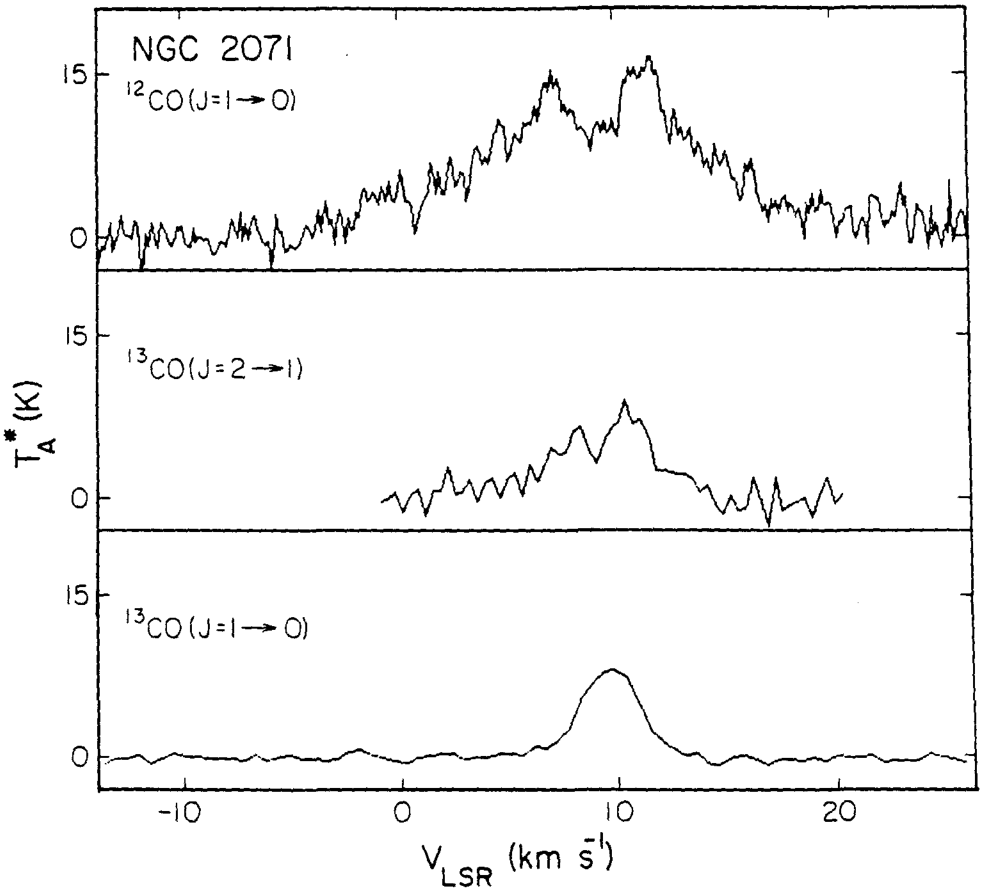

FIG. 2.—CO spectra at the position (0.0, +0.5) in order of decreasing opacity

pansion by comparing the velocities of the ^{13}CO peaks and the ^{12}CO absorption dip minima. The data in Figure 1, however, are not consistent with either simple collapse or expansion models: at the (1, 1) position, the ^{13}CO line peaks at a higher velocity than the velocity of the ^{12}CO dip (indicative of expansion), but the low-velocity ^{12}CO peak is stronger than the high-velocity ^{12}CO peak (indicative of collapse). These observations, as well as the fact that the self-reversals are not limited to a small region in the molecular cloud, can be explained if the self-reversals are due, in part, to cooler gas near the cloud periphery which is unaffected by the forces causing gas motions in the central regions.

A Monte Carlo nonlocal thermodynamic equilibrium, multi-level radiative transfer computer code (Bernes 1979) was used to produce model ^{12}CO and ^{13}CO line profiles. A CO abundance of 5×10^{-5} relative to hydrogen and a ^{12}CO/^{13}CO ratio of 60 were used. Figure 4 shows the parameters of the model cloud. A slow collapse velocity proportional to $r^{-0.5}$ was specified for the cloud, but the collapse was stopped at an inner radius equal to 1/30 the cloud outer radius. Also included in this model was a region of cool (12 K) gas at the cloud periphery moving away from the cloud core toward the observer with a velocity relative to the core of about 1.5 km s^{-1}. This material could represent gas unaffected by the gravitational force causing the collapse, or perhaps it could have acquired motion from an interaction with another cloud. The presence of this cool, outerlying gas was indicated by the shapes and spatial extent of the self-reversal dips.

As was shown earlier, the turnover time from rotation in NGC 2071 is much larger than crossover times inferred from the observed CO linewidths, even for the ^{12}CO lines without broad wings. Therefore, rotation is not the primary cause of the velocity dispersion in the line cores and other gas motions must be considered. In the Monte Carlo code calculations, radial mass motion was found to produce line core profiles which matched the observations much better than did the microturbulence-dominated models.

The results of the computer transfer calculations are shown in Figure 5. The aim of these calculations was to reproduce the main features of the line cores. Since the broad-wing features arise in gas streams which are physically distinct from the gas in the main portion of

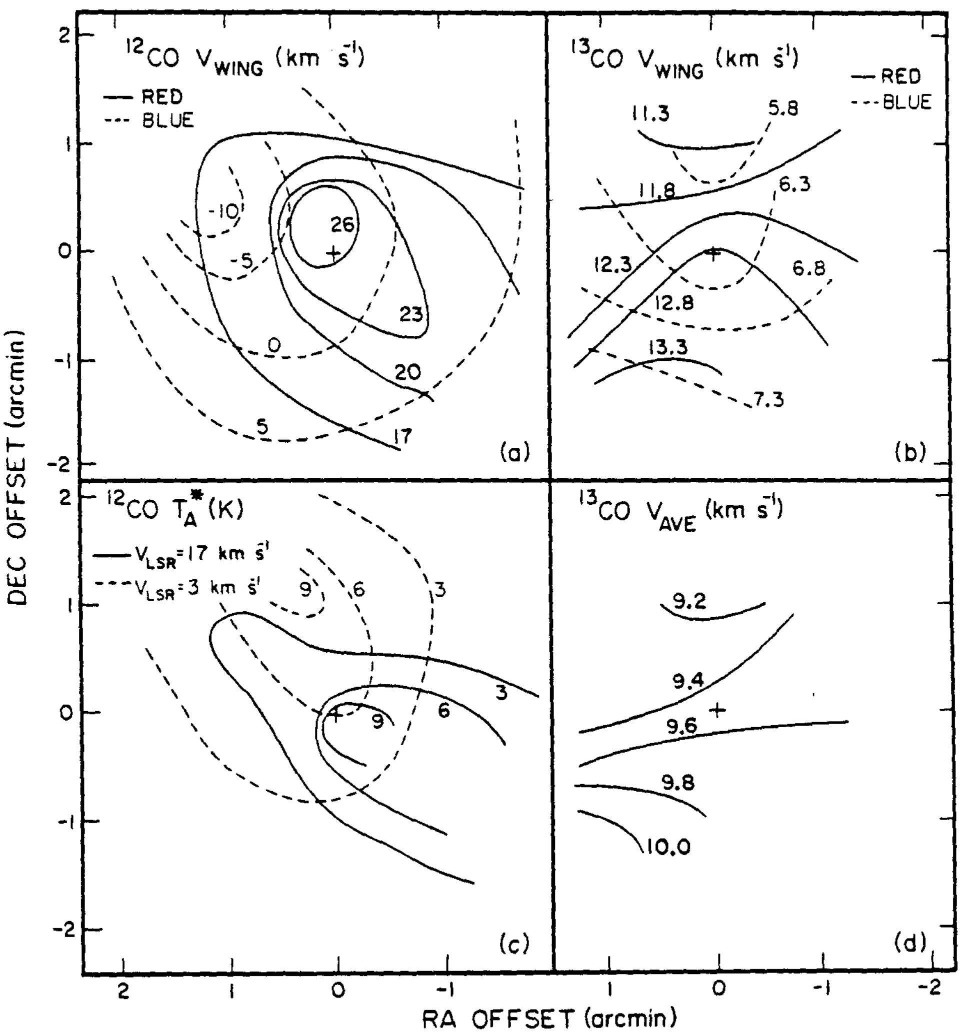

FIG. 3*a*.—$V_{\rm wing}$ ^{12}CO contours. 3*b*.—$V_{\rm wing}$ ^{13}CO contours. 3*c*.—T_A^* ^{12}CO contours at selected single velocity channels (width=0.13 km s^{-1} centered on the given velocity). 3*d*.—$V_{\rm ave}$ ^{13}CO contours.

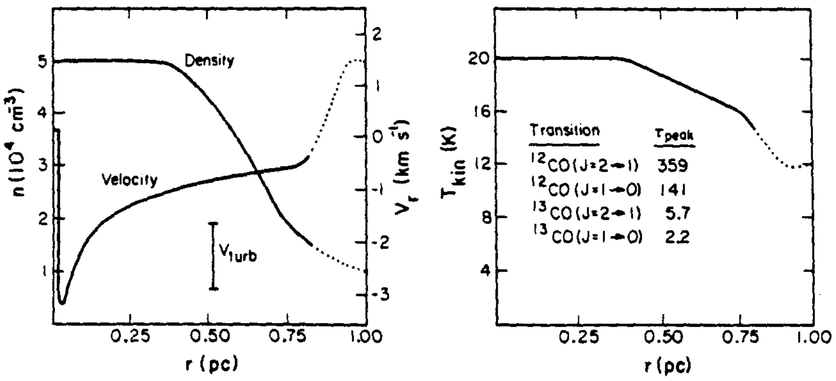

FIG. 4.—Distribution of radial velocity (relative to cloud center), density, and kinetic temperature in Monte Carlo model for the main body of the NGC 2071 molecular cloud. Dotted lines denote transition to region of cool, absorbing, foreground material at cloud periphery. Also shown are peak optical depths towards cloud center.

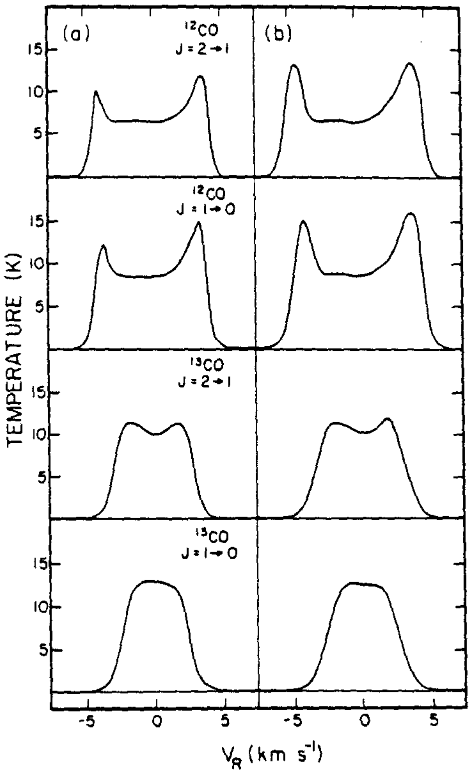

FIG. 5.—Line core profiles resulting from the model in Fig. 4 corresponding to (*a*) a line of sight displaced from cloud center by 0.07 pc (0.5′), and (*b*) a line of sight through cloud center. The model profiles are similar to the observed spectra at positions (0,0) and (0, +0.5) in Figs. 1 and 2.

the cloud, they were not included in these transfer calculations. The observed line core widths and intensities were reproduced in the model to within a factor of about 25%, even though the Monte Carlo code profiles were calculated for a spherically symmetric cloud. We cannot be certain that the cloud is collapsing; an expanding cloud model produces similar results. In the absence of a known energy source in the center of NGC 2071 strong enough to power overall cloud expansion, we chose to present the model for a contracting cloud, motivated in part by the arguments of Goldreich and Kwan (1974). It is significant that, even if most of the cloud is in a state of collapse, at some positions the relative intensities of the high-velocity and low-velocity ^{12}CO peaks, and the relative velocities of the ^{12}CO absorption dips and ^{13}CO peaks, have the appearance expected of an expanding cloud. This occurs because the absorbing material near the outer portion of the cloud between the observer and the cloud core is not participating in the collapse. Absorption in this foreground material shifts the self-reversal dip in the line profile to a lower velocity and decreases the intensity of the lower velocity ^{12}CO peak.

The observations in Figure 1 cannot be satisfactorily modeled with a single source in which there is only one sense of radial mass motion. Our model demonstrates how a simple form of cloud fragmentation could affect observed spectral profiles. Because of the limited data on which it is based, this model is not unique. However, from ^{12}CO(J=2–1) maps of NGC 2071, Phillips *et al.* (1981*a*) have also concluded that absorption (line inversion) occurs in a separate clump of cold, diffuse, foreground gas which is part of the local molecular complex.

The observed intensity and possibly self-reversed shape of the ^{13}CO (J=2–1) line indicate that there are high CO column densities in the direction of NGC 2071. The Monte Carlo model fitted to the observations incorporates hydrogen densities of 10^4–10^5 cm^{-3} over the 1 pc region of NGC 2071 covered in the CO maps. Even the ^{13}CO (J=1–0) line is optically thick, as would be expected from the similar observed line strengths for the ^{12}CO and ^{13}CO lines. Sandqvist *et al.* (1982) have detected HCO$^+$ emission over a central region more than 0.65 pc (5′) in diameter in NGC 2071. The HCO$^+$ results imply densities greater than 10^4 cm^{-3} throughout this part of the source since high densities are required to excite HCO$^+$ (Loren and Wootten 1981).

Additional observations are needed to determine more precisely the physical conditions in the disklike portion of the NGC 2071 cloud. The question of collapse or expansion still remains to be answered and might be resolved by high-resolution maps of high-excitation molecules. More observations of infrared hydrogen molecular lines are also needed to study the hot, high-velocity gas expected to be near the shock front caused by the stellar wind (Shull and Hollenbach 1978). As instrumental sensitivity and resolution improve, more broad-winged CO sources will probably be found; a better statistical sampling is necessary before the role of these objects in stellar formation and evolution can be determined.

V. CONCLUSIONS AND SUMMARY

Spectra of ^{12}CO and ^{13}CO lines mapped in NGC 2071 exhibit broad ^{12}CO wings and self-reversed line profiles at the central positions. There is strong evidence that the ^{12}CO high-velocity features originate in a bipolar gas flow powered by a stellar wind along the axis of a slowly rotating disklike structure. Model calculations indicate that there is systematic radial mass motion in the main body of the cloud and that the hydrogen density is 10^4–10^5 cm^{-3}; the self-reversals arise in part from transfer effects in collapsing (or expanding) material. However, absorption in cooler gas near the cloud periphery not participating in the motion of the main body of the cloud can significantly alter the appearance of the self-reversed spectra and make it difficult to distinguish between expansion and collapse motions in the rest of the molecular cloud.

The author wishes to express thanks to Dr. S. L. Scott for assistance with the 10.4 m system software and to the rest of the staff of the Owens Valley Radio Observatory for their support. The author is also grateful to Drs. H. A. Wootten, A. Sargent, T. Geballe, and J. Bally for useful discussions and for permission to cite unpublished data. Valuable suggestions were provided by Dr. P. G. Wannier. An anonymous referee is thanked for suggesting helpful changes in this paper. Research in Radio Astronomy at the Owens Valley Radio Observatory, California Institute of Technology, is supported by the National Science Foundation via grant AFT 80-16863.

REFERENCES

Bally, J. 1981, *Bull. AAS*, **13**, 540.
Bernes, C. 1979, *Astr. Ap.* **73**, 67.
Calamai, G., Felli, M., and Giardinelli, S. 1982, *Astr. Ap.*, submitted.
Dickman, R. L. 1978, *Ap. J. Suppl.*, **37**, 407.
Elmegreen, B. G., and Morris, M. 1979, *Ap. J.*, **229**, 593.
Goldreich, P., and Kwan, J. 1974, *Ap. J.*, **189**, 441.
Lada, C. F., and Harvey, P. M. 1981, *Ap. J.*, **245**, 58.
Leung, C. M., and Brown, R. L. 1977, *Ap. J. (Letters)*, **214**, L73.
Loren, R. B. 1977, *Ap. J.*, **215**, 129.
Loren, R. B., Plambeck, R. L., Davis, J. H., and Snell, R. L. 1981, *Ap. J.*, **245**, 495.
Loren, R. B., and Wootten, H. A. 1981, *Ap. J.*, **242**, 568.
Masson, C. R. 1980, *Proc. Soc. Photo-Opt. Instrum. Eng.*, **231**, 291.
Pankonin, V., Winnberg, A., and Booth, R. S. 1977, *Astr. Ap.*, **58**, L25.
Persson, S. E., Geballe, T. R., Simon, T., Lonsdale, C. J., and Baas, F. 1981, *Bull. AAS*, **13**, 513.
Phillips, T. G., Knapp, G. R., Huggins, P. J., Werner, M. W., Wannier, P. G., Neugebauer, G., and Ennis, D. 1981*a*, *Ap. J.*, **245**, 512.
Phillips, T. G., Woody, D. P., Dolan, G. J., Miller, R. E., and Linke, R. A. 1981*b*, *IEEE Trans.*, **MAG-17**, 684.
Sandqvist, A., Wootten, H. A., Loren, R. B., Friberg, P., and Hjalmarson, A. 1982, in *Proceedings of Symposium on Neutral Clouds Near* H II *Regions — Dynamics and Photochemistry, Regions of Recent Star Formation*, ed. R. S. Roger and P. E. Dewdney (Dordrecht: Reidel), in press.
Sargent, A. I., van Duinen, R. J., Fridlund, C. V. M., Nordh, H. L., and Aalders, J. W. G. 1981, *Ap. J.*, **249**, 607.
Shull, J. M., and Hollenbach, D. J. 1978, *Ap. J.*, **220**, 525.
Snell, R. L., and Loren, R. B. 1977, *Ap. J.*, **211**, 122.
Snell, R. L., Loren, R. B., and Plambeck, R. L. 1980, *Ap. J. (Letters)*, **239**, L17.
Strom, K. M., Strom, S. E., Carrasco, L., and Vrba, F. J. 1975, *Ap. J.*, **196**, 489.
Strom, K. M., Strom, S. E., and Vrba, F. J. 1976, *A.J.*, **81**, 308.
White, G. J., and Phillips, J. P. 1981, *M.N.R.A.S.*, **194**, 947.

STEPHEN M. LICHTEN: California Institute of Technology 102-24, Pasadena, CA 91125

CHAPTER 2

HIGH-VELOCITY MOLECULAR GAS IN THE DARK CLOUD L1529

Reprinted from *The Astrophysical Journal (Letters)*, *255*, L119 (1982)

THE ASTROPHYSICAL JOURNAL, 255:L119–L122, 1982 April 15

HIGH-VELOCITY MOLECULAR GAS IN THE DARK CLOUD L1529

STEPHEN M. LICHTEN
Owens Valley Radio Observatory, California Institute of Technology
Received 1981 November 30; accepted 1982 January 8

ABSTRACT

High-velocity CO wings have been detected near a dense condensation in the dark cloud L1529. Embedded stars or young stellar objects nearby have been identified as likely energy sources responsible for the unusual velocity dispersion (30 km s^{-1}) in the wings; these objects may also be responsible for the more moderate, yet still supersonic velocity dispersion (2–3 km s^{-1}) typical of the CO line cores. The observations of CO and high-excitation molecules in L1529 are consistent with cloud models in which stellar winds play a major role in the energetics and internal kinematics of dark clouds.

Subject heading: interstellar: molecules

I. INTRODUCTION

Extended wings in the lines of CO and other molecules at millimeter wavelengths have been observed in a number of molecular clouds. Initially such profiles were found in regions close to H II regions, infrared heating sources, or hot luminous gas. Included in this category are Orion A (Kwan and Scoville 1976), L1551 (Snell, Loren, and Plambeck 1980), Cep A (Rodriguez, Ho, and Moran 1980), AFGL 490 (Lada and Harvey 1981), NGC 2071 (Lichten 1982), W3 (Snell and Loren 1977; Sandqvist *et al.* 1982), Mon R2 (Loren 1977), HH 7-11, and T Tauri (Snell and Edwards 1981).

Broadened line wings have also been observed in the direction of dark molecular clouds where no compact infrared sources have as yet been detected. Examples are L723, L1455, and L1427 (Frerking and Langer 1982). Characteristic line wing dispersions for these dark cloud profiles are 3–10 km s^{-1}, as opposed to the considerably higher 30–80 km s^{-1} dispersions typical of the more energetic regions in the first category.

We report the detection of atypically broad, low-intensity CO line wings from a quiescent region of the dark cloud L1529. There is no evidence for the presence of embedded protostellar objects in this direction (Walmsley, Winnewisser, and Toelle 1979; Avery 1980). We present a possible explanation for our observations in terms of the interaction between young stellar objects and internal gas kinematics of dark molecular clouds.

II. OBSERVATIONS AND RESULTS

L1529 was observed in the $J = 1\text{–}0$ rotational transitions of ^{12}CO and ^{13}CO at 115271 and 110201 MHz in 1980 December and 1981 January. A region 7′ × 4′ in size, centered at $\alpha(1950) = 4^h29^m43^s.4$; $\delta(1950) = 24°16'54''$, was mapped in ^{12}CO at approximately beamwidth spacings; at five central positions, ^{13}CO spectra were also taken. Antenna No. 2 of the Caltech 10.4 m array at the Owens Valley Radio Observatory in Big Pine, California, was used in conjunction with a liquid helium cooled, superconducting-insulating-superconducting (SIS) tunnel junction receiver (Phillips *et al.* 1981) and a 512 channel acousto-optic spectrometer (Masson 1980). Spectral resolution was 200 kHz. The antenna main beam (full width at half-maximum) was measured to be 55″ at 115271 MHz from Jupiter scans. Observational techniques and methods of calibration are fully described by Lichten (1982).

Contours of peak T_A^*, the antenna temperature corrected for instrumental and atmospheric losses, are shown in Figure 1*a*. The spatial variations of ^{12}CO line width ΔV, defined as $[\int T_A^*(v)dv]/T_A^*(\text{peak})$, are presented in Figure 1*b*. Spectra from the positions $(\Delta\alpha, \Delta\delta) = (0,0)$ and $(-1,-2)$, where broad ^{12}CO wings were detected, are shown in Figure 2.

III. DISCUSSION

L1529, also designated TMC-2, is located in the Taurus dark cloud complex at a distance of 135 pc (Elias 1978). From observations of HC_5N, NH_3, HCO^+, HC_3N, and CS (Myers, Ho, and Benson 1979; Walmsley, Winnewisser, and Toelle 1979; Wootten, Snell, and Evans 1980; Linke and Goldsmith 1980), it has been concluded that L1529 has a round, dense core of density $\sim 5 \times 10^4$ cm^{-3}, roughly 0.1 pc (2′.5) in size, with a mass ~ 1 $M_\odot$, located at the position $\alpha(1950) = 4^h29^m43^s$; $\delta(1950) = 24°19'00''$. This position corresponds to the position (0,2) in Figures 1*a* and 1*b*. Our preliminary observations of L1529 indicated that CO emission extends for several degrees over the entire complex of more tenuous material in which this high-density condensation is embedded.

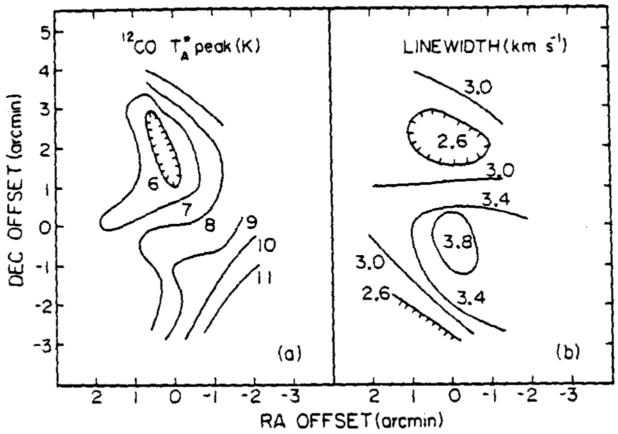

FIG. 1.—(*a*) Contours of peak $T_A{}^*(^{12}CO)$, and (*b*) contours of ^{12}CO line width in L1529.

L1529 has been characterized as a stable, quiescent region, with its dense core possibly in hydrostatic equilibrium (Myers, Ho, and Benson 1979). Optically thin molecules excited in the dense core have line widths as narrow as 0.15 km s^{-1}, only about twice the thermal velocity for a gas temperature near 10 K (as determined from the ^{12}CO temperature). Our detection of high-velocity CO wings demonstrates that there is energetic material in L1529.

Our CO observations of L1529 have the following characteristics:

1. High-velocity ^{12}CO line wings are present at the (0, 0) and (−1, −2) positions, with indications of possible wings at (0, −1) and (−1, −1). The (0, 0) wings have a full width of 30 km s^{-1} at the rms noise level of 0.09 K. No ^{13}CO wings were detected. The effects of the broad-line wings are visible in Figure 1*b* as enhancements in ΔV at (0, 0) and at positions to the southwest.
2. The average velocity (excluding the broad-line wings), $\langle V_{LSR} \rangle$, of both the ^{12}CO and ^{13}CO lines is constant to within 1 channel (0.5 km s^{-1}) of 6.0 km s^{-1} across the mapped portion of the cloud.
3. Figures 1*a* and 1*b* show that at the position of the high-density condensation, (0, 2), the ^{12}CO temperature and line width decrease to their minimum values. In nearly all other broad-winged sources, the positions of highest velocity dispersion coincide with density peaks. This is not the case in L1529.

Since we cannot deduce the optical depth in the CO line wings from our data alone, we cannot explicitly calculate the mass of the high-velocity material. We can, however, establish reasonable limits to its value. Assuming that the wings are optically thin, that the excitation temperature is 12 K, and that the relative CO/H_2 abundance is 5×10^{-5}, we calculate, following Lada and Harvey (1981), a high-velocity mass of 0.02 $M_\odot$. The projected area used in this calculation was 8 $arcmin^2$, but this quantity is somewhat uncertain. A higher value for the mass would result from optically thick CO in the line wings or from higher excitation temperatures. We have overestimated the mass only if clumping is significant for the high-velocity material. An upper limit of 0.5 $M_\odot$ follows from the 0.09 K rms noise level in the ^{13}CO spectrum, assuming that $N(^{12}CO)/N(^{13}CO) = 60$. It appears that the high-velocity mass is considerably less than the 1 $M_\odot$ in the dense condensation 3′ to the northeast.

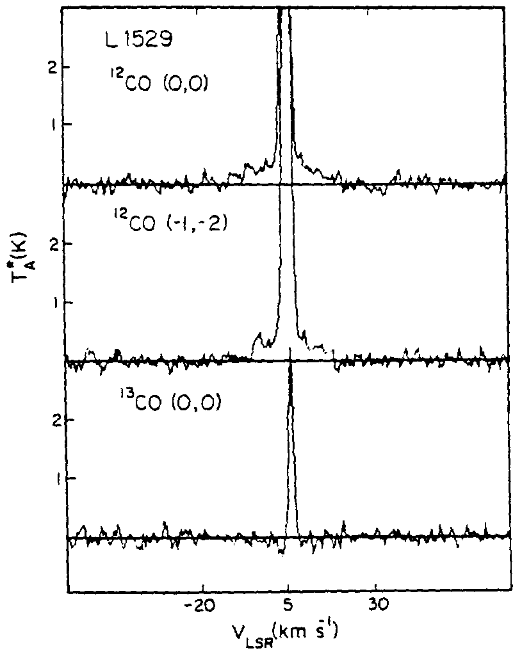

FIG. 2.—CO spectra at the positions where broad wings were detected. Offsets ($\Delta\alpha$, $\Delta\delta$) are in arcmin relative to $\alpha(1950) = 4^h29^m43^s.4$, $\delta(1950) = 24°16'54''$.

The broad wings could result from systematic mass motions such as rotation, collapse, or expansion. Rotation and asymmetric cloud collapse can be ruled out since, in either of these two cases, a large central mass, $M \geq V^2R/2G \sim 100\ M_\odot$, would be required to account for the observations in Figure 2. Furthermore, neither the aforementioned observations of high-excitation molecules from the dense condensation, nor our CO observations (which presumably arise in the surrounding, more tenuous material) show any evidence for systematic changes in the velocity centroid across L1529.

Collimated bipolar mass outflow, which does not require a large central mass, has been suggested as an explanation for the presence of broad molecular line wings in AFGL 490 (Lada and Harvey 1981), L1551 (Snell, Loren, and Plambeck 1980), and NGC 2071 (Lichten 1982). Our data, although limited, do not show the pronounced anisotropic spatial distribution of red and blue wings characteristic of this phenomenon. It is unlikely that there is a bipolar mass outflow whose axis is aligned directly toward the observer so that both red

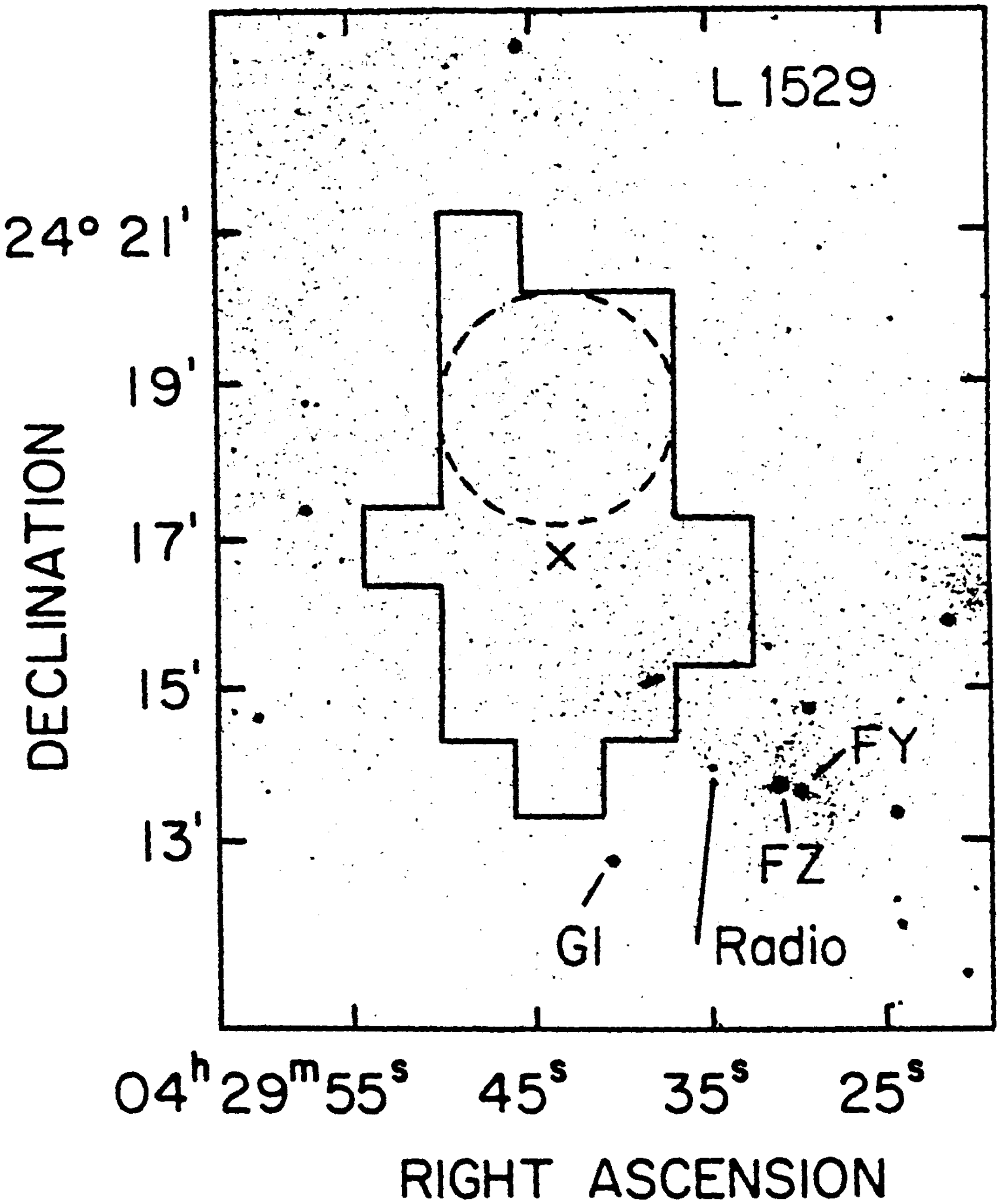

FIG. 3.—Enlarged portion of POSS print showing area mapped in CO (*solid line*); the dense, cooler, molecular condensation (*dashed line*); radio continuum source position; and stellar objects FY Tau, FZ Tau, and HK Tau/G1. (0,0) position is marked with an ×. © 1960. National Geographic Society—Palomar Sky Survey. Reproduced by permission of the California Institute of Technology.

and blue wings would be observed simultaneously. Further observations are needed to better determine the spatial extent of high-velocity wings in L1529.

Two nearby stars, FY Tau and FZ Tau, have been classified as T Tauri-like objects on the basis of their infrared magnitudes (Elias 1978). Also known as Haro 6-17 and Haro 6-18, their spectra exhibit strong emission lines typical of Herbig-Haro objects (Cohen and Kuhi 1979). Directly south of the CO broad-wing detections is a 16.8 mag star, HK Tau/G1, which Cohen and Kuhi suggest is a B2 star, possibly embedded, but without a dust shell. In addition, between these stars and the region of broad CO wings, Gilmore (1980) has detected three compact radio continuum sources, one of which has a flat spectrum and has been tentatively identified as an H II region. Figure 3, an enlarged portion of an E print from the Palomar Observatory Sky Survey (POSS), shows the area covered by the CO observations as well as the positions of the dense molecular condensation, the radio continuum source, and the nearby stars (or young stellar objects). A stellar feature coincides with the position of the radio source; it is especially intriguing that a nebulous object is visible at the $(-1, -2)$ position of broad CO line wings.

The stellar luminosity required to power gas motions by photon pressure is roughly $L/c \sim MV(V/R)$. We calculate $\sim 400\ L_{\odot}$ to drive $0.02\ M_{\odot}$ at a velocity of 10 km s^{-1} over 4′ (0.16 pc). Van Duinen *et al.* (1982) have found an upper limit of $\sim 2\ L_{\odot}$ for embedded stellar far-infrared sources in L1529. Therefore, mechanical forces, rather than photon pressure, are probably responsible for the observed broad wings.

It is possible that some energetic phenomenon (such as high-velocity winds) associated with these nearby young stellar objects is disturbing the molecular gas surrounding the dense quiescent core in L1529. The observed 30 km s^{-1} spread in CO broad wings is several orders of magnitude greater than the sound speed in 12 K gas, so shocks must be present. The extreme high-velocity CO wings probably originate near the shocks. Given the presence of shock fronts, it is likely that the warm, more tenuous gas (where most of the CO emission originates) surrounding the cooler, dense condensation to the northeast is somewhat nonhomogeneous. The velocity dispersion of the CO line cores (2–3 km s^{-1}) may represent relative velocities of molecular clumps throughout the region. Since these clumps have a kinetic gas temperature of ~ 12 K (deduced from saturated ^{12}CO line intensities) and there is little evidence for appreciable large-scale mass motion in L1529, we suggest that their relative supersonic velocities are also due to the energetic input of the nearby young stellar objects.

The Norman and Silk (1980) model for T Tauri stars and clumpy molecular clouds fits our observations rather well. As predicted by Norman and Silk, in L1529 there appear to be: (1) a cold, dense condensation ~ 0.1 pc in size embedded in a warmer, less dense medium; (2) narrow spectral lines (width ~ 0.1–0.3 km s^{-1}) observed from the dense condensation, as opposed to the higher velocity dispersion (~ 3 km s^{-1}) for molecular line emission from the surrounding, nonhomogeneous, warmer gas; (3) extreme high-velocity line wings which can be produced in regions where T Tauri winds are initially shocked if postshock material is nonhomogeneous.

Further observations are needed to determine the degree and scale size of clumping in L1529. More detailed information on the spatial distribution of the CO wings would also be useful so that a more exact physical model for L1529 can be constructed. In conclusion, we find that our CO observations are certainly consistent with cloud models in which energetic input from embedded stellar objects plays a major role in internal kinematics of dark molecular clouds.

This research was supported by the National Science Foundation via grant AFT 80-16863. S. Scott, D. Woody, and C. Masson provided valuable assistance at Owens Valley Radio Observatory. A. I. Sargent is thanked for communication of unpublished data.

REFERENCES

Avery, L. W. 1980, in *Interstellar Molecules*, ed. B. H. Andrew (Dordrecht: Reidel), p. 47.
Cohen, M., and Kuhi, L. V. 1979, *Ap. J. Suppl.*, **41**, 743.
Elias, J. H. 1978, *Ap. J*, **224**, 857.
Frerking, M. A., and Langer, W. D. 1982, *Ap. J.*, submitted.
Gilmore, W. 1980, *A. J.*, **85**, 894.
Kwan, J., and Scoville, N. Z. 1976, *Ap. J.* (*Letters*), **210**, L39.
Lada, C. J., and Harvey, P. M. 1981, *Ap. J.*, **245**, 58.
Lichten, S. M. 1982, *Ap. J.*, **253**, 593.
Linke, R. A., and Goldsmith, P. F. 1980, *Ap. J.*, **235**, 437.
Loren, R. B. 1977, *Ap. J.*, **215**, 129.
Masson, C. R. 1980, *Proc. Soc. Photo-Opt. Instrum. Eng.*, **231**, 291.
Myers, P. C., Ho, P. T. P., and Benson, P. J. 1979, *Ap. J.* (*Letters*), **233**, L141.
Norman, C., and Silk, J. 1980, *Ap. J.*, **238**, 158.
Phillips, T. G., Woody, D. P., Dolan, G. J., Miller, R. E., and Linke, R. A. 1981, *IEEE Trans.*, **MAG-17**, 684.
Rodriguez, L. F., Ho, P. T. P., and Moran, J. M. 1980, *Ap. J.* (*Letters*), **240**, L149.
Sandqvist, A., Wootten, A., Loren, R. B., Friberg, P., and Hjalmarson, A. 1982, in *Regions of Recent Star Formation, Proc. Symposium on Neutral Clouds near H* II *Regions—Dynamics and Photochemistry*, ed. R. S. Roger and P. E. Dewdney (Dordrecht: Reidel), in press.
Snell, R. L., and Edwards, S. 1981, *Bull. AAS*, **13**, 540.
Snell, R. L., and Loren, R. B. 1977, *Ap. J.*, **211**, 122.
Snell, R. L., Loren, R. B., and Plambeck, R. L. 1980, *Ap. J.* (*Letters*), **239**, L17.
Van Duinen, R. J., Sargent, A. I., Aalders, J. W. G., Fridlund, C. V. M., and Nordh, H. L. 1982, in preparation.
Walmsley, C. M., Winnewisser, G., and Toelle, F. 1979, *Astr. Ap.*, **81**, 245.
Wootten, A., Snell, R., and Evans, N. J., II. 1980, *Ap. J.*, **240**, 532.

STEPHEN M. LICHTEN: California Institute of Technology, Mail Code 105–24, Pasadena, CA 91125

CHAPTER 3

WARM H I HALOS AROUND MOLECULAR CLOUDS

Reprinted from The Astrophysical Journal, 268, 727 (1983)

THE ASTROPHYSICAL JOURNAL, 268:727-738, 1983 May 15

WARM H I HALOS AROUND MOLECULAR CLOUDS

PETER G. WANNIER AND STEPHEN M. LICHTEN
Department of Astronomy, California Institute of Technology
AND
MARK MORRIS
Astronomy Department, Columbia University

Received 1982 August 9; accepted 1982 November 8

ABSTRACT

Observations of H I have been made with the 305 m Arecibo dish toward the isolated edges of several molecular clouds. Comparison with 1.3 and 2.6 mm CO line emission indicates the existence of H I halos extending 0.5 to several pc beyond the CO boundaries. Because the halos appear in emission against the ~ 100 K galactic H I background, the gas is evidently warmer than much of the interstellar H I gas. The observed column densities and transition zone thicknesses agree well with steady state calculations equating the formation rate of H_2 on grains to its destruction by UV radiation.

Subject headings: interstellar: molecules — radio sources: 21 cm radiation

I. INTRODUCTION

Dense molecular clouds are observed to have sharp (< 1 pc) boundaries, where the bulk of the gas presumably changes from atomic to molecular form. The sharp transition from atomic to molecular hydrogen has been inferred from a distinct break in N_{H_2} (from $< 10^{16}$ to $> 10^{19}$ cm^{-2})[1] near $E(B-V) = 0.08$ (Savage *et al.* 1977). In addition, radio observations of carbon monoxide indicate that the boundaries of CO line-emitting regions are fairly sharp (e.g., Blitz and Thaddeus 1980). The H I/H_2 and C^+/CO transition zones are important to the evolution of molecular clouds, yet observations provide little information about their extent, temperature, or space density.

The transition between C^+ and CO has been studied theoretically by several authors (e.g., Werner 1970; Glassgold and Langer 1975). It appears that if CO is formed by ion-molecule reactions, then the location of the boundary is determined by the abundances of intermediaries such as OH, which in turn depend upon the penetration of ambient galactic UV into the boundary layer. The CO boundary therefore occurs where the outward column density of dust becomes adequately large. According to Glassgold and Langer, this corresponds to a characteristic column density of $N_{\mathrm{H}} \sim 3 \times 10^{21}$ cm^{-2}.

For hydrogen gas, the thickness of the atomic-to-molecular transition zone is determined theoretically by balancing the photodestruction of H_2 against its formation on grains (Field, Sommerville, and Dressler 1966; Hollenbach, Werner, and Salpeter 1971). Recent calculations, improving on earlier approximations, have increased the expected transition zone thickness by a factor of ~ 3 (Federman, Glassgold, and Kwan 1979, hereafter FGK), implying an H I column density which should be readily observable at the perimeters of dense clouds ($N_{\mathrm{H\,I}} \sim 3 \times 10^{20}$ cm^{-2}). Because this column density is substantially smaller than that inside the CO/C^+ boundary, the H I at a cloud edge should lie well outside the region from which CO emission is observable.

Although several previous H I studies of molecular clouds have been made, most have focused their attention on the lines of sight to the dense cloud cores, where the effects of the boundary layers might be masked. In the present study we focus on the properties of the cloud boundaries by observing H I at the edges of known, isolated CO clouds (Table 1) with the spatial resolution necessary to resolve the boundary layer in profile.

II. OBSERVATIONS

Neutral hydrogen observations were obtained between 1978 November 8 and 12 with the 305 m reflector of the Arecibo Observatory.[2] The receiving system consisted of a dual-channel uncooled parametric amplifier and a 13 m dual circular feed optimized to an observing frequency of 1405 MHz. At zenith (and at 1420 MHz),

---

[1] Throughout this paper, the subscripts H, H I, and H_2 will be used in conjunction with density (n) or column density (N) and will refer, respectively, to number of hydrogen atoms in the form of H I + H_2, in the form of H I, and in the form of H_2.

TABLE 1

SOURCE LIST

Source	R.A. (1950)	Decl. (1950)	l (°)	b (°)	$v_{\rm lsr}$ (km s^{-1})
Per OB2-C	$3^{h}13^{m}45^{s}.0$	29°36′00″	156.7	−23.3	2.0
Per OB2-B	3 25 40.0	28 52 00	159.7	−22.4	7.5
Per OB2-A	3 37 00.0	29 49 36	161.2	−20.1	8.0
L1599-B	5 46 45.0	7 21 15	199.1	−10.2	10.0
L1599-A	5 48 01.8	7 37 12	199.0	−9.8	10.0
S255	6 10 01.0	18 00 00	192.6	−0.0	7.0
Mon filament ...	6 20 00.0	3 42 06	206.4	−4.7	10.0
Mon OB1	6 28 00.0	13 00 00	199.1	1.4	5.6

this combination produced a gain of 6.7 K Jy^{-1}, a main lobe HPBW of 3′.6, and effective system temperatures of 75 and 90 K in the two channels. The dual circular line feed produced an approximately uniform illumination pattern, therefore yielding high sidelobe levels. The antenna response was dominated by the main lobe and the first diffraction ring of radius 5′.6, having a response −11.3 dB (a factor of 13.5) below the main beam. The integrated response of the first diffraction ring was about one-half that of the main beam, so that some care is necessary when interpreting the intensities of small ($\leq 10'$) spectral line sources relative to the intensity of the more extended galactic H I emission. The antenna performance (system temperature, antenna gain, and sidelobe levels) begins to degrade at zenith angles exceeding ~10° because of vignetting (the feed begins to illuminate the ground). These zenith angle effects were measured, and appropriate corrections were applied to each spectrum. Very few of the spectra were obtained at zenith distances exceeding 14°. The temperature scale for all observations was set by comparing, for each observing frequency, a noise tube calibration signal with a standard calibration source (Her A and/or 3C 33), the fluxes for the latter taken from the list of Bridle *et al.* (1972). The back end was an autocorrelation spectrometer, typically used with a total bandwidth of 2.5 MHz (and 252 channels) or 5.0 MHz (and 504 channels), yielding a spectral resolution of 2.1 km s^{-1}. The spectra were frequency switched by half the spectrometer bandpass and centered such that the observed features from both halves of the switching cycle could be added together by folding the spectra.

Observations of the $J = 2-1$ and 1–0 transitions of CO were made at the Owens Valley Radio Observatory using one of the two antennas of the millimeter-wave interferometer. Calibration of the temperature scale was achieved by measuring the system response to ambient-temperature and liquid nitrogen-cooled microwave absorbers. The reported antenna temperatures (T_A^*) are corrected for antenna efficiency and for sky opacity as determined from observations of sky emission at different elevation angles.

At the CO(2–1) frequency of 230 GHz, a Cassegrain-mounted hot-electron bolometer was used, yielding a receiver noise temperature of ~350 K over a bandwidth of 1 MHz (1.3 km s^{-1}). The CO(2–1) data consist of single-frequency strip maps made by sweeping the antenna over the desired strip and sampling the receiver output. It was assumed (and observed) that all the observed clouds were much larger than the 26″ telescope beamwidth so that the extended-source beam efficiency of 0.65 was used to scale the observations.

Most of the CO(1–0) data (115 GHz) were obtained with a superconducting tunnel junction (SIS) receiver ($T_{\rm rec} = \sim 380$ K [single-sideband]) and a 512 channel acousto-optic spectrometer with an effective resolution of 200 kHz (0.52 km s^{-1}). For one source (L1599-A) the 1–0 data were obtained with a room-temperature Schottky diode receiver ($T_{\rm rec} = 2200$ K [single-sideband]) and a 512 channel autocorrelator with a resolution of 48.8 kHz (0.13 km s^{-1}). For both CO(1–0) receiver systems, the antenna beamwidth (FWHM) was 58″. Spectra were obtained at different map positions by position switching to off-positions observed to have no CO emission. An extended-source antenna efficiency of 0.75 was used to scale the CO(1–0) observations.

III. RESULTS AND DISCUSSION OF INDIVIDUAL SOURCES

Figures 1–5 display the CO data in the form of strip maps of T_A^*, the antenna temperature corrected for effects of atmospheric opacity and antenna efficiency. The strips were chosen to cross the CO cloud edges at positions where the boundary seemed to be well defined, with no apparent filaments or wisps extending beyond the outer boundary. The location of each strip relative to the larger molecular cloud is shown with a heavy solid line on maps taken from the literature. The H I data are

---

[2] Arecibo Observatory, Arecibo, Puerto Rico. The Arecibo Observatory is part of the National Astronomy and Ionosphere Center, operated by Cornell University under contract with the National Science Foundation.

expressed as T_A, which does not include the scaling correction for coupling of the source to the antenna beam pattern. This correction for beam efficiency actually varies across the H I strip map depending on the relative proportions of the source and the galactic background filling the Arecibo secondary diffraction ring sidelobe; for all the sources in our sample, the beam efficiency scaling factor is close to 1.5, and we shall explicitly include this factor in subsequent analysis (§ IV).

Where possible, the CO(1-0) strips are presented in the form of velocity-position contours, thus indicating both the spatial distribution and kinematic behavior of the molecular gas. Velocity information is not available for the CO(2-1) data which provide intensity information for a single[3] velocity channel (1.3 km s^{-1} wide). For the H I data, velocity-position contours do not provide very clear information about the clouds under study because of the presence of broad and intense emission from background galactic H I (see, for example, Fig. 5). In the clouds studied, the CO line widths (FWHM) are less than 2.5 km s^{-1} near the cloud edges. Therefore, in order to minimize confusion with the background emission, the H I strips show the H I intensity from a single spectrometer channel (2.1 km s^{-1} wide) chosen to be closest to the velocity of the peak of the CO line.

a) *S255*

The S255 molecular cloud has been studied extensively by Evans, Blair, and Beckwith (1977), who adopt (in a note added in manuscript) a distance of 2.5 ± 0.5 pc and a mass of ~ 10^4 $M_\odot$. Although the source lies in the galactic plane ($l, b = 192.^\circ6, -0.^\circ04$), it appears to be a reasonably compact and isolated region. The CO cloud is actually associated with a cluster of red nebulae, denoted S254 to S257 by Sharpless (1959). Of these, S255 and S257 are compact (~ 2′ diameter) H II regions, associated with intense continuum emission and lying ~ 2′ to the east and west of the molecular peak, respectively, and S254 is a more diffuse (~ 8′ diameter) H II region lying ~ 8′ to the west of the molecular peak.

The two maps in Figure 1 are N-S and E-W strips passing through the molecular peak and passing through the northern and western boundaries, respectively. The E-W strip passes through (and beyond) the visible H II regions S257 and S254, while the N-S strip does not pass directly through any compact H II region. Considerable Hα emission is visible on the Palomar Sky Survey throughout the S255 region, and it seems likely that the gas is ionized beyond both of the two observed cloud edges. Both strips have clean CO boundaries and sharp H I peaks, rising up clearly above the background H I emission. The H I emission peaks are apparently under-resolved by the telescope beam, but the atomic spin temperature (and hence, T_k) is apparently greater than 140 K ($T_A > 100$ K), at least at the western boundary.

b) *Perseus OB2*

The molecular cloud associated with the Per OB2 association has been studied by Sargent (1979) and Baran (1982). The cloud has a mass of ~ 10^4 $M_\odot$ and lies well out of the galactic plane ($b = -23°$ to $-16°$) at a distance of 350 ± 50 pc (Baran 1982). Because of its proximity (compared with S255, for example), the region has a large apparent extent, ~ 7°, and is elongated at an angle of ~ 45° to the galactic plane. There is apparent star-formation activity in the dense cloud as evidenced by the presence of several Herbig-Haro objects and the H II region (and IR source) NGC 1333, but the H II region is well separated from the boundaries studied, and there is no other evidence for an envelope of ionized gas (from the Palomar Sky Survey, for example).

The three cloud edges chosen for study are shown in Figure 2*d* and correspond to the strip maps (Per OB2-A, B, and C). Two of the edges (A and C) show clear H I peaks at the CO boundary and, owing to the proximity of the region, are both well resolved by the 3.′6 telescope beam. In both cases the H I peak is clearly associated with the CO cloud edge. The third strip (B), running south from NGC 1333, shows a distinct rise in H I brightness temperature starting at the CO boundary. However, the H I strip map is not long enough to be certain whether or not a peak of emission is formed. The lower resolution *Berkeley Low Latitude Survey of Neutral Hydrogen* (Weaver and Williams 1974*b*) shows that the increase at this boundary is a local phenomenon since the 21 cm intensity decreases by 40% about 2.°5 south of Per OB2-B (0, 0).

In Figure 2*c*, H I intensities at three velocities are shown because of the velocity gradient which occurs in the CO spectra toward the cloud edge. The H I velocities presented (1, 3, and 5 km s^{-1}) were chosen because of the increase in the CO velocity toward the cloud core (off the map in Fig. 2*c*). Most of the molecular material (as traced by CO) in Per OB2-C is at higher velocities than the ~ 0 km s^{-1} velocity at the cloud edge.

c) *L1599*

The L1599 molecular cloud is an isolated molecular cloud lying well out of the galactic plane ($b \sim -10°$). The molecular cloud has been studied at CO(1-0) by Maddalena *et al.* (1983), who estimate a cloud mass of 1300 ± 400 $M_\odot$. L1599 is elongated (20′ by 120′) and lies at the outskirts of the giant (~ 20°) molecular cloud complex which includes Orion A, Orion B, and Mon R2.

---

[3] In L1599, CO(2-1) strips were made at several adjacent velocities. The data from several strips were averaged to yield wider velocity coverage.

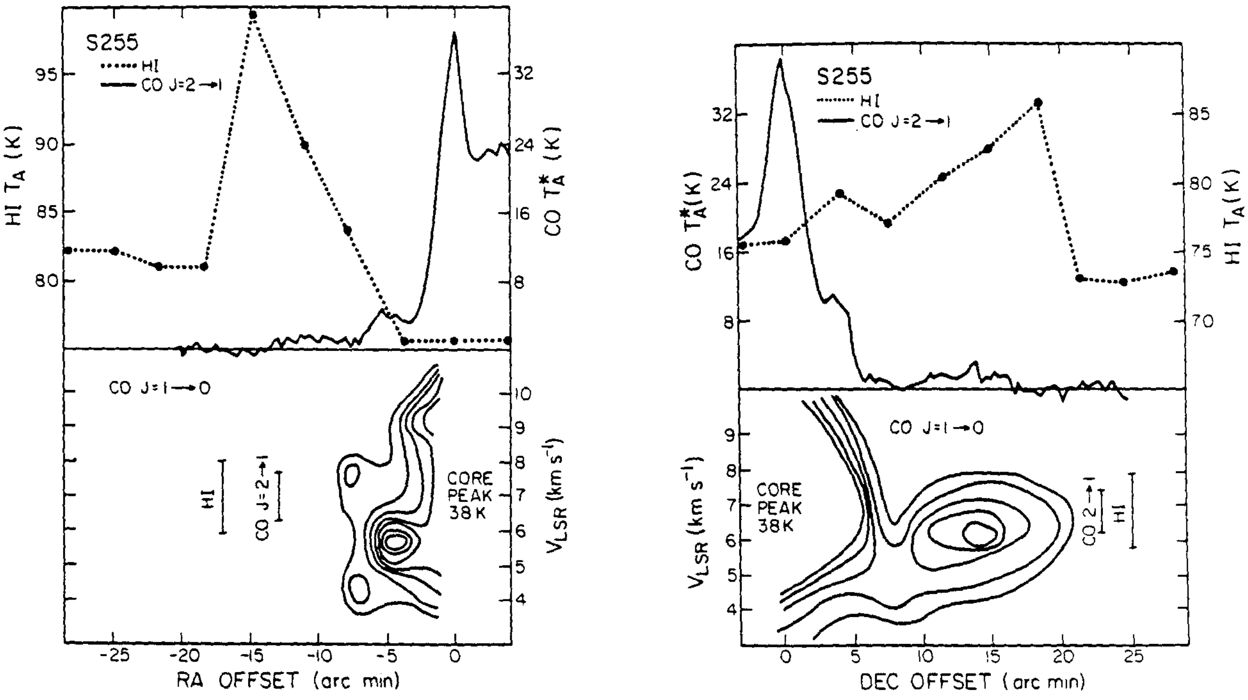

FIG. 1*a* FIG. 1*b*

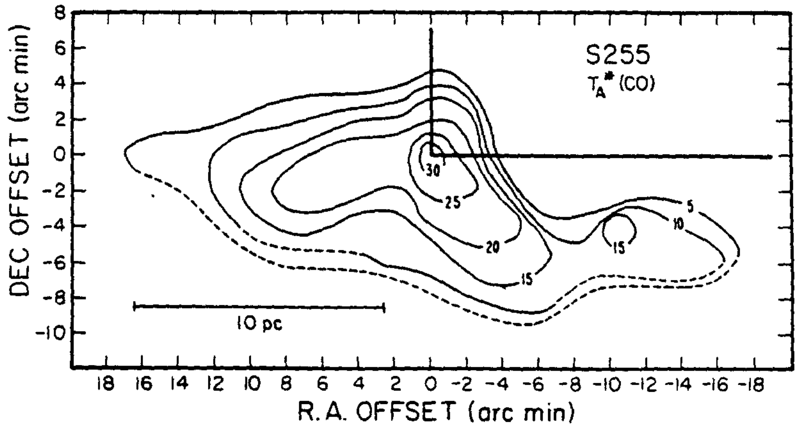

FIG. 1*c*

FIG. 1.—Right ascension (*a*) and declination (*b*) maps of S255 show clear evidence for H I emission at the CO cloud boundary, though spatially unresolved due to the large (~ 2.5 kpc) distance to this object. The H I and CO(2–1) intensities are those at $v_{\rm lsr}$ = 7 km s^{-1}, with velocity coverages shown at the bottom. The CO(1–0) T_A^* contour levels are 7.5, 6.5, 5.5, 4.5, 3.5, 2.5, and 1.5 K. The locations of the strips relative to the molecular cloud are shown in (*c*), taken from Evans, Blair, and Beckwith (1977).

It borders on the λ Orionis H II region (S264) and is apparently affected (flattened and presumably ionized) at its inner boundary by its interaction with the H II region. The apparent interaction allows for a good distance determination (that to the ionizing star), which is 400±40 pc (Murdin and Penston 1977).

Two strips, cutting across the narrow dimension of the cloud at a position angle of 135°, were mapped in H I and CO(2–1). These are shown in Figure 3 together with a low-resolution (8′) map of the entire cloud from Maddalena *et al.* (1983). The H I map of L1599-B traverses the entire cloud and therefore passes across

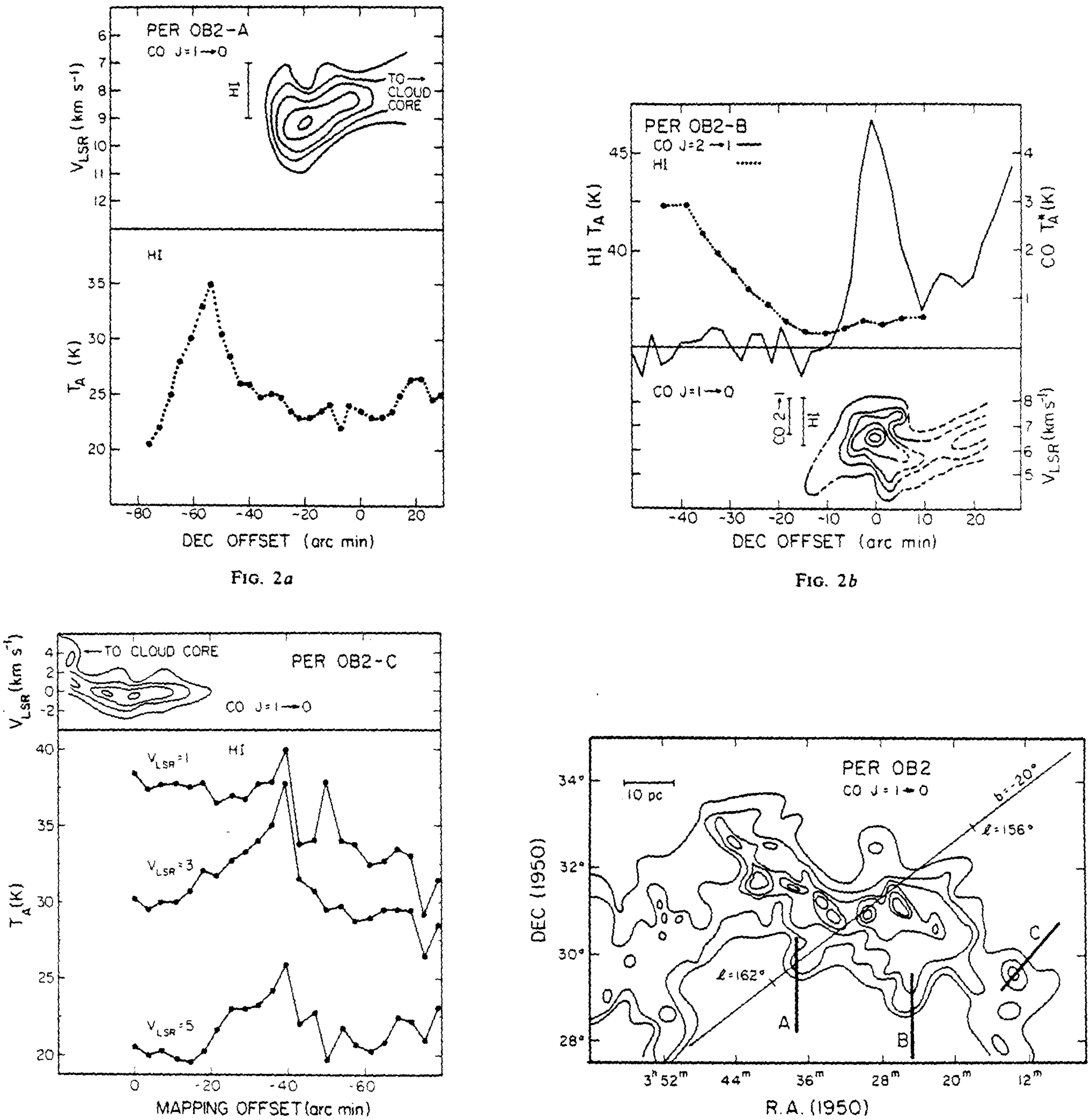

FIG. 2*a*

FIG. 2*b*

FIG. 2*c*

FIG. 2*d*

FIG. 2.—Strip maps for Per OB2-A, B, and C are shown along with locations of the strips on a CO(1–0) integrated intensity map (*d*) by Baran (1982). The Per OB2-C strip was made at a position angle of 135°. Because of the proximity of this source, the H I halo seen in (*a*) and (*c*) is well resolved. It is argued that the rise in H I emission in (*b*) must also reach a maximum within 2° of the boundary, though off the end of the present strip. The H I and CO(2–1) velocity coverages are shown on the CO(1–0) contour maps in (*a*) and (*b*). In (*c*), H I intensities in three 2.1 km s^{-1}-wide filters (v_{lsr} = 1, 3, and 5 km s^{-1}) are plotted since the velocity of the molecular gas decreases from ~ 4 km s^{-1} to ~ 0 km s^{-1} as the cloud edge is approached. Contours of CO(1–0) T_A^* are (*a*) 3.25, 2.75, 2.25, 1.75, and 1.25 K; (*b*) 7.3, 5.8, 4.3, 2.8, and 1.3 K; and (*c*) 4.0, 3.0, 2.0, and 1.0 K. Contour levels in (*d*) are 30.0, 22.5, 15.0, 7.5, 4.5, and 1.5 K km s^{-1}.

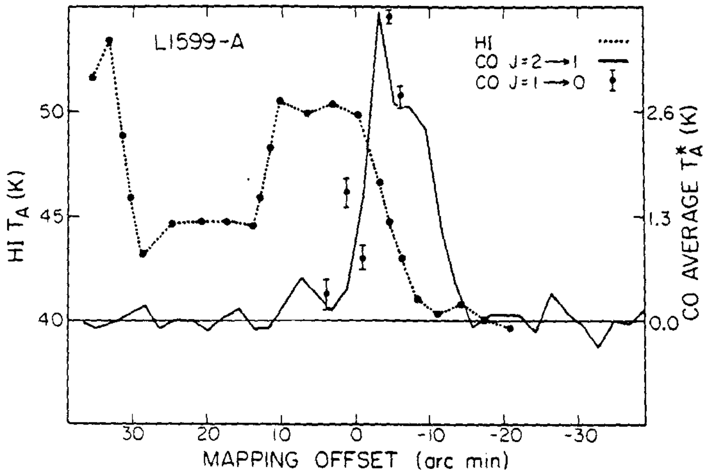

FIG. 3*a*

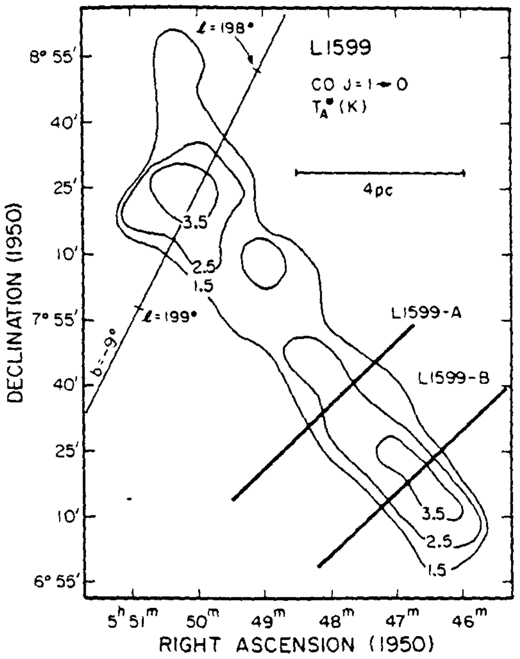

FIG. 3*c*

FIG. 3.—CO(2–1) and H I maps for the L1599 strips along with a low-resolution CO map of Maddalena *et al.* 1983. This elongated cloud borders on the λ Orionis H II region, and one side (on the right in the figures) may be near an ionization front. There is a distinct H I peak in L1599-B at both CO edges, and a similar peak is seen in L1599-A along with an additional peak apparently unrelated to the dense cloud. Both of the strips are at a position angle of 135° (R.A. increasing to the left) in order to cut across the narrow dimension of the cloud. The H I filter width was 2.1 km s^{-1} centered at $v_{\rm lsr}$ = 10.0 km s^{-1}. For L1599-A, the CO(1–0) and the CO(2–1) data are averages over several adjacent, narrow channels yielding an effective resolution of 2.3 km s^{-1} and centered at $v_{\rm lsr}$ = 10.3 km s^{-1}. For L1599-B, a single CO(2–1) filter covering 2.6 km s^{-1} was centered at $v_{\rm lsr}$ = 9.6 km s^{-1}.

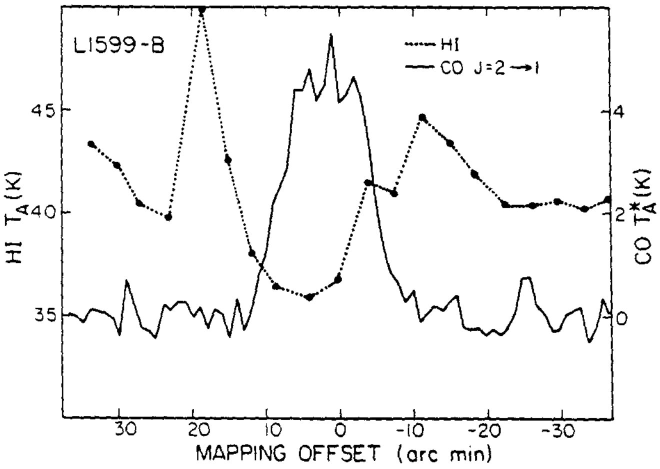

FIG. 3*b*

two CO boundaries, that bordering on the λ Orionis H II region being on the right in Figure 3*c*. At each of the boundaries, there is a distinct H I peak, reaching a maximum ~ 5′ from the CO edge. The strip L1599-A (passing across the boundary opposite to the H II region) also has an H I peak at the CO edge but, in addition, has a second peak 30′ from the cloud edge which has no clear association with the L1599 cloud.

d) *Monoceros OB1*

The molecular cloud associated with the Mon OB1 association has been studied by Blitz (1978). It is located near the galactic plane (b = 1°4) at a latitude of 199°. Using a distance of 900 ± 200 pc from Racine (1968, and references therein), the observations of Blitz yield a cloud mass of 2–4 × 10^5 $M_\odot$. Clearly, the region is a site of active star formation, being associated with the foreground cluster NGC 2264 and the reflection association Mon R1. A patchy, diffuse H II region at larger *l* extends near, but probably not up to, the observed cloud edge.

The single strip map across the cloud edge is shown in Figure 4 along with a low-resolution (8′) map of Blitz (1978) showing the general CO distribution. The best indication of the CO cloud boundary is shown by the contour map of CO(1–0), and an H I emission spike is evident near the boundary. Farther away from the H I peak, the H I emission intensity continues to rise, up to the end of the strip. These intensity changes are local, since the Berkeley survey (Weaver and Williams 1974*a*) shows constant temperature to within ~ 5–10 K in Mon

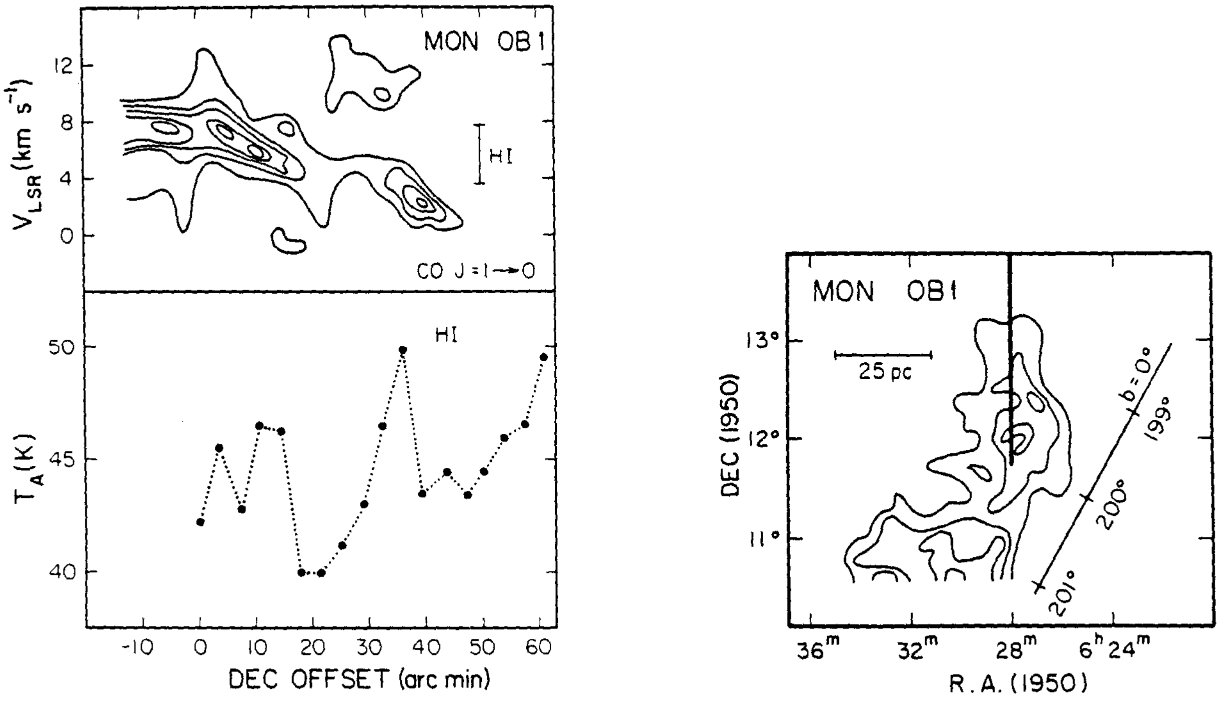

FIG. 4a FIG. 4b

FIG. 4.—The Mon OB1 cloud is an active star-formation region associated with the foreground cluster NGC 2264. The strip passes across one CO edge and shows a sharp H I peak at that point, but the H I data are not extensive enough to determine whether or not the rise at the right of the figure continues. Low-resolution data suggest that it does not. The H I declination map of Mon OB1 was made at $v_{\rm lsr}$ = 5.6 km s^{-1}. Some of the irregularity in this map may be due to the fairly complicated velocity field in Mon OB1, as seen in the CO contour map. Contours of CO(1–0) T_A^* are 5.0, 4.0, 3.0, 2.0, and 1.0 K. In (*b*) the map of Blitz (1978) shows the location of the strip map and gives the integrated CO(1–0) intensity in contours of 4, 3, 2, and 1 K-Mhz.

OB1 over several degrees at 0°6 resolution. The existence in our plot of several H I peaks toward this cloud edge may be due to the confused velocity structure near the cloud periphery. In retrospect, this cloud edge is a poor choice for our purposes because of ambiguities introduced by the complex velocity field.

e) *Monoceros Filament*

Mon filament, like L1599, is an isolated cloud ($b \sim -5°$) associated with the giant molecular cloud complex in Orion (but straddling the boundary with Monoceros). It has been mapped in CO(1–0) by Maddalena *et al.* (1983), who find it to be part of a long (10°), narrow, E-W feature at an angle of ~ 60° to the galactic plane. Because of its unusual kinematic behavior (abrupt variations in radial velocity and large line widths), they suggest that the cloud may be a streamer of gas connecting the giant dense clouds in the Orion region to the galactic plane. Mon filament has no bright rims or other obvious interaction with H II gas. The distance to Mon filament is inferred from its association with the Orion complex to be 500 pc (+500, −300).

The single strip map (Fig. 5) was chosen so as to traverse the filament. The H I strip shows a marked and general rise beyond both of the CO cloud boundaries but has no apparent H I peak. For this particular source, the presence of an H I halo could easily be masked by its peculiar kinematics (see § IV). As was the case with Per OB2-B, low-resolution H I observations (Weaver and Williams 1974*a*) show that the H I intensity subsequently decreases several degrees away on either side of the source. Apparently, a more extended, high-resolution H I strip is needed in order to clearly delineate any H I peaks associated with the cloud edges. In addition to its H I behavior outside of the CO cloud boundaries, Mon filament is the one source in this survey which displayed a distinct H I self-absorption feature on the central dense portion of the cloud. The 21 cm absorption dip appeared in three of the spectra, causing a local dip of ~ 5 K in the H I strip map. For several reasons, the general rise in H I intensity off the cloud is unlikely to be caused by absorption of background H I emission by cool H I in the molecular cloud. First of all, the general increase in Figure 5 continues well beyond the known CO boundary. Second, the H I self-absorption is

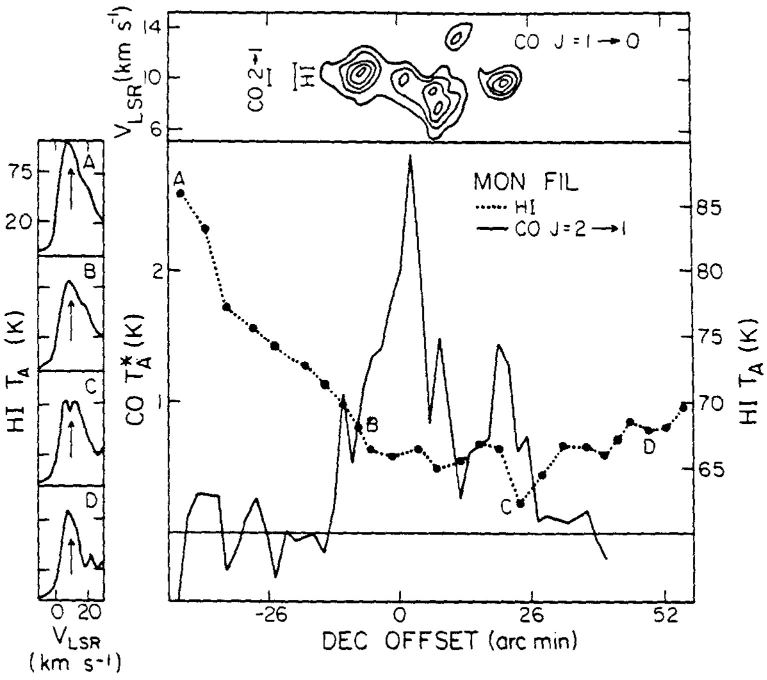

FIG. 5*a*

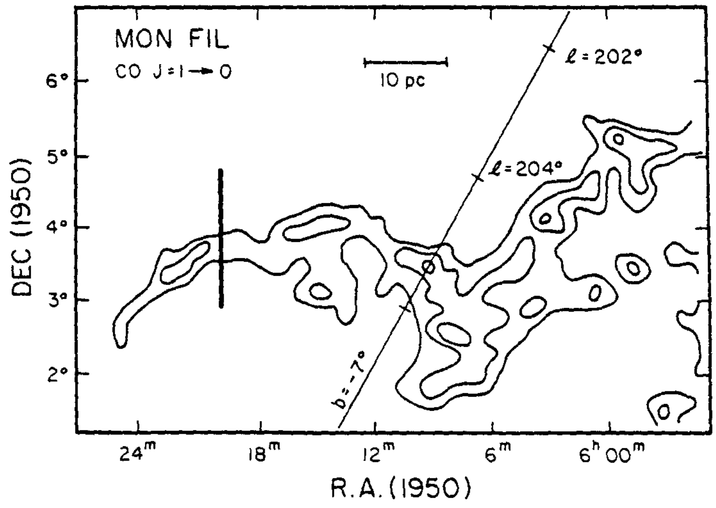

FIG. 5*b*

FIG. 5.—Mon filament is part of an elongated cloud at the periphery of the giant molecular cloud complex containing the Orion molecular clouds. The declination strip passes across the narrow dimension of this filament, and the H I and CO(2–1) data, centered at v_{lsr} = 10.0 km s^{-1}, represent filter widths of 2.1 and 1.3 km s^{-1}, respectively. H I spectra at four labeled positions are presented to illustrate the narrow self-absorption toward position C at v_{lsr} = 10.0 km s^{-1} (*arrows*). This instance of self-absorption is the only obvious case in the present survey. The CO(1–0) T_A^* contour levels are 5.0, 4.0, 3.0, 2.0, and 1.0 K. In (*b*) the location of the strip map is shown on a map taken from Morris, Montani, and Thaddeus (1980). CO(1–0) T_A^* contours in (*b*) are 5.1, 3.4, and 1.7 K.

TABLE 2

HALO PROPERTIES

	OBSERVED			DERIVED		
SOURCE	T_A(bg) (K)	T_A(edge) (K)	ΔR (res)[a] (pc)	T_{bg} (K)	T_{min} (K)	N_{min} (10^{20} cm^{-2})
S255-RA	82	100	3.6(2.6)[b]	109	145	1.62
S255-Dec	72	85	7.3(2.6)	97	120	0.98
Per OB2-A	20	35	2.0(0.4)	27	53	1.13
Per OB2-B	36[c]	42	> 1.5[d](0.4)	48	61	0.49
Per OB2-C	29	38	1.8(0.4)	39	55	0.64
L1599-A	44	50	1.4(0.4)[e]	59	71	0.44
L1599-B	41	50	0.5(0.4)[b]	55	74	0.78
L1599-B	40	45	0.7(0.4)[b]	54	65	0.39
Mon filament ...	66[c]	85	> 3.5[d](0.5)	88	118	1.32
Mon filament ...	66[c]	70	> 3.5[d](0.5)	88	97	0.29
Mon OB1	42[c]	50	1.8[d](0.9)[b]	57	73	0.64

[a] H I halo thickness FWHM estimated from Arecibo 21 cm data. Resolution of Arecibo beam in pc is given in parentheses.

[b] May be underresolved.

[c] Temperature on cloud; T_A(bg) not observed directly.

[d] H I halo boundaries unclear in 21 cm data.

[e] If second H I peak farther away from cloud is included, $\Delta R > 3.5$ pc.

only apparent on the spectra for three positions where there is a local dip in the H I strip map. Finally, other H I surveys of molecular clouds show self-absorption only toward regions of high molecular column density near the cloud cores (McCutcheon, Shuter, and Booth 1978; Knapp 1974).

The presence of H I self-absorption could seriously complicate our analysis because we are comparing the CO emission with only a single 21 cm velocity channel, and H I self-absorption features are typically 1–3 km s^{-1} wide (McCutcheon, Shuter, and Booth 1978; Knapp 1974). We have checked our H I data for evidence of self-absorption by cold H I. The only narrow minimum (coincident with the CO cloud velocity) found in our sample of sources was the one shown in Figure 5 (Mon fil). We conclude that our observations are relatively unaffected by H I self-absorption.

IV. ANALYSIS

The nine maps in Figures 1–5 contain information about 11 cloud edges. At (or beyond) all 11 CO boundaries, the 21 cm intensity rises as the CO emission (and visual extinction) falls. At six of the boundaries (in S255-RA, S255-Dec, L1599-B, Per OB2-A, and Per OB2-C), the H I maps show distinct single emission peaks at the cloud edge. At two edges (in L1599-A and Mon OB1) there is an emission peak, but the H I emission continues to rise beyond the peak. At the remaining three edges (in Mon filament and Per OB2-B), there is a smooth rise in the H I intensity, and comparison with lower spatial resolution H I surveys shows that beyond the end of our strip maps, the intensity decreases. We interpret these results as indicating the presence of H I halos around most of the molecular clouds studied.

In order to estimate the statistical significance of these results, we examined the H I spectra at velocities offset from the molecular gas by either 6 or 12 km s^{-1}, depending on the CO line widths. The velocity offsets exclude all CO emission but are small enough so the H I intensity, due primarily to the galactic background, is within 40% of the intensity at the CO cloud velocity. In each strip maximum and minimum H I intensities were recorded for all positions farther from the CO cloud than the CO boundary at $T_A^*(\mathrm{CO}) = 1$–2 K. These contrasts in T_A(H I) were then compared with the quantity T_A(edge)$-$$T_A$(bg) taken from Table 2 for the nine edges. This comparison should be a good indication of how the random fluctuations in the H I background might mimic H I halos. The strips L1599-A and Mon OB1 were not analyzed because fluctuations in the CO intensity made the unambiguous assignment of a CO boundary difficult.

At the nonmolecular velocities, the average contrast is 3.1 K ($\sigma = 6.4$ K) for the largest fluctuation, while at the molecular velocity, the corresponding value is 10.9 K ($\sigma = 5.6$ K).

The standard error of the difference between these two mean values would be 3.0 K if the two samples were from the same population (e.g., if our halo observations were simply a manifestation of random H I fluctuations). Hence they differ by 2.6 standard errors, and the probability for this is less than 1%. Despite the small sample, we believe our results are statistically significant. It is highly improbable that random H I intensity fluctua-

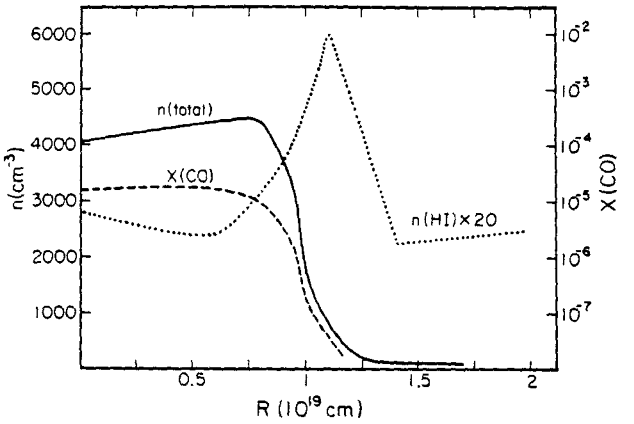

FIG. 6

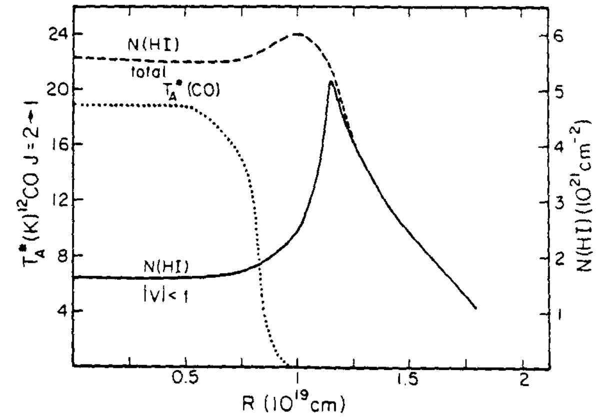

FIG. 7

FIG. 6.—Theoretical cloud model results from the work of Gerola and Glassgold (1978). Total density, CO abundance, and H I density are plotted as functions of radial distance from cloud core. These relations were used as input to the Monte Carlo CO intensity and H I column density computations shown in Fig. 7.

FIG. 7.—The computed CO(2–1) intensity from a Monte Carlo radiative transfer model is plotted as a function of projected radial distance from cloud core as seen from Earth. The H I column density is shown, calculated from Fig. 6, for two velocity ranges: $-1 < v_{\rm lsr} < 1$ (corresponding to a single Arecibo spectrometer channel) and $-7.5 < v_{\rm lsr} < 7.5$, which includes all cloud velocities in the model of Gerola and Glassgold.

tions are responsible for our observations of H I increases near cloud edges.

Atomic-to-molecular transition zones have been discussed by several authors (see § I), most recently by Gerola and Glassgold (1978, hereafter GG) as part of a model following the entire evolution of a gravitationally collapsing interstellar cloud. The particular model discussed starts as a spherical cloud of radius 11 pc, mass $2 \times 10^4\ M_\odot$, initial density 150 cm^{-3}, and initial temperature 100 K. In the cloud interior, heating and cooling mechanisms and chemical reactions are followed in a self-consistent, one-dimensional hydrodynamic model. The results of the GG model, their "warm" case,[4] are reproduced in Figure 6, which gives the variation of total density, CO density, and neutral hydrogen density with distance after an evolution time of 0.9 t_f, where t_f is the initial free-fall time (3.6×10^6 yrs). The cloud radius is about 3 pc. The total density and CO density fall off abruptly at the cloud edge, and slightly farther out there is a sharp peak in H I density.

We have performed a non-LTE, 10-level radiative transfer calculation using a Monte Carlo computer code (Bernes 1979) to see what CO emission would be expected from such a molecular cloud. The input to this calculation was essentially the model of GG, including the collapse velocity, which could be approximated over most of the cloud by the formula

$$v_r = -1.5 r \text{ km s}^{-1},$$

where r is in pc. Near the cloud edge, however, the magnitude of the collapse velocity begins to decrease.

Figure 7 displays the calculated CO(2–1) line intensity and H I column density as a function of (projected) distance from the cloud core. The H I column density was integrated over a bandwidth of 2 km s^{-1}, corresponding to a single channel from an Arecibo spectrum, and over a bandwidth of 15 km s^{-1}, which essentially includes all velocities. The primary significance of the model calculations is that they predict a distinct H I halo at the CO cloud boundary. The modeled H I and CO line intensities, as well as their spatial extents, vary to some extent with the adopted initial conditions. However, the observed H I halos are consistent with reasonable starting conditions.

It is important to understand the significance of the two different H I column densities. Because the clouds were assumed to have circular cross sections, the *total* H I column density does not display a sharp peak at the CO cloud boundary. It is the assumed kinematic model (slow collapse), in combination with the H I distribution, which produces the marked maximum in H I column density at the cloud rest velocity. For certain clouds, such as the Monoceros filament, the lack of a sharp emission spike at the cloud velocity might be attributable to their unusual kinematics and may not preclude the presence of actual H I halos.

For a uniform cloud filling the antenna beam, the observed H I intensity (in excess of the background continuum) is

$$T_B = T_{\rm bg} e^{-\tau} + (T_s - T_c)(1 - e^{-\tau}),$$

where $T_{\rm bg}$ is the background H I emission (typically 80–100 K), T_c is the continuum galactic emission, which

---

[4] GG consider two cases, a "warm" case, which includes a ~50% efficiency for heating of the gas by the H_2 formation heating, and a "cool" case, which does not consider heating by H_2 formation on grains. Our discussion of the GG model always refers to the warm case.

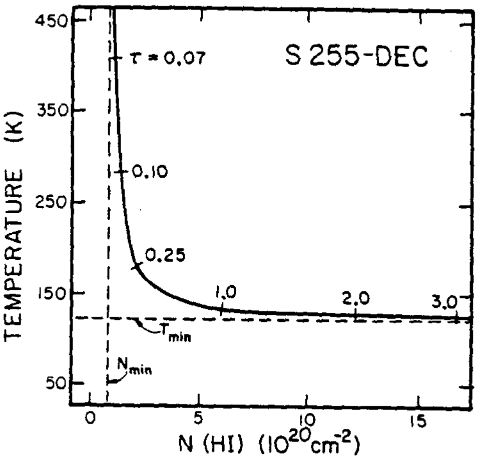

FIG. 8.—The range of permissible values of spin temperature and H I column density is illustrated, for the S255-Dec halo, for various values of τ, the H I opacity. The relationship between T and $N_{\rm H\,I}$ is derived in the manner described in the text from the observed increase in 21 cm intensity near the cloud edge over the general galactic background 21 cm intensity.

we assume to be equal to 3 K, and T_s is the H I spin temperature. Because the cloud halos always appear as bright features against the galactic background H I emission, we know that $T_s > T_c + T_{\rm bg}$ regardless of the optical depth. The minimum column density $N_{\rm H\,I}$ (cm^{-2}) of the halo gas can be found simply from the optically thin limit to be (Spitzer 1978)

$$N_{\rm min} = 1.94 \times 10^{18} \Delta v (T_B - T_{\rm bg}) ,$$

where the (Gaussian) line width, Δv, is expressed in km s^{-1}. Similarly, the minimum spin temperature, $T_{\rm min}$, is found from the optically thick limit, namely,

$$T_{\rm min} = T_B + T_c .$$

In order to obtain T_B from the actual antenna temperatures, T_A, a beam-source coupling correction is applied to the observed excess antenna temperatures (above $T_{\rm bg}$) in keeping with the observed halo widths and the known antenna sidelobe pattern. For intermediate optical depths, the halo kinetic temperature and column density can be related, and the results, for one source, are shown in Figure 8. For this source, S255-Dec, the beam-corrected galactic background, $T_{\rm bg}$, is 97 K, and the beam-corrected cloud edge temperature is 120 K, which equals $T_{\rm min}$. The column density $N_{\rm min}$ is 0.98×10^{20} cm^{-2}. Table 2 lists for all the cloud-edge sources values of the observed galactic background temperature, T_A(bg), the observed cloud edge temperature, T_A(edge), the observed cloud halo thickness in H I, ΔR, and the derived quantities $T_{\rm bg}$, $T_{\rm min}$, and $N_{\rm min}$.

V. DISCUSSION

When the values ΔR, $T_{\rm min}$, and $N_{\rm min}$ in Table 2 are compared with the specific model of GG, the observed halo thicknesses ($\Delta R \sim 0.5$ to several pc) and minimum H I column densities ($N_{\rm min} \geq 2 \times 10^{19}$ cm^{-2}) are found to be consistent with the model expectations. The increase of kinetic temperature in the H I halo, however, is larger than predicted by GG, but this is probably due to the relatively high density of their model halo and to the low resolution of their numerical calculations in the peripheral regions of the clouds.

A more general comparison can be made with the parameterized models of FGK. These authors discuss the thickness of the H_2/H I transition zone and give abundance profiles which depend strongly on the dimensionless quantity representing the ratio of the formation and destruction rates of H_2 at the surface:

$$\varepsilon = 2 \langle n_{\rm H} \rangle R_1 / (G_d^0) .^5$$

Here, $\langle n_{\rm H} \rangle$ is the average density (cm^{-3}) of hydrogen atoms in the form of H I and H_2 in the transition zone, G_d^0 is the photodissociation rate at the surface of the cloud, and R_1 is the formation rate of molecular hydrogen on the surface of grains such that $R_1 n_{\rm H\,I} n_{\rm H}$ is the formation rate in cm^{-3} s^{-1}. The length scale of the transition zone is then

$$L_{\rm tr} = 9.5 \times 10^{-5} \varepsilon^{-1.4} \langle n_{\rm H} \rangle^{-1} \text{ pc.}$$

FGK also show that ε is related to $N_{\rm H}$ in the transition zone (note that $N_{\rm H}$ is nearly equivalent to $N_{\rm H\,I}$ in the transition zone). From Table 2, we see that typical minimum values for $N_{\rm H\,I}$ are $\sim 10^{20}$; this corresponds to $\varepsilon \sim 2 \times 10^{-4}$ (from FGK, Fig. 2), giving

$$L_{\rm tr} \sim 14 \langle n_{\rm H} \rangle^{-1} \text{ pc.}$$

We can estimate $\langle n \rangle$ from the quantity $f N_{\rm min} / \Delta R$, where $N_{\rm min}$ and ΔR are from Table 2, and f is a geometrical factor to account for the fact that $N_{\rm min}$ is measured "edge-on" instead of directly "head-on" through the H I halo. In the spherically symmetric GG model, $f \sim 0.2$; comparison of our measured values of ΔR to the corresponding overall cloud dimensions (Table 2 and the low-resolution maps in Figs. 1–5) yields a range of 0.1–1 for f, with some dependence on somewhat uncertain source geometries. The average value of $N_{\rm min}/\Delta R$ (Table 2) is 16 pc; for $f \sim 0.1$–1.0, we compute $L_{\rm tr} \sim 1$–9 pc, certainly consistent with our observed range of ΔR in Table 2. These calculations, however, indicate that $\langle n \rangle$ could be as low as 10–100 times less than the density in the GG model, but since we can measure only $N_{\rm min}$, these are lower limits for $\langle n \rangle$.

The minimum temperatures which we derive for H I halos (≥ 100 K) are considerably larger than those computed by GG (40 K even for their warm case). The dominant heat-loss mechanism, line radiation from

---

[5] This expression makes implicit assumptions about the mechanism of H_2 formation on grains which are fully discussed by Hollenbach, Werner, and Salpeter (1971).

ionized carbon, is given by Spitzer (1978) as

$$\lambda = 7.9 \times 10^{-27} n_H^2 d_C e^{-92°/T} \text{ ergs cm}^{-3} \text{ s}^{-1},$$

where d_C is the carbon abundance relative to the cosmic abundance. The large observed (minimum) kinetic temperatures could therefore result either from an increase in the assumed heating, a decrease in the space density below that assumed by GG, or a decreased carbon abundance.

The molecular cloud models of de Jong, Dalgarno, and Boland (1980) do have surface temperatures large enough to just account for our observed lower limits; the difference between the two models being the authors' choices of heating and cooling parameters. Enhancements of the kinetic temperature at the surfaces of molecular clouds also appear in the work of Clavel, Viala, and Bel (1978) and Oppenheimer and Dalgarno (1975). Of course, the kinetic temperatures derived from the present observations are lower limits, and the actual kinetic temperatures may be larger, indicating a space density lower than those used in the models. Such a result is in agreement with the observed limits on the H I column density.

Observationally, there have been a few previous indications that molecular clouds are warmest at their edges. Snell (1981) finds from an analysis of ^{12}CO and ^{13}CO spectra in several dark clouds that the temperatures in the outer regions of clouds rise rapidly to values greater than 50 K. Similarly, a model by Young *et al.* (1982) of CO emission in the dark cloud B5 suggests that the CO edge (~ 40 K) is much warmer than the cloud center (~ 15 K). The temperatures of the CO cloud edges are all lower than those observed in the H I halos. Apparently, the kinetic temperature continues to rise beyond the warm molecular surfaces.

VI. CONCLUSIONS

Based on observations of five molecular clouds, it appears that warm H I halos, from 0.5 to several pc in extent, form at or slightly beyond the CO boundaries of dense clouds. The appearance of the halos in emission against the ~ 80 K background galactic H I emission implies halo kinetic temperatures well above temperatures in the denser molecular gas, even the warm molecular gas observed at the outer edges of dense clouds. The spatial extents and observed column densities of the halos agree well with those based on steady state calculations which balance the formation of H_2 against its destruction by ambient UV radiation. The process forms a distinct boundary layer of H I by virtue of the simultaneous need for high density (to get a suitably large neutral column density) and low visual extinction (to allow for the destruction of H_2).

Observations of the submillimeter transitions of atomic and ionized carbon should be used to improve our picture of cloud edges. In addition, further H I observations are needed to improve the statistical significance of our sample. Do all molecular clouds indeed have H I linings?

We are indebted to G. Baran for providing unpublished data and to A. Glassgold, P. Goldreich, and R. Dickman for helpful comments. The anonymous referee also made several valuable suggestions. This work was funded in part by National Science Foundation grants AST-80-16863 to the California Institute of Technology and AST-81-14716 to the Columbia University. One of us (M. M.) would like to thank the UCLA Astronomy Department for their hospitality while the manuscript was being prepared.

REFERENCES

Baran, G. P. 1982, Ph.D. thesis, Columbia University.
Bernes, C. 1979, *Astr. Ap.*, **73**, 67.
Blitz, L. 1978, Ph.D. thesis, Columbia University.
Blitz, L., and Thaddeus, P. 1980, *Ap. J.*, **241**, 676.
Bridle, A. H., Davis, M. M., Fomalont, E. B., and Lequeux, J. 1972, *A.J.*, **77**, 405.
Clavel, J., Viala, Y. P., and Bel, N. 1978, *Astr. Ap.*, **65**, 435.
de Jong, T., Dalgarno, A., and Boland, W. 1980, *Astr. Ap.*, **91**, 68.
Evans, N. J., II, Blair, G. N., and Beckwith, S. 1977, *Ap. J.*, **217**, 448.
Federman, S. R., Glassgold, A. E., and Kwan, J. 1979, *Ap. J.*, **227**, 466 (FGK).
Field, G. B., Sommerville, W. B., and Dressler, K. 1966, *Ann. Rev. Astr. Ap.*, **4**, 226.
Gerola, H., and Glassgold, A. E. 1978, *Ap. J. Suppl.*, **37**, 1 (GG).
Glassgold, A. E., and Langer, W. D. 1975, *Ap. J.*, **197**, 347.
Hollenbach, D. J., Werner, M. W., and Salpeter, E. E. 1971, *Ap. J.*, **163**, 165.
Knapp, G. R. 1974, *A.J.*, **79**, 527.
Maddalena, R., Morris, M., Thaddeus, P., and Moskowitz, J. 1983, in preparation.
McCutcheon, W. H., Shuter, W. L. H., and Booth, R. S. 1978, *M.N.R.A.S.*, **185**, 755.
Morris, M., Montani, J., and Thaddeus, P. 1980, in *IAU Symposium 87, Interstellar Molecules*, ed. B. H. Andrew (Dordrecht: Reidel), p. 197.
Murdin, P., and Penston, M. V. 1977, *M.N.R.A.S.*, **181**, 657.
Oppenheimer, M., and Dalgarno, A. 1975, *Ap. J.*, **200**, 419.
Racine, R. 1968, *A.J.*, **73**, 233.
Sargent, A. I. 1979, *Ap. J.*, **233**, 163.
Savage, B. D., Bohlin, R. C., Drake, J. F., and Budich, W. 1977, *Ap. J.*, **216**, 291.
Sharpless, S. 1959, *Ap. J. Suppl.*, **4**, 257.
Snell, R. L. 1981, *Ap. J. Suppl.*, **45**, 121.
Spitzer, L. 1978, *Physical Processes in the Interstellar Medium* (New York: Wiley).
Weaver, H., and Williams, D. R. W. 1974*a*, *Astr. Ap. Suppl.*, **17**, 1.
______. 1974*b*, *Astr. Ap. Suppl.*, **17**, 251.
Werner, M. W. 1970, *Ap. Letters*, **6**, 81.
Young, J. S., Goldsmith, P. F., Langer, W. D., Wilson, R. W., and Carlson, E. R. 1982, *Ap. J.*, **261**, 513.

Stephen M. Lichten and Peter G. Wannier: Department of Astronomy, 105-24, California Institute of Technology, Pasadena, CA 91125

Mark Morris: Astronomy Department, Columbia University, Box 98, Pupin Labs, New York, NY 10027

APPENDIX A

H I Halo Mass and Molecular Cloud Turbulence

Are molecular clouds, in general, massive enough to satisfy the virial theorem? This question is disputed in the literature. Orion and Monoceros are not gravitationally bound, according to Thaddeus (1982), "unless they are surrounded by fairly massive and so far unobserved H I halos," since the CO determined masses of six clouds in these complexes are systematically lower than their virial masses by a factor of about 2.5 . There is considerable uncertainty, however, in CO determined cloud masses, which entail 1) conversion from CO column density, or integrated intensity, to H_2 column density, and 2) conversion from H_2 column density to H_2 mass. Cloud geometry, density structure, and relative CO/H_2 abundance are all possible sources of error. Each of these uncertainties amounts to a factor of 2-3. Blitz (1979) mapped 14 giant molecular cloud complexes in CO and claims they are probably gravitationally bound. Baran (1982) studied 7 giant molecular clouds in CO and finds, on the average, that the CO determined mass is slightly larger than the virial mass. Baran (1982) also speculated that additional cloud mass might be present in the form of "unseen" H I. Solomon and Sanders (1979) concluded from their survey of giant molecular clouds that these objects are generally gravitationally bound.

Having detected H I envelopes at molecular cloud edges, we are now in a better position to assess their contribution to the total mass of the nebulae. Knowledge of the appropriate source geometry as well as the column density measured perpendicularly through the H I halo is required for an explicit calculation. We can only estimate the geometry from our projected view of the molecular cloud. The lower limit to the column density is fN_{min}, where f is a geometrical factor between 0.1 and 1 (f=0.2 for a sphere; see §V.) and N_{min} is from Table 2. We can therefore calculate the following lower limits for H I halo masses: $10^3 f$ M_o (S255), $2.5X10^3 f$ M_o (Per OB2), 21f M_o (L1599), $3.5X10^2 f$ M_o (Mon OB1), and $8X10^2 f$ M_o (Mon fil). The overall molecular cloud masses are: 10^4 M_o (S255), 10^4 M_o (Per OB2), $1.3X10^3$ M_o (L1599), $3X10^5$ M_o (Mon OB1), and 10^4 M_o (Mon fil; Thaddeus 1982). Although the H I halo masses here are lower limits, it should be noted that if they were more than a factor of about ten higher, the H I halos would be highly opaque (see Figure 8, for example). Furthermore, for most common geometries (such as spheres, cylinders), the factor f is considerably less than unity. Therefore we conclude, on the basis of this limited cloud sample, that the H I halos we have detected probably contain only a small fraction of the total mass of these nebulae, and they make little contribution towards gravitationally binding molecular clouds.

These results cast doubt on Larson's (1981) suggestion that supersonic turbulent motions in molecular clouds are derived from subsonic turbulent motions present in much warmer, massive atomic envelopes; instead, internal sources of turbulent energy are likely to play a major role in molecular cloud internal kinematics.

References

Baran, G.P. 1982, unpublished Ph.D. thesis, Columbia University.

Blitz, L. 1979, in Giant Molecular Clouds in the Galaxy, ed. P.M. Solomon and M.G. Edmunds (Oxford: Pergamon), p. 1.

Larson, R.B. 1981, M.N.R.A.S., 194, 809.

Solomon, P.M., and Sanders, D.B. 1979, in Giant Molecular Clouds in the Galaxy, ed. P.M. Solomon and M.G. Edmunds (Oxford: Pergamon), p. 41.

Thaddeus, P. 1982, in Symposium on the Orion Nebula to Honor Henry Draper, ed. A.E. Glassgold, P.J. Huggins, and E.L. Schucking (N.Y.: N.Y. Academy of Sciences).

CHAPTER 4

AUTOCORRELATION MEASUREMENTS OF INTENSITY FLUCTUATIONS IN MOLECULAR CLOUDS

ABSTRACT

Autocorrelation and statistical analyses of ^{13}CO intensity fluctuations are used in this paper to investigate supersonic turbulence in several molecular clouds. The data are sensitive to spatial scales of 0.04–80 pc and are consistent with the presence of tens to hundreds of turbulent fragments, or cells, within each molecular cloud. A typical fragment size is a few tenths of a pc (much less than the cloud dimensions), and the internal velocity dispersion within each fragment is significantly less than the velocity dispersion of the entire cloud. Relative supersonic velocities between fragments make the molecular radio lines much broader than expected thermal line widths. We discuss several sources of energy which could power this turbulence over cloud lifetimes. In some sources, we also find evidence for systematic large-scale flows. However in cloud cores, random motions appear to dominate the kinematics.

I. INTRODUCTION

The importance of turbulence in astrophysics has been recognized for several decades in theoretical discussions (Chandrasekhar 1949). Observational studies have emphasized spatial correlation techniques and have included the atomic interstellar medium (Aller 1951; Serkowski 1958; Kaplan 1966; Baker 1973), ionized nebulae (Munch 1958), and the Sun (Stuart and Rush 1954; Frenkiel and Schwarzschild 1955; Knobloch and Rosner 1981).

Turbulence within molecular clouds may critically affect the manner in which star formation proceeds (Hunter 1979; Hunter and Fleck 1982), but the existence of true hydrodynamical turbulence -- e.g. velocity fields with randomly fluctuating physical characteristics due to inertial forces and with specific statistical properties -- has always been assumed; its inclusion in molecular cloud models has never been justified. Varying amounts of turbulence are commonly invoked to bring radiative transfer calculations into agreement with millimeter-wave molecular observations (Evans 1980). In large part, the success of these models stems from the fact that radiative transfer codes based on extremely different assumptions about line-broadening mechanisms give temperatures and densities which agree to within uncertainties resulting from the unknown source geometry (White 1977). This is also why they do not do a very good job of providing information about molecular cloud internal velocity fields.

Although well known signposts — such as compact HII regions, near-infrared sources, local temperature peaks, H_2O masers and type I OH masers — mark locations in molecular clouds where star formation is taking place, the process of star formation remains an unsolved fundamental astrophysical problem. The initiation of the fragmentation process during which protostars presumably form is poorly understood. Gas velocity fields must affect star formation, but a satisfactory explanation has never been found for supersonic line widths observed in every known molecular cloud (a summary of observations through 1979 is given by Larson 1981). The origin and maintenance of these apparently universal supersonic gas motions remains a mystery, although these have been hotly debated topics in recent years (Penzias 1975). The recent discoveries of weak, broad line wings covering up to 100 km s^{-1} in extent in molecular clouds (references can be found in Lichten 1982b) further complicates the problem.

In this paper, we report the results of a detailed examination of temperature and velocity spatial variations within several molecular clouds covering a wide range of mass. Regions with and without evidence for ongoing star formation were studied. The observations presented are sensitive to turbulent scales from 0.04 to 80 pc. The aim of this work is to determine the sizes and velocity dispersions of turbulent elements in molecular clouds.

The plan of this paper is as follows: in §II., the observational procedures and methods of analysis are described. The results are presented in §III., including treatment of experimental errors and bias. Individual sources are described in §IV. Interpretation of the ^{13}CO autocorrelation functions is discussed in §V., and possible means of powering molecular cloud turbulence are compared. In §VI. we discuss observations of HC_3N lines, and §VII. contains an overall summary of conclusions from this work.

II. OBSERVATIONS AND METHODS OF ANALYSIS

The data for this study consist of ^{12}CO, ^{13}CO, $C^{18}O$, and HC_3N spectra observed in the direction of the following molecular clouds: L1529 (TMC2), L1534 (TMC1), NGC 2071, NGC 2068, The Orion Molecular Cloud, S255, and S140. Most of the analysis is based on the ^{13}CO and HC_3N observations. Table 1 lists for each source the central reference position, source distance, LSR velocity, number of ^{13}CO positions observed, maximum ^{13}CO map extent, and other molecular transitions observed.

a) Instrumentation

^{13}CO, $C^{18}O$, and ^{12}CO 2.7 and 2.6 mm data were obtained with one of three 10.4m antennas of the Caltech mm-wave interferometer during January, February, and March 1982 at the Owens Radio Observatory (OVRO) in Big Pine, California. The telescope was equipped with a liquid-helium cooled superconducting insulating superconducting (SIS) receiver and an acousto-optic spectrometer which provided 1024 channels each of width 100 kHz. Calibration was achieved by measuring relative system responses to sky, hot (ambient) loads, and liquid-nitrogen cooled loads at different elevations during the observing sessions. Since all the sources were extended in CO relative to the 1′ beam, an extended source efficiency of

0.75 was used to scale the data. Antenna temperatures are expressed as T_A^*, which is the intensity corrected for instrumental (including beam efficiency) and atmospheric losses. (The $C^{18}O$ temperatures may be slightly underestimated since this molecule is somewhat less extended than CO or ^{13}CO.)

In order to increase the spatial coverage beyond that of the OVRO data, more ^{13}CO observations were made in March 1983 with the newly resurfaced 12m NRAO antenna on Kitt Peak, near Tucson, Arizona. A cooled, Cassegrain, dual-channel mixer receiver was used in conjunction with a filter bank spectrometer yielding resolution of 100 kHz and 250 kHz simultaneously. A chopper vane calibration technique was used to correct for atmospheric attentuation and for spillover. Second-order corrections for these effects were made according to the sky opacity, which was monitored daily. The T_A^* from Kitt Peak agreed with the T_A^* from OVRO to within about 15%, so a slight correction was applied to make them equal.

Additional ^{13}CO data in the NGC 2071, NGC 2068, and surrounding Orion regions were kindly provided by Maddelena et al. (1983). These spectra were taken with the Columbia 4 ft antenna and cover a much larger region (at considerably coarser resoution) than the OVRO observations. The resolution of the Columbia filter bank spectrometer was 0.68 km s^{-1} and the antenna efficiency was 0.80 . Very short scans at 7.'5 spacing were averaged in real time to return 170 profiles spaced at 30′ intervals. Thus the Columbia data have an effective resolution of a 30′ synthesized "superbeam"; the FWHP beamwidth of the 4 ft antenna is 8′.

The HC_3N 9–8 and 11–10 lines at 3.7mm and 3.0mm were observed in April 1982 with the NRAO Kitt Peak 11m telescope prior to its resurfacing. The filter bank spectrometer was used at resolutions of 30, 100, or 250 kHz. Calibration was achieved in the same manner as for the ^{13}CO Kitt Peak observations. Relative sideband gains (which were slightly different at the two frequencies) were measured with an image rejection filter; these measurements were used to determine second-order calibration corrections. The planets were observed so that the beam size could be measured and the beam efficiency for sources comparable to or smaller than the antenna beam could be determined. Since all the HC_3N sources were comparable to the 1:3 beam, a beam efficiency of 0.60 was used to scale the intensities. This is an intermediate value between the beam efficiency for a point source and the beam efficiency for a source the size of the Sun.

All the CO and HC_3N spectra were taken by position switching. System performance and observing parameters are summarized in Table 2.

b) Autocorrelation Analysis

The ^{13}CO spectra are the data base for statistical and autocorrelation analyses designed to characterize turbulence in the molecular cloud sources. The total area covered by the OVRO/Kitt Peak maps varies from source to source, but in general, each map used for autocorrelation or statistical analysis extends over a roughly square region 3/4 degree in extent. Sampling was at 1', 3', and 5' spacings. At least once every twenty minutes, the $(\Delta\alpha,\Delta\delta) = (0,0)$ position of the source being mapped was reobserved as an intensity calibration check (all offsets in this paper are given in arcmin).

The autocorrelation function $A(\Delta r, v)$ measures the degree of correlation at velocity v between temperature fluctuations measured at positions $\underset{\sim}{r}$, $\underset{\sim}{r}'$, which are separated by distance Δr:

$$A(\Delta r, v) = \frac{\sum\limits_{r} YY'}{\left[\sum\limits_{r} Y^2 \sum\limits_{r'} Y'^2 \right]^{1/2}} ,$$

where $Y = T(\underset{\sim}{r}, v) - \langle T(v) \rangle$ and $Y' = T(\underset{\sim}{r}', v) - \langle T(v) \rangle$, T represents the observed ^{13}CO T_A^*, and $\langle T(v) \rangle = \sum T(\underset{\sim}{r}, v)/N$, the summation proceeding over the N positions. The summation is over all pairs such that $\underset{\sim}{r}$ and $\underset{\sim}{r}'$ are a distance Δr apart. Since the ^{13}CO data were sampled at fixed mapping point intervals, pairs had to be binned for various lags, Δr. There were usually 100-300 pairs in the summation for a given Δr, although at some of the larger spacings there were as many as 1500. Improvement of the signal/noise ratio in line wings was given priority over increasing the size of the maps once about 100 positions were observed. The Columbia data, however, consist of 170 spectra entirely covering NGC 2071, NGC 2068, Orion A, and Orion B.

A second autocorrelation function, $A(\Delta v)$, was computed to measure the degree of correlation, averaged over all the profiles for a source, of temperature fluctuations separated by a velocity interval, Δv. If we let $B = [T(\underset{\sim}{r}, v) - \langle T(v) \rangle]/\langle T(v) \rangle$, and $B' = [T(\underset{\sim}{r}, v') - \langle T(v') \rangle]/\langle T(v') \rangle$, where the angle brackets denote spatial averages as defined above, then the normalized brightness velocity autocorrelation function is:

$$A(\Delta v) = \frac{\sum_r \sum_v BB'}{\left[\sum_r \sum_v B^2 \sum_r \sum_{v'} B'^2 \right]^{1/2}} \quad .$$

$A(\Delta r, v)$ and $A(\Delta v)$ are sensitive to different types of intensity fluctuations. $A(\Delta v)$ compares normalized intensities in pairs of velocity channels; normalization is necessary because the large difference in intensity in line wings compared to line cores would make the unnormalized autocorrelation function difficult to interpret. The choice of a normalized brightness, B, for $A(\Delta v)$ computations, gives equal weight to line wings and line cores (Baker 1973).

c) Statistical Calculations

For optically thin line emission, as is generally the case for ^{13}CO, $C^{18}O$, and HC_3N transitions at 2.7-4mm, the intensity at each velocity is proportional to the column density (cm^{-2}) at that velocity:

$$T(v) \propto \underline{N}(v) = \int \underline{n}(v)ds,$$

where $\underline{n}(v)$ is the particle density (cm^{-3}) and s is the path length in the line of sight. Therefore the observed intensity fluctuations actually describe column density fluctuations -- as long as the molecular cloud is fairly uniform in its other properties (such as excitation temperature). In order to simplify the analysis, we shall first assume the following crude model: the molecular cloud consists of many smaller fragments, each of column density $\underline{N}_o$ giving rise to an average temperature contribution

$\langle T_o \rangle$, and the average number of fragments in the antenna beam is n. We assume a Poisson distribution for n, so that the intensity (in appropriate units) at one position, the intensity averaged over all positions, and the intensity variance are given by the following expressions:

$$T(v) = n(v) \langle T_o(v) \rangle,$$

$$\langle T(v) \rangle = \frac{\sum T(v)}{N} = \langle n(v) \rangle \langle T_o(v) \rangle,$$

$$\mathrm{VAR}\ T(v) = \frac{\sum [T(v) - \langle T(v) \rangle]^2}{(N - 1)} = \langle n(v) \rangle \langle T_o(v) \rangle^2.$$

The values of $T_o(v)$ and $\langle n(v) \rangle$ are straightforwardly calculated:

$$\langle T_o(v) \rangle = [\mathrm{VAR}\ T(v)]/\langle T(v) \rangle,$$
$$\langle n(v) \rangle = \langle T(v) \rangle^2/[\mathrm{VAR}\ T(v)].$$

If we represent the integrated intensity in a profile by $W = \int T_o(v)dv$, then analagous to the above expressions, we can solve for n_{tot}, the total average number of cloud fragments at all velocities in an antenna beam:

$$n_{tot} = \langle W \rangle^2/(\mathrm{VAR}\ W).$$

These expressions have been used previously in analyses of H I 21cm intensity fluctuations to study interstellar turbulence in atomic gas (Baker 1973; Hachenberg and Mebold 1974) and are based on the assumption that spectral profiles observed at different positions are independent measurements. However if the autocorrelation scale length is greater than the sample spacing (as will be shown to be true for most of the sources), then each profile is not independent of the others. Furthermore, in this extremely simplified hypothetical situation, $T_o(v)$, is assumed to be a constant in each molecular cloud, e.g. $\langle T_o(v)\rangle = T_o(v)$. These assumptions and their effects are considered in more detail in Appendix C.

From $\langle T_o\rangle$, the individual cloud fragment H_2 column density at velocity v, $\langle \underline{N}_o(v)\rangle$, is easily calculated (Spitzer 1978) under the assumption that the ^{13}CO line is optically thin and the $^{13}CO/H_2$ abundance ratio is 8.3×10^{-7}:

$$\langle \underline{N}_o(v)\rangle = \frac{2.89 \times 10^{20}\ T_o(v)\Delta v}{1 - \exp(-5.29/T_{ex})}.$$

Here $\underline{N}_o$ is in cm^{-2} and Δv is the velocity interval in km s^{-1}.

IV. RESULTS

The ^{13}CO autocorrelation functions, $A(\Delta r, v)$ and $A(\Delta v)$, computed from OVRO/Kitt Peak observations, are shown in Figures 1-4 and Figure 11. Since $A(\Delta r, v)$ is computed for each spectrometer channel, the figures have been arranged so that the blue wing, line core, and red wing autocorrelation functions can be easily compared. The autocorrelations computed from the coarse-resolution Columbia observations of Orion are plotted in Figure 5.

The autocorrelations for S140 and NGC 2071 show evidence of structure over scales of 1-2 pc, from maps about 9 pc in overall extent. However the Taurus dark clouds, L1529 and L1534, appear to have structure over scales of only 0.1-0.2 pc, from maps about 1.5 pc in overall extent. Because of the way the spatial autocorrelation function is defined, large intensity variations over relatively large scales will tend to swamp effects from smaller scale variations which may have lower amplitudes. Therefore we chose from within S140 and NGC 2071, four sub-regions whose total map extents were 1-2 pc, in order to investigate the possibility of smaller fragments existing within the 1-2 pc size clumps which appear to dominate the autocorrelations in Figures 1-4. Figures 7-10 show the results from these smaller sub-region maps, which were completely sampled at 1 arcmin spacing. NGC 2071BW and S140BW are centered at the parent cloud positions in Table 1, and include positions where broad CO line wings have been detected. NGC 2068 is a relatively quiescent region southeast of the NGC 2071 cloud core, and S140(3,15) is a rather average molecular region offset from the S140 cloud core. We also applied our autocorrelation analyses to L1529C, another cloud core region which is only about 0.5 pc in diameter (Figure 6). Figures 6-10 show that within the larger molecular cloud fragments inferred from Figures 1-4, there are many more smaller clumps of material.

Figure 12 displays the results of the ^{13}CO statistical calculations: $\langle n \rangle$ and $\langle \underline{N}_o \rangle$ are plotted as a function of velocity for each source. In Appendix C, we show that $\langle n \rangle$ and $\langle \underline{N}_o \rangle$ will tend to under and over-estimate, respectively, their true values due to the simplifications adopted in their calculation. $\langle \underline{N}_o \rangle$ was computed from $\langle T_o \rangle$ under the assumption of optically thin ^{13}CO line emission. The quantity ⟨n⟩ is noticeably higher in the local cloud sub-regions compared to their parent clouds, consistent with many small clumps making up each of the large fragments which dominate the results from the large-scale maps. Similarly, ensembles of these large fragments together probably comprise the even larger (~ 10 pc) structures which show up in the Columbia Orion data (Figure 5). Note that the overall Kitt Peak/OVRO maps' maximum extents are about equal to the minimum Columbia spacings, and the size of the high resolution sub-region maps are about equal to the correlation lengths deduced from the overall Kitt Peak/OVRO maps. Thus each of the three sets of data begins where the other leaves off and we see that these molecular clouds have fragmentation occurring at a variety of spatial scales.

Figure 13 shows HC_3N observations towards the five sources. As will be discussed later in this paper, HC_3N lines at 3mm originate primarily in gas of high density ($> 10^5$ cm^{-3}) and can be used as a tracer of this material. Table 4 gives the HC_3N line widths (FWHM) and the HC_3N spatial extent (FWHM) of each source.

a) Corrections to the Autocorrelations

Even a grid of random fluctuations could give rise to nonzero autocorrelation functions because of three factors: the finite spatial resolution, inherent bias of the autocorrelation statistic, and the noise level of the observations.

The autocorrelation graphs labelled "beam" in Figures 1-11 show the effects of finite antenna resolution; they represent the autocorrelation which would result from sampling, with the Columbia, Kitt Peak and OVRO antennas, a grid of intensities which fluctuate randomly in position. Similarly, the autocorrelations labelled "aos" show the velocity autocorrelation which would be measured with the AOS if the intensity fluctuations occurred randomly with velocity. The determination of limitations due to instrumental smoothing are discussed in detail in Appendix A.

For each velocity channel in each source, we have matched the portion of $A(\Delta r, v)$ between $\Delta r = 0$ and Δr of the first null to the expected shape for an ensemble of cloud fragments each of which has a Gaussian emission profile of FWHM = d. Then the effective cloud fragment size, corrected for instrumental resolution, is

$$\theta = \left[d^2 - \theta_b{}^2\right]^{1/2},$$

where θ_b is the OVRO or Kitt Peak antenna beam FWHM (about 1 arcmin). Figure 14 shows how θ varies with velocity in each source. We do not claim that these molecular clouds are necessarily composed of Gaussian clumps of size θ; the purpose of Figure 14 simply is to <u>compare</u> rough measures of fragment size at different velocities in the various sources studied. We shall discuss the actual shapes of the autocorrelation functions later in this paper.

We have computed the effective Gaussian velocity width (FWHM) corresponding to velocity autocorrelations down to $A(\Delta v) = 0.25$. These velocity widths, Δv_f, are listed in Table 3 along with Δv measured from the ^{12}CO, ^{13}CO, and $C^{18}O$ spectral lines. All these quantities have been corrected for the spectrometer resolution in the same manner as θ described above. The velocity dispersion inferred from $A(\Delta v)$ is significantly less than would be inferred from the CO line widths. We consider this observational result to be supportive of an analysis whose working hypothesis is that molecular clouds consist of smaller fragments, each of which has smaller internal velocity dispersion than the velocity dispersion of the whole cloud.

The values of the autocorrelation functions have uncertainties which are attributable to noise level in the data and to an inherent bias in the autocorrelation statistic. These effects are worked out in Appendix B. The overall noise level (1σ) in $A(\Delta r, v)$ for OVRO data is less than or equal to 0.07, and the overall noise level in $A(\Delta v)$ is ~ 0.04 or less. The Columbia data have an autocorrelation noise level of ~ 0.05 .

IV. SOURCES

The sources chosen for this study were selected to include different types of molecular clouds. The OVRO/Kitt Peak high resolution data are sensitive to spatial scales of 0.04 to 10 pc, while the Columbia data cover 4.2 to 80 pc. A brief description of each source follows.

a) L1529

Also known as TMC2, L1529 is well studied at radio, IR, and optical wavelengths (Lichten 1982b, and references therein). Although CO emission extends for several degrees around L1529, emission from molecular lines sensitive to high densities ($\underline{n} > 10^4$ cm^{-3}) originates from isolated regions several arcmin (0.1 pc) in diameter and apparently embedded in much more extensive less dense molecular gas from which CO emission is detected. Although there is little evidence for star formation, weak CO line wings covering nearly 30 km s^{-1} have been detected near some T-Tauri objects in L1529.

The overall mass of the Taurus dark cloud complex is estimated to be 9000 M_o (Baran 1982). The mass of one of the typical high density condensations in L1529 is about 1 M_o (Myers et al. 1979). Saturated ^{12}CO line intensities indicate kinetic temperatures of 10–15 K for L1529.

b) L1534

Located about 2° northeast of L1529, L1534 (TMC1) is also a rich source of molecular emission. Embedded within the molecular cloud is a 15′ X 2′(or 0.6 X 0.08 pc) dense ridge from which HC_nN (n = 3, 5, 7, 9), NH_3, and CS lines have been detected (Avery, MacLeod, and Broten 1982; Snell, Langer, and Frerking 1982; Tolle et al. 1981). Evidence for existence of a dense core surrounded by a more tenuous halo has been found in comparisons of line strengths of various HC_nN transitions (Bujarrabal et al. 1981; Avery et al. 1982).

Snell et al. (1982) claim that the L1534 high density ridge is composed of six fragments which they suggest may be proto-stellar size objects, each of mass 2-10 M_{o}. As in L1529, ^{12}CO intensities are consistent with a 10-15 K excitation temperature in L1534.

c) The Orion Molecular Cloud Complex

The Orion Molecular Cloud complex has been completely mapped in CO by Thaddeus (1982), who estimates its total mass to be several x 10^{5} M_{o}. The complex extends over more than 15^{o} (125 pc) and includes the Orion A and B clouds, NGC 2068 and 2071, and numerous Lynds dark nebulae. The CO gas kinetic temperature in Orion varies from 10 K in the optically dark clouds more than 100 K towards the Orion KL nebula; temperatures are even higher in localized regions near IR sources which are evidently a major source of heating.

d) NGC 2071 and NGC 2068

NGC 2071 is a reflection nebula in the northeast part of the Orion complex and contains numerous signposts of star-formation, including $H_{2}0$ and OH masers, near and far infrared sources, weak radio continuum emission, broad CO and H_{2} line wings, and prominent ^{12}CO self-reversed line profiles. The mass of NGC 2071 is ~ 650 M_{o} based on NH_{3} observations (Calamai, Felli, and Giardinelli 1982); the cloud model constructed by Lichten [1982a (Chapter 1)] to fit CO observations contains a mass of 450 M_{o}. A kinetic temperature of ~ 30 K has been inferred from CO intensities, but the dust temperature is 40-50 K (Sargent et al. 1981).

About 1/3° south of NGC 2071, NGC 2068 is an optically bright H II region and reflection nebula containing numerous early-type stars. Carbon recombination lines and a weak type I OH maser have been detected towards NGC 2068 (references in White and Phillips 1981). ^{13}CO observations show that the average kinetic temperature in NGC 2068 is about 40 K.

e) S255

S255 has been studied in detail by Evans, Blair, and Beckwith (1977), who estimate its mass to be 10^4 M_o. The S255 and nearby S257 nebulae contain compact HII regions which are associated with a cluster of optically reddened areas containing far and near infrared sources, OH and H_2O masers, and radio continuum sources. The kinetic temperature in S255 is ~ 40 K towards the cloud core where the CO emission peaks.

f) S140

S140 is a molecular region of enhanced CO emission which is bounded to the northeast by the dark clouds L1202 and L1204, and is bounded to the southwest by an Hα rim (Blair et al. 1978). S140 contains several infrared sources associated with compact HII regions (Beichman et al. 1979; Hackwell et al. 1982). The cloud mass is about 2300 M_o (Blair et al. 1978) with a significant fraction of this mass concentrated in a small (1′) central region of high density ($\underline{n} > 10^5$ cm^{-3}). The average kinetic gas temperature is about 35 K in S140. In the more visually obscured regions to the east and northeast, the temperature is lower, about 15 K. CO mm wavelength lines towards the (0,0) position have very broad wings with the following properties: 1) the blue wing extends to much higher velocities than does the red wing, and 2) the red and blue wings have the same spatial distribution, unlike most CO broad-winged sources (Bally and Lada 1983). The high density region where CO peaks is about 2' from the Hα rim.

V. DISCUSSION: ^{13}CO OBSERVATIONS

Since only a limited number of sources were studied, general statements about the turbulence should be made cautiously. In those sources whose individual fragments could be resolved by the telescope, it appears that these fragments are fairly numerous (Figure 12) and each have somewhat less than the overall cloud velocity dispersion. Higher spatial resolution would be helpful to determine fragment internal velocity dispersions; in our sources, it is likely that spatial variations occur over scales smaller than the telescope resolution so that intensities in <u>all</u> velocities rise and fall together from one position to the next and inter-velocity correlations cannot be well established. This effect will make $A(\Delta v)$ overestimate the true velocity correlation scale.

As a consistency check on the statistical methods of §III.b. and on the adopted model of a molecular cloud as a collection of turbulent cloud fragments, an independent measure of the total number of fragments (at all velocities) in one antenna beam was obtained by comparing $\sigma_{\langle v\rangle}$, the standard deviation of the overall mean cloud velocity, with the typical Δv_{FWHM} of a single profile. Note that $\sigma_{\langle v\rangle}$ is the standard error for the turbulent elements' velocity distribution, and decreases as the total number of turbulent elements per antenna beam increases. This estimate of

n_{tot} is:

$$n^{*}_{tot} = [\Delta v_{FWHM}]^{2}/[8(\ln 2)(\sigma_{\langle v\rangle})^{2}].$$

In Table 5 we show n_{tot} (from §III.b.) and n^{*}_{tot} for each source. The two methods are in reasonable agreement. Note that if a molecular cloud were totally dominated by radial collapse or expansion (the "large-scale velocity gradient" model), one would expect very little variation in the observed velocity centroid across the source, and therefore a very high value of n^{*}_{tot} would be derived. n^{*}_{tot} is not systematically greater or lower than n_{tot}, which was derived totally independently from intensity fluctuations. Therefore we conclude that a substantial amount of the observed velocity dispersion in molecular clouds is due to apparently random relative motions between smaller cloud fragments.

a) Randomness of the ^{13}CO Fluctuations

We first consider the randomness of the observed ^{13}CO fluctuations. This is an important consideration for determining the validity of turbulent radiative transfer cloud models. It is also relevant in comparisons of turbulent and mass motion contributions to line broadening in molecular clouds.

i) Autocorrelation of a Poisson Random Process

Let ΔT_i denote the deviation at position i from the average ^{13}CO intensity. We assume optical thinness (a fairly reasonable assumption except perhaps at the line center in some sources) so that ΔT is a measure of column density fluctuations. We shall greatly simplify the situation and say that ΔT varies a random number of times over the interval Δr to the position j of the next measurement, ΔT_j, and that ΔT assumes only values +T or −T. These fluctuations occur on the average with density λ. Let $P_n(\Delta r)$ be the probability that there are n changes from +T to −T over the interval Δr. For random fluctuations independent of processes outside the interval Δr, by definition this is a Poisson process (Bendat and Piersol 1971):

$$P_n(\Delta r) = \frac{(\lambda \Delta r)^n e^{-\lambda \Delta r}}{n!}.$$

The autocorrelation of this process is:

$$A(\Delta r) = \frac{\langle \Delta T_i \Delta T_j \rangle}{\langle \Delta T_i{}^2 \rangle} .$$

The averages are taken over all positions i, j separated by distance Δr. The numerator can be solved for as follows: the probability for a product $\Delta T_i \Delta T_j$ equalling $+T^2$ is simply $P_+ = P_0 + P_2 + P_4 + \ldots$, and the probability for $-T^2$ is $P_- = P_1 + P_3 + \ldots$ Thus we have

$$\langle \Delta T_i \Delta T_j \rangle = T^2 P_+ - T^2 P_-$$

$$= T^2 \sum (-1)^n P_n$$

$$= T^2 e^{-\lambda\Delta r} \sum \left[(-1)^n (\lambda\Delta r)^n/(n!) \right]$$

$$= T^2 e^{-2\lambda\Delta r}.$$

The denominator of $A(\Delta r)$ is T^2, so the autocorrelation is

$$A(\Delta r) = e^{-2\lambda\Delta r}.$$

This is the result for a Poisson process in which intensity fluctuations are represented as a random rectangular wave process (Bendat and Piersol 1971). A more realistic representation of the fluctuation pattern might have Gaussian rather than square-wave shapes and this could alter the detailed shape of $A(\Delta r)$; the above expression would still give the general form for a Poisson process.

Note that most of the spatial autocorrelations in Figures 1-4 and Figures 6-10 are not well approximated by a simple exponential form. Most reach zero, are negative over a range of scale lengths, and then are positive again. As a contrasting example to the Poisson process, we shall consider a periodic pattern for ^{13}CO intensity fluctuations.

ii) Autocorrelation of a Periodic Process

As a simple example of a periodic pattern for ^{13}CO intensity fluctuations, we shall assume the following representation for ΔT:

$$\Delta T_i = T \cos(2\pi X/R_o + \theta_1) \cos(2\pi Y/R_o + \theta_2),$$

where θ_1 and θ_2 are random variables with uniform density $1/2\pi$ over the range $(0,2\pi)$, T and R_o are constants denoting the peak amplitude and scale length of the fluctuations, and (X,Y) are the coordinates for position i. Then for position j offset from position i by $(\Delta X,\Delta Y)$,

$$\Delta T_j = T\cos[2\pi(X+\Delta X)/R_o + \theta_1]\cos[2\pi(Y+\Delta Y)/R_o + \theta_2].$$

The autocorrelation for this distribution is:

$$A(\Delta X,\Delta Y) = \frac{\iint \Delta T_i \Delta T_j \; d\theta_1 d\theta_2}{\iint [\Delta T_i]^2 \; d\theta_1 d\theta_2}$$

$$= \cos(2\pi\Delta X/R_o)\cos(2\pi\Delta Y/R_o).$$

If we use the convention that $\Delta X = \Delta r\cos(\alpha)$ and $\Delta Y = \Delta r\sin(\alpha)$, the above expression can be simplified to

$$A(\Delta X,\Delta Y) = \cos\left[\frac{2\pi(\Delta X+\Delta Y)}{R_o}\right] + \sin\left[\frac{2\pi\Delta X}{R_o}\right]\sin\left[\frac{2\pi\Delta Y}{R_o}\right]$$

$$= \cos\left[\frac{2\pi\Delta r\sin(\alpha+\pi/4)}{R_o\sin(\pi/4)}\right] + \sin\left[\frac{2\pi\Delta r\cos(\alpha)}{R_o}\right]\sin\left[\frac{2\pi\Delta r\sin(\alpha)}{R_o}\right].$$

We now assume that α is a uniformly distributed random variable over $(0,2\pi)$ for a given displacement of magnitude Δr. The autocorrelation function, $A(\Delta r)$, is computed by averaging over all possible values of α, e.g. all possible values of $(\Delta X,\Delta Y)$, for a given Δr:

$$A(\Delta r) = (1/2\pi) \int A(\Delta X, \Delta Y)\, d\alpha$$

$$= J_o\left[\frac{2\pi \quad \Delta r}{R_o \sin(\pi/4)} \right],$$

where J_o is the zeroth order Bessel function.

Figures 15a and 15b are graphical representations of Poisson and periodic fluctuation patterns and their corresponding autocorrelation functions. A qualitative comparison with Figures 1-10 shows that Figure 15b is similar in its general form to the observed spatial autocorrelations based on high resolution data, especially in smaller cloud sub-regions, while Figure 15a gives the general form of the coarse resolution Columbia autocorrelations and of some autocorrelations derived from the comprehensive OVRO/Kitt Peak maps, which are sensitive to larger spatial scales. These results are suggestive of various degrees of fragmentation and clumping in molecular clouds, where large-scale (~ several pc or more) fluctuations occur as a random Poisson process, but on smaller, internal scales, an average "wavelength" or fragment size can also be identified. The Poisson density parameter we deduce from Figure 5, $1/\lambda \sim 10$ pc per sub-cloud, is in agreement with the ~ 7-10 pc turbulent scale length found by Baker (1973) and Aller (1973) in the atomic and ionized interstellar medium.

We also predict that higher resolution observations of these sources will reveal structure on even smaller scales. In each source, there are large intensity variations over the minimum 1′ sample spacing. Higher resolution could be achieved with a larger antenna, with higher frequency observations, or with interferometric observations (which are currently under way at OVRO).

b) A Clumpy Turbulent Interpretation

Table 3 and Figures 1-12 are certainly consistent with a clumpy "turbulent" description of molecular clouds (Zuckerman and Evans 1974; Baker 1976). In Table 3 the ^{13}CO Δv_f for the individual turbulent elements in L1529 and L1534 correspond to 3-D rms velocities of only 0.29-0.44 km s^{-1}; the rms (3-D) thermal velocity for a 15K gas composed primarily of molecular hydrogen is 0.38 km s^{-1}. In this sense, the internal velocity dispersions of the hypothesized individual turbulent elements are not supersonic. Note also the similar magnitudes of Δv_f in Table 3 and $\Delta v(HC_3N)$ in Table 4. Presumably the HC_3N emitting elements have sizes and velocity dispersions similar to those of the ^{13}CO cells; we shall show later that the HC_3N emitting regions are considerably denser than are the ^{13}CO emitting regions. The sizes of the HC_3N sources are not very well determined (Table 4), but they are at least consistent with the sizes for the ^{13}CO turbulent cells inferred from Figures 6-10.

The internal turbulent cell rms velocities (3-D) corresponding to Δv_f in NGC 2071 and S140 are 0.66-1.18 km s^{-1} (excluding S140BW, which has an extended non-Gaussian correlation over a wide velocity range); the thermal velocity corresponding to a 40K gas of H_2 is 0.54 km s^{-1}. Although not severely supersonic, these energetic motions still must be accounted for. One possible explanation is that since these sources are so much more distant than L1529 and L1534, there may be numerous turbulent cells smaller than our 1′ instrumental resolution. If fragments the same size as were found in L1529 and L1534 are also in NGC 2071 and S140, they could not be detected unless much higher resolution (by a factor of 5-10) were used. If there are many unresolved fragments, the internal fragment velocity dispersion will be overestimated by the method used to calculate A(Δv). An extreme example would be one in which the entire cloud was only a few antenna beams in size; then intensities at <u>all</u> velocities would rise and fall together and A(Δv) would be large at all velocity lags. We expect that this question will be settled when the more distant sources are observed with the same absolute spatial resolution as the closer sources. This could explain the extended velocity correlation found in the broad line region of S140, which is the most distant source, and the only one with a source of especially intense emission only a few antenna beams in diameter. Finally, we point out that any large-scale mass motions will tend to smear out A(Δv) relative to measurements in dark, more quiescent clouds such as the Taurus nebulae.

c) Organized Mass Motions in NGC 2071 and S140

It has been suggested [Blair et al. 1978; Lichten 1982a (Chapter 1)] that some large-scale mass motions are present in NGC 2071 and S140. In Figures 3 and 4, there are striking qualitative differences between the spatial correlations at red and blue-shifted velocities. In NGC 2071 (Figure 3), the blue (lower) velocity autocorrelations are smooth and wavy; the peaks and valleys can be identified with the overall cloud radius and the sizes of smaller fragments of several pc size. However in the red (higher) velocity autocorrelations, there is a cycle which is apparently too large to fit on the graph, and considerable finer small-scale wavy structure is strongly present well above the 0.07 noise level. This finer waviness is quite absent at the blue velocities. In S140, the situation is essentially reversed; smooth, large-scale waviness is found in the red autocorrelations, and small-scale finer waviness is found at blue velocities. Note that in all the autocorrelation plots based on maps 2 pc in size or less, there is no red/blue asymmetry.

A totally random velocity field for a collection of turbulent clumps could never produce the asymmetries in Figures 3 and 4. They can be explained, however, if the central cloud regions are turbulent (at least in the sense that the numerous cloud fragments there move for the most part randomly), but the outer regions partake of organized mass motion in the form of either collapse or expansion. Such systematic radial motion gives photons from the cloud core on one side of a spectral line a greater escape probability. If the cloud is contracting, the blue-shifted photons have the lower optical depth; for expansion, the red-shifted photons have the lower opacity. All other things being equal, the velocities with the lower optical depths will tend to show more structure in the autocorrelation function, since $A(\Delta r)$ is sensitive to clumpy cloud structure only to the degree that T_A^* is proportional to column density. As τ increases, however, T_A^* begins to reflect more and more some kind of column-averaged temperature in the cloud. It is known from optically thick ^{12}CO line observations, that the projected temperature generally rises in the direction of cloud core heating sources, but that considerable fine scale structure is washed out by line saturation effects. Generally, our ^{13}CO opacities in S140 and NGC 2071 vary from 0.1 to 0.6, depending on the velocity displacement from the line center, but at isolated positions,

$\tau(^{13}CO)$ can be as high as 1 or 2 [Lichten 1982a (Chapter 1)]. If systematic radial mass motion superimposed on a turbulent cloud core is responsible for the asymmetries in Figures 3 and 4, then the direction of motion is expansion in NGC 2071 and contraction in S140. Lichten [1982a (Chapter 1)] has discussed how the ^{12}CO self-reversals towards NGC 2071 indicate that at least part of the cloud is expanding. Loren (1981) and Loren et al. (1981) have also suggested that part of NGC 2071 is expanding.

Regardless of the validity of the differential opacity explanation offered above, it is clear from Figures 3 and 4 that in those regions, some of the red and blue shifted gas in the outer parts of S140 and NGC 2071 are coming from different parts of the clouds. The outer, not inner, regions are implicated since Figures 1-2, 6-7, and 9, which are all based on smaller maps centered at cloud cores, show basically the same autocorrelation form at red and blue-shifted velocities in a given source. This is expected from cloud cores whose velocity fields are mostly random with little or no contribution from systematic radial components.

We have also examined our data for evidence of rotation. NGC 2071 has a slight NW-SE velocity gradient, although the larger northeast Orion complex in which it is embedded shows no rotation. The southern part of Orion seems to have a velocity shift in the opposite direction. S140 has no discernible overall velocity shift; L1529 and L1534 show little change in velocity over the areas mapped. Within NGC 2071 and S140, there are numerous local instances of velocity shifts which seem to prefer no particular spatial orientation. It is possible that mild rotation might be associated with expansive or contractive motions in S140 and NGC 2071.

d) Energy Sources for Supersonic Gas Motions

The origin of the universally observed supersonic CO linewidths in galactic molecular clouds has been a troublesome problem since the earliest mm-wave observations were made. In the literature, the following causes for supersonic gas motions have been suggested: gravitational collapse (Goldreich and Kwan 1974); expanding HII regions (Oort and Spitzer 1955; Bania and Lyon 1980) and supernovae explosions (McKee and Ostriker 1977); hydromagnetic waves (Arons and Max 1975); cloud impacts (Bash et al. 1981); galactic rotational shear (Fleck 1980, 1981); for dark clouds, winds from T Tauri stars (Norman and Silk 1980); and transmission of protostellar rotational energy to the molecular cloud via a rotationally driven wind (Franco 1983). We shall briefly discuss each of these possibilities in the following sections.

i) Gravitational Collapse

It has been suggested that molecular clouds are undergoing gravitational collapse (Goldreich and Kwan 1974; Loren 1976, 1977; Snell and Loren 1977). However if all clouds were collapsing, the resultant rate of star formation would be 1 to 2 orders of magnitude greater than that which is observed (Zuckerman and Evans 1974). A simple collapsing cloud line profile should become more narrow at the cloud edge while remaining centered at the cloud core velocity; however the observations of Wannier, Lichten, and Morris [1983 (Chapter 3)] show that towards cloud edges, CO line profiles become irregular, sometimes splitting apart at various velocities, and it is not unusual for the cloud velocity to be different at cloud edges than towards cloud cores. Other observational evidence is suggestive of cloud collapse which is retarded or halted at cloud cores (Lada et al. 1974; Lada 1976). In some models the cloud core is turbulent (Kwan 1978; Linke and Goldsmith 1980) and the turbulent energy could be derived from the gravitational collapse (Boland and de Jong 1982). In any case, the collapse must be stopped somewhere in the cloud since the gravitational free-fall time is (Spitzer 1978):

$$\tau_{ff} = [3\pi/(32G\rho_{H_2})]^{1/2} \sim 2X10^6 \text{ years}$$

for a molecular cloud with $n_{H_2} \sim 300$ cm^{-3}. However molecular cloud lifetime estimates range from 4X10^7 years (Bash 1979) to > 10^9 years (Scoville and Hersh 1979).

Calamai et al. (1982) argue that gravitation cannot provide the main energy input for the NGC 2071 molecular cloud because gravitational energy could replace the energy lost due to dust radiation in that source for only ~ 400 years.

In our small sample of molecular clouds, we find (§V.c.) evidence that one is possibly contracting, and one possibly expanding. Judgment on the feasibility of powering internal supersonic turbulence through molecular cloud collapse must be reserved until it can be determined to what extent molecular clouds are contracting. Since some clouds may be expanding in an overall sense (see also Loren 1981), it is not clear that internal turbulent energy is generally derived from gravitational collapse. In Chapter 5, we shall test the collapsing cloud hypothesis directly by examining velocity fluctuations.

ii) HII Regions and Supernovae

The presence of powerful HII regions associated with O and B stars must surely affect molecular cloud kinematics. However the isolated radio continuum sources which have been detected towards L1529, NGC 2071, S140, and S255 (Gilmore 1980; Calamai et al. 1982; Bally 1982; Ho et al. 1981) are relatively small and weak in comparison to the powerful HII regions associated with Orion A or W3, for example. It seems unlikely that these smaller HII regions are responsible for the turbulent velocity fields throughout the interiors of neutral molecular clouds. Furthermore, there are numerous sources such as L1534 which do not contain any detectable HII regions. Although powerful HII regions and supernovae may play an important role in the overall energy balance of the interstellar medium (Spitzer 1978; McKee and Ostriker 1977), the local molecular cloud gas motions are probably due to some other mechanism to which they can be more directly linked. The energetic input of embedded stellar objects which may be associated with weak, compact HII regions will be discussed below.

iii) Hydromagnetic Waves

Arons and Max (1975) suggested that if CO emitting clouds contain systematic magnetic fields over scales of ~ 10 pc with strengths $B_0 > 40$ μGauss, observed line widths could be caused by hydromagnetic waves. Although they postulated a major role in this process for HII regions, Arons and Max also mentioned possible hydromagnetic wave mechanisms for dark clouds without embedded HII regions. To confirm or disprove their model, the strengths of magnetic fields in a wide variety of molecular sources must be determined; at the present time, these measurements are unavailable. Wannier, Scoville, and Barvainis (1983) have interpreted their upper limits for observation of linear polarization in dense molecular clouds as evidence for considerable curvature or fine scale structure of magnetic or velocity fields over distances of 0.1–1 pc at a level of about 10μGauss.

Future work in the area of molecular cloud turbulence should place a high priority on magnetic field studies. Clark and Johnson (1982) have inferred magnetic field strengths of 30–60 μGauss by invoking magnetic braking to account for their observations of B361, but their interpretation should be viewed cautiously as model-dependent, especially in light of the lack of detection of linear polarization in a variety of nebulae.

iv) Cloud Impacts

Bash, Hausman, and Papaloizou (1981) devised a model for giant molecular clouds in which impacts with smaller clouds supply the energy to maintain internal turbulence. This model does not apply to regions with star formation, however, and is specifically directed towards clouds of size ~ 40 pc; its relevance to the sources of size 0.1–10 pc with which our study is concerned is not clear, particularly in light of recent evidence (Sargent et al. 1981) that molecular clouds previously thought to be free of star formation may have embedded protostars which can only be detected at far infrared wavelengths. In any case, all the molecular clouds in our study are associated with complexes which show some evidence for at least low mass star formation, so we will not discuss the cloud impact model further. It would be difficult to apply the cloud impact model to isolated dark clouds in which CO line widths are still found to be supersonic (Leung et al. 1982).

v) Galactic Rotational Shear

Goldreich and Lynden-Bell (1965) discussed the spiral arm structure of the Galaxy in terms of sheared gravitational instabilities resulting from differential rotation in a disk. They derived expressions relating the velocity dispersion of stars to galactic velocity distributions and proposed a theory of spiral arm formation in which differential rotation aids the growth of small sheared perturbations, with star formation and turbulence interactions playing a major role. Fleck (1980, 1981) has elaborated on this theme and suggests that the shearing action of differential galactic rotation can replenish the energy dissipated by supersonic gas motions in molecular clouds. Fleck (1981) estimates that this source of turbulent energy could stabilize molecular clouds for up to $\sim 10^{10}$ years.

In view of the results of Larson (1981) and of Leung, Kutner, and Mead (1982), who argue that molecular line widths in a variety of sources vary with size in a way similar to the Kolmogoroff rule for subsonic turbulence, the model of Fleck (1981) provides a natural origin for a common hierarchy of turbulent interstellar motions. However, the existence of wide ranges of spectral line widths for the same molecular transition at positions inside <u>the same molecular cloud</u> is then a puzzling phenomenon. For example, in the Per OB2 giant molecular cloud near NGC 1333 and HH 7-11, the FWHM $\Delta v(^{12}CO)$ is ~ 6 km s^{-1} and broad, low intensity ^{12}CO line wings cover ~ 40 km s^{-1} (Snell and Edwards 1981; Loren 1976); south of NGC 1333, the ^{12}CO line width decreases to only ~ 2 km s^{-1} but then increases to ~ 3.2 km s^{-1} near the cloud edge [Lichten unpublished data; see also Wannier, Lichten and Morris 1983 (Chapter 3), whose designation for this source region is Per OB2-B]. In the Orion molecular cloud L1630, Milman et al. (1975) report ^{13}CO line widths (FWHM) varying by a factor of 3 from adjacent regions. The considerable variation of line width with position observed in molecular clouds is suggestive of significant input from <u>local</u> line broadening mechanisms. Fleck (1981) states that "local turbulent motions...[are] unlikely...to be dominant, since the resultant velocities would be largest on the smallest scales..." Yet just the opposite is observed, since the highest velocities in molecular clouds are found in the broad wing sources which are spatially limited to localized regions of average size ~ 0.4 pc (Bally and Lada 1983).

One solution could be that the energy from galactic differential rotation is transmitted into molecular cloud interiors via mechanisms discussed by Franco (1983), who proposes that protostellar objects return mass, angular momentum, and rotational energy back to the surrounding molecular cloud material during the contraction process. Franco (1983) examines the effects of a rotationally driven stellar wind (Hartmann and MacGregor 1982) on the ambient molecular gas and finds that it is sufficient to power the observed turbulence; his model has the advantage of requiring a low space density of protostellar objects ~ 0.1 pc^{-3}. Differential galactic rotation could supply turbulent energy to molecular clouds if this were the source of rotational energy of protostellar objects, whose irregular space distribution could be responsible for internal cloud variations of molecular line widths.

Indirect evidence suggestive of a connection between large scale galactic motions and velocity dispersions within cloud interiors is shown in Figure 16. Figure 16 relies on the results in Chapter 3 (Wannier, Lichten, and Morris 1983), where high resolution CO and H I observations were compared and warm H I halos or shells enveloping molecular clouds were detected. In Chapter 3, we were able to calculate a minimum kinetic temperature of the warm H I. The one-dimensional thermal line width for atomic hydrogen at this minimum temperature is plotted against the measured ^{13}CO linewidth towards cloud centers of each source observed in Chapter 3. The correlation is suggestive of a link between supersonic molecular gas motions in cloud interiors and the temperature of surrounding warmer H I material. Clearly more sources are needed to establish a statistical basis for this relationship; additional observations towards this end are currently underway (Wannier, Morris, and Lichten 1983).

v) High-Velocity Mass Outflows from Stellar Objects

Norman and Silk (1980) proposed a model for dark molecular clouds in which ~ 0.1 pc clumps of dense ($n \sim 10^4$-10^5 cm^{-3}), cool ($T_k \sim 10$ K) material move supersonically through a warmer ($T \sim 30$ K), less dense

($n \sim 10^3$-10^4 cm^{-3}) interclump medium; high-velocity winds from low-mass pre-main-sequence objects (such as T Tauri objects) provide contiuous dynamic input into the molecular clouds and maintain the turbulence.

The predictions of Norman and Silk have been remarkably accurate for some dark cloud observations (see Lichten 1982b, and Avery 1980). The high space density (> 10 pc^{-3}) they require for T Tauri objects, however, has not been confirmed outside of certain parts of the Taurus complex. Franco's (1983) rotationally driven stellar wind model is similar to the model of Norman and Silk, but requires a lower space density of young stellar objects by two orders of magnitude to power molecular cloud turbulence. The recent detection of high-velocity molecular flows in dark clouds of low-mass star formation (Bally and Lada 1983; Edwards and Snell 1982; Kutner et al. 1982; Lichten 1982b; Frerking and Langer 1982) as well as in warmer molecular clouds with strong infrared sources shows that these energetic events are more common than was once thought. Broad CO line wings thought to be due to bipolar mass outflows from stellar objects occur over characteristic scales ~ 0.4 pc on the average (Bally and Lada 1983), which is approximately equal to the small-scale correlation lengths in Figures 6-10, and to the HC_3N source sizes in Table 4. It seems appropriate to consider the hypothesis that internal cloud turbulence may derive its energy and some of its small scale structure from these high velocity flows. Bally and Lada (1983) conclude that energetic high-velocity flows could support molecular clouds only if turbulent energy in molecular clouds has a dissipation timescale greater than one free-fall time. But Scalo and Pumphrey (1982) show that for supersonically turbulent systems composed of many fragments, the dissipation timescale is a factor of ~ 20 greater than the geometrical collision timescale due to the preponderance of oblique collisions which dissipate relatively little energy, and they estimate that the dissipation timescale is longer than the free-fall time by an order of magnitude. Therefore it appears that molecular cloud support from these energetic molecular flows should be seriously considered. Since this question will ultimately be settled by determination of the frequency of occurrence of high-velocity molecular flows, we shall only make a simple rough calculation to check on the feasibility of maintainence of turbulent motions by this source of energetic input. Consider a cloud of mass M_{cl} containing fragments moving with turbulent velocity V_t, whose correlation scale length is λ. Embedded in this cloud is a high-velocity source with typical outflow velocity V_{wing} involving mass M_{wing} having timescale τ. If the turbulent energy is derived from this energetic outflow, then

$$e \, \frac{M_{wing}(V_{wing})^2}{\tau} > \frac{1}{2} \, \frac{M_{cl}V_t^3}{\lambda\xi} ,$$

where $\xi \sim 20$ is the factor deduced by Scalo and Pumphrey (1982) and e is the efficiency of transmission of energy in the outflow to turbulence gas motions in the molecular cloud. In convenient units:

$$1000e \, \frac{M_{wing} \, [V_{wing,25}]^2}{\tau_4} > \frac{M_{cl,100} \, [V_{t,2}]^3}{\lambda_{18}} .$$

M_{wing} and $M_{cl,100}$ are in units of M_o and $100M_o$, $V_{wing,25}$ in units of 25 km s^{-1}, $V_{t,2}$ in units of 2 km s^{-1}, τ_4 in units of 10^4 years, and λ_{18} in units of 10^{18} cm. Our spatial autocorrelation results show $\lambda_{18} \sim 1$, V_{wing} and M_{wing} are estimated from observations of ^{12}CO and ^{13}CO in the high-velocity wings, and M_{cl} and V_t are estimated from the intensity and width of the ^{13}CO line core. Since $e \sim 0.1$ (Lada and Gautier 1982; Solomon, Huguenin and Scoville 1981), it appears that each high-velocity source can provide turbulent energy for $\sim 10^4$ $M_\odot$ in a typical clumpy molecular cloud, over the lifetime (10^4-10^5 years) of the outflow.

When the distribution, total number, and frequency of broad-wing sources in our Galaxy is better known, their total contribution to molecular cloud turbulence will be better understood. In light of Figure 16, one might speculate that the turbulence within molecular clouds, if powered mainly from within by energetic outflows from embedded stellar objects, could play a role in heating the H I halos which surround molecular clouds. A detailed treatment of this possibility is beyond the scope of this paper, and is probably not justified by current observations. However in the future, it could be investigated if high-velocity outflows are found to be common in all molecular clouds.

VI. Discussion: HC_3N Observations

The rotational lines of HC_3N are sensitive molecular hydrogen density probes of molecular clouds (Avery 1980; Avery et al. 1982; Vanden Bout et al. 1983). A characteristic density, $\underline{n}^*$, can be defined for each transition by equating the spontaneous emission rate, A_{ul}, with the collisional excitation rate (Evans 1980):

$$A_{ul} = \underline{n}* \langle\sigma v\rangle \left[1 - e^{-h\nu/kT} \right],$$

where $\langle\sigma v\rangle$ is the collisional rate ($cm^3 s^{-1}$) given by Green and Chapman (1978). We find $\underline{n}* \sim 2X10^3$, $5X10^5$, and $1X10^6$ cm^{-3} for the $^{13}CO(1-0)$, $HC_3N(9-8)$, and $HC_3N(11-10)$ transitions at a temperature of 20 K. Because of their high excitation requirements, we observed HC_3N lines at 3mm wavelength to find the distribution of dense (10^5-10^6 cm^{-3}) molecular gas in our sources. The interpretation of HC_3N emission in molecular clouds is fairly simple since it has been found to be optically thin for most sources which have been studied at the 9-8 and higher transitions (Morris et al. 1977; Vanden Bout et al. 1983).

Table 4 shows that in the sources in which we mapped HC_3N, the HC_3N source sizes are a few tenths of a pc or less. Although L1534 has dimensions 0.6X0.08 pc, Snell, Langer, and Frerking (1982) have shown that there are actually 6 fragments along this ridge, each of size 0.1-0.2 pc. We have compared our HC_3N and CO data and find that in L1529, HC_3N does not peak at the same position as a CO peak, but rather at the position of a local ^{12}CO minimum. ^{12}CO moderately broad line wings are found at a different position (Lichten 1982b [Chapter 2]). However in the warm clouds S140 and NGC 2071, the HC_3N emission peaks at the strongest CO position where broad wings, self-reversals (in NGC 2071; Lichten 1982a), and infrared sources are located. The HC_3N line widths in the warm, optically bright clouds (S140, NGC 2071, and S255) are considerably larger than those found in L1529, L1534, and other colder, dark clouds (Vanden Bout et al. 1983).

It is possible that the warm clouds may contain numerous dense fragments which have been influenced by large-scale mass motions. For example, cloud contraction could have concentrated most of the high density material at the cloud centers where eventually protostars and infrared sources originated. HC_3N emission falls off rapidly away from these central positions in the warm clouds. The effect of high velocity molecular gas flows on dense gas is visible in Figure 13, which shows faint HC_3N emission outside of the line core in NGC 2071 and S140(1,2). Note, however, that no HC_3N emission from the high-velocity plateaus was detected. Presumably, some dense material is accelerated in the high-velocity flows but is not detected at the highest velocities.

Figure 13e compares molecular emission towards S140(1,2) in the lines of ^{13}CO, $C^{18}O$, HC_3N (11-10), and $^{12}CO(1-0)$. There is probably some self-absorption in the ^{12}CO line core since the line peak velocities for ^{12}CO, ^{13}CO, and $C^{18}O$ are -8.6, -7.5, and -7.5 km s^{-1}, but the velocity of the dip at the ^{12}CO line core is -7.5 km s^{-1}. Since the HC_3N (11-10) transition is excited at densities $\gtrsim 10^6$ cm^{-3}, there is <u>some</u> high density gas in the moderate line wings. Consider, for example, the emission near $v \sim -14$ km s^{-1} at the (1,2) position in S140. The $^{12}CO/^{13}CO$ T_A^* ratio at $v \sim -14$ km s^{-1} is only 4.0 ($\pm$ 0.5), so we deduce that $\tau(^{13}CO) \sim 0.3$. If the 3.2 K ^{12}CO intensity at this velocity is interpreted as beam dilution of a saturated line from a 30 K gas, the dilution factor is ~ 0.11 [Plambeck et al. (1983) find a filling factor of 0.13 for this source by an independent method]. A column density can be computed under the hypothesis that the negative line wing material consists of fragments with $\Delta v \sim 1$ km s^{-1} and assuming that the $^{13}CO/H_2$ abundance ratio is $8.3X10^{-7}$:

$\underline{N}_{H_2}$(v=-14) ~ 1.0X10^{22} cm^{-2}. If the emission at -14 km s^{-1} is due to one spherical fragment, we deduce a linear size of 0.09 pc from the dilution factor and average density ~ 4X10^{5} cm^{-3}. HC_3N (11-10) emission would be expected from such dense material. However at other velocities and positions, the $^{12}CO/^{13}CO$ intensity ratio is about 20 in the line wings, indicative of lower CO opacities which could be caused by either an overall lower average density or smaller fragment size. If the temperature is lower, the density inferred would also be lower: for example, for T = 15 K, a density of 7X10^{4} cm^{-3} would result.

Figures 9, 10, and 14 show that much CO small-scale structure in S140 was unresolved by our 1′ beam. If the typical fragment size in S140 is about 0.1 pc, it is not surprising that the spatial autocorrelation functions at Δr ~ 1′ are difficult to distinguish from the beam (instrumental) autocorrelation since Δr ~ 1′ corresponds to a scale of 0.27 pc in S140. For this source, higher spatial resolution is needed to determine correlation lengths for turbulence.

In summary, the HC_3N emission is consistent with the ^{13}CO autocorrelation results which indicate that molecular cloud fragments exist with characteristic scales of ~ tenths of pc. The weak HC_3N emission detected in moderate velocity gas in NGC 2071 and S140 indicates that <u>some</u> of the CO line wing material may be quite dense ~ 10^{5}-10^{6} cm^{-3}. Although the high density gas and the CO peaks in Taurus are found in different positions, in the warm molecular clouds, the HC_3N emission falls off quickly away from the local CO peak, possibly due to effects of large scale mass motions.

VII. Conclusions

Spatial variations of ^{13}CO spectra in five molecular clouds are consistent with each cloud containing many tens of turbulent fragments of average size 0.1–0.5 pc; there are probably smaller cloud fragments undetected because of instrumental resolution limits. The relative motions of these fragments can account for highly supersonic observed CO line widths. However the internal velocity dispersion of an individual fragment, as deduced from ^{13}CO velocity autocorrelations and HC_3N line widths in the closer, better resolved sources, is considerably less than that of the whole cloud and is probably near-sonic. The smoothness of observed CO spectral profiles results from there being typically ~ 30 fragments within the volume sampled by an antenna beam. We have also found evidence for large-scale systematic contractive and expansive motions in the outer regions of two warm molecular clouds. Coarser-resolution observations sensitive to larger scale features in the Orion region show a different pattern of intensity fluctuations on a scale of ~ 10 pc, in agreement with previous 21cm studies of properties of the atomic interstellar medium.

The HC_3N high-excitation lines in warm molecular clouds may be broadened by effects of larger-scale mass motions if several fragments are contained in the antenna beam. Relative positions of CO and HC_3N peaks in warm clouds are similar, but in dark clouds are different. We have inferred that some of the material in energetic molecular cloud gas flows near young stellar objects is in very dense clumps.

High velocity mass flows from young stellar objects could power some of the supersonic relative motions of cloud fragments, but whether they account for all observed internal cloud turbulence depends on the distribution and frequency of these outflows. It is possible that the internal cloud turbulence heats the atomic hydrogen at the edge of the clouds. The transmission of galactic rotational shear energy into molecular clouds is a second possibility. Both of these mechanisms are consistent with our reported correlation of ^{13}CO line width with H I cloud edge temperature.

APPENDIX A

INSTRUMENTAL SMOOTHING AND THE AUTOCORRELATIONS

The OVRO antenna beam pattern at 110 GHz is very close to a Gaussian form with a full width at half maximum (FWHM) of 65". This was verified in September 1982 at a wavelength of 3mm by observing 3C84 with the two antennas in the interferometer mode, offsetting an antenna 0ʹ.1 at a time and recording the decreases in fringe amplitude that resulted. The first sidelobes at the CO frequency are approximately at $r = 1ʹ.5$ with a relative gain of less than 1%. The autocorrelation labeled "beam" in Figures 1-10 represents the autocorrelation resulting from the response pattern of the antenna as would be expected for sampling a grid of randomly fluctuating numbers. The antenna sidelobes have negligible effect and the "beam" autocorrelation is virtually identical to that expected for a Gaussian. The autocorrelations of molecular cloud intensity fluctuations cannot be considered real unless $A(\Delta r, v)$ is significantly different from the "beam" autocorrelation. The Kitt Peak 12m FWHM beam is nearly identical to that at OVRO, so it has essentially the same autocorrelation (R. Howard, private communication).

The second source of instrumental smoothing is the spectrometer. The design of the OVRO acousto-optic spectrometer (AOS) is described by Masson (1982). The 1024 channels are not entirely independent; adjacent pixels have slightly overlapping response patterns. The response pattern of an individual channel was determined by injecting a calibration signal from a 5 MHz comb generator across the 100 MHz total bandwidth of the AOS. This signal is effectively a delta function, and the resulting spectrum was used to calculate the response pattern of an individual channel. In Figure 11, where $A(\Delta v)$ was based on data taken with the AOS, we have indicated the autocorrelation (labelled "aos") which would result from using the AOS to measure correlations of signals which vary randomly with velocity. The AOS autocorrelation is similar to that of a Gaussian with FWHM of 200 kHz.

The NRAO filter bank spectrometer channels have sharply peaked response functions which cross at the 3db points (R. Howard, private communication) with width 100 kHz. The limit of resolution, 0.27 km s^{-1}, also shown in Figure 11.

APPENDIX B

THE EFFECTS OF NOISE AND BIAS OF THE AUTOCORRELATION STATISTIC

a) Autocorrelation Bias

The autocorrelation function is a biased statistic because it is not exactly zero even when the data are totally uncorrelated and independent. The reason for this is that in the autocorrelation sum $X_1X_2 + X_1X_3 + \ldots$ the term X_1X_3 is not independent of X_1X_2, etc. The magnitude of this effect has been worked out exactly for the problem of serial correlation, which is a one-dimensional version of the autocorrelation discussed here. For serial correlation computed from N measurements, the autocorrelation coefficient and its standard deviation for unit lag of independent terms is (Dixon 1944)

$$A = -1/(N-1),$$

$$\sigma = \frac{1}{(N-1)}\left[\frac{N(N-3)}{(N+1)}\right]^{1/2} \sim [1/N]^{1/2}$$

For other than unit lag, this expression is still a good approximation for the exact result (Anderson 1942; Dixon 1944). To compare the two-dimensional bias to the serial correlation bias, we computed an autocorrelation for random noise using observational data at off-source velocities where there was no ^{13}CO signal. The result for $N = 110$ was $A = -0.0095$ and $\sigma = 0.05$, close to the values predicted by the serial correlation formulae. Clearly this value of A for random noise input is too small to be important; however the dispersion, σ, is significant because it indicates the uncertainty in $A(\Delta r, v)$ which results from the finite sample size.

The standard deviation of $A(\Delta v)$ is given exactly by the serial correlation formula because $A(\Delta v)$ actually is a serial calculation. The number of measurements ranged from ~ 350 for narrow lines to > 1000 for broad lines, since each channel at each position is considered a measurement (we have taken into account here the fact that adjacent channels in the spectrometer are not totally independent). The uncertainty in $A(\Delta v)$ due to the finite sample size is ~ 0.05 (narrow lines) to ~ 0.03 (broad lines).

b) Noise

The OVRO ^{13}CO noise level was 0.04–0.10 K; at Kitt Peak and Columbia, the ^{13}CO noise level was about 0.2 K. The weaker sources, L1529 and L1534, were observed for a longer time so they had somewhat lower noise levels than the stronger sources. The noise level in the spectra limits the amount of meaningful information in the autocorrelation function. Consider the following autocorrelation:

$$A\ (\Delta r, v) = \frac{\langle X_i X_j \rangle}{\left[\langle X_i^2 \rangle \langle X_j^2 \rangle \right]^{1/2}} \quad .$$

Let the noise level in each of the N profiles be $\sigma_i = \sigma_j = \sigma$, and denote the overall average intensity by $\langle X \rangle$. There will be a total of $N(N - 1)/2$ pairs of measured intensities (at a given velocity v) used to calculate the autocorrelations. In most cases, there were about 200 pairs summed for each value of Δr. Then

$$(\sigma_A/A)^2 = (4/200)(\sigma/\langle X \rangle)^2,$$

where σ_A is the standard deviation uncertainty in the autocorrelation, A. In order to keep this contribution to autocorrelation noise below 0.05, a signal/noise ratio, $A/\sigma_A = 20$ is required, since the maximum autocorrelation is unity. In this example, the signal/noise ratio should be ~ 3 or better in each profile over the range of velocities included. This limits the velocity range over which $A(\Delta r, v)$ can be computed because the signal/noise ratio is lowest in the line wings. The data in Figures 1-4, 6-10 do not include any observations which would result in an observational noise contribution of more than 0.05 to the autocorrelation function, $A(\Delta r, v)$. We estimate that the <u>overall</u> noise level (1σ) in $A(\Delta r, v)$ is less than or equal to 0.07, including effects of the autocorrelation statistic bias and noise in the ^{13}CO spectra.

The noise level in $A(\Delta v)$ can be estimated in a similar manner. The number of pairs participating in the summation, however, is much larger than for the the spatial autocorrelations, so the observational noise contribution is considerably lower, 0.02 or less. The overall uncertainty in $A(\Delta v)$ from all effects is ~ 0.04 or less.

APPENDIX C

a) INDEPENDENCE OF PROFILES

Since $A(\Delta r, v)$ is significantly non-zero for at least several values of Δr in all five sources, the set of spectral profiles for each source are not entirely independent measurements. The number of independent observations, N_I, is given by an expression of the form (Mebold et al. 1974):

$$N_I = N/\left[1 + (2/N)\sum N(\Delta r)A(\Delta r)\right],$$

where N is the number of positions observed, $N(\Delta r)$ is the number of pairs separated by Δr which were used in the calculation of the autocorrelation function, $A(\Delta r)$. In this expression we have disregarded the velocity dependence of the autocorrelation, and the summation in the denominator proceeds over all values of Δr. Noting that $\sum N(\Delta r) = N(N-1)/2$, we let

$$\rho = \frac{\sum N(\Delta r)A(\Delta r)}{\sum N(\Delta r)},$$

and it follows that

$$N_I = N/[1 + (N-1)\rho].$$

Hence the equivalent number of degrees of freedom for an unbiased estimate of the variance is

$$N_I - 1 = (N-1)(1-\rho)/[1+(N-1)\rho].$$

This expression is derived by Walsh (1947) in an analysis of variance for correlated data samples.

The five molecular clouds studied have sizable negative as well as positive autocorrelations at various spatial scales, and these tend to cancel in the calculation of ρ. In these sources, $\rho \leq 0.03$ at all velocities; typically, $N_I \sim N/2$.

A more cautious treatment would not include negative autocorrelations to calculate ρ. In that case, the number of "independent" measurements is only 0.2–0.3 the total number of positions observed. We have recomputed VAR T(v) for the sources using this smaller sample of "uncorrelated" profiles; such a procedure is equivalent to using only profiles separated by the scale length determined by the autocorrelation function up to its first null and ignoring the negative values of $A(\Delta r)$. VAR T(v) computed by this method was at most 20% larger than VAR T(v) computed by including <u>all</u> the profiles, and in most cases the difference was less than 10%.

We conclude that although the non-zero autocorrelations change the equivalent number of degrees of freedom, VAR T(v) and quantities derived from it are not affected significantly by the existence of spatial correlations in our sample.

b) VARIANCE OF CLOUD FRAGMENT PARAMETERS

The simple statistical model of §III.b. includes the assumption that at each position,

$$T(v) = n(v)\langle T_o(v)\rangle,$$

where $T_o(v) = \langle T_o(v)\rangle$ is the average contribution, taken to be a constant, from a single cloud fragment (of which there are n). We shall now assume as before that n is Poisson distributed, but we shall allow $T_o(v)$ to be a variable which could be different at different positions:

$$\text{VAR } T(v) = \langle n(v)\rangle \langle T_o(v)\rangle^2 + \langle n(v)\rangle \text{ VAR } T_o(v),$$
$$\langle T(v)\rangle = \langle n(v)\rangle \langle T_o(v)\rangle,$$

where we have substituted $\text{VAR } T_o(v) = \langle n(v)\rangle^{-1}\text{VAR } \langle T_o(v)\rangle$. The following expressions are now straightforwardly derived:

$$\langle n(v)\rangle = \frac{\langle T(v)\rangle^2}{\text{VAR } T(v)} \left[1 + \frac{\text{VAR } T_o(v)}{\langle T_o(v)\rangle^2} \right],$$

$$\langle To(v)\rangle = \frac{\text{VAR } T(v)}{\langle T(v)\rangle} \left[1 + \frac{\text{VAR } T_o(v)}{\langle T_o(v)\rangle^2} \right]^{-1}.$$

These same expressions appear in §III.b. without the quantities in brackets. For example, if $\text{VAR } T_o \sim T_o$, then as calculated in §III.b. and Figure 12, $\langle n\rangle$ and $\langle \underline{N}_o\rangle$ would underestimate and overestimate their true values by a factor of ~ 2 since they were computed assuming $\text{VAR } T_o = 0$. These are not major effects and do not significantly affect the conclusions of this paper.

TABLE 1

SOURCE LIST

Source	α(1950)	δ(1950)	D[a] (pc)	VLSR (km s^{-1})	...^{13}CO.... N_{pos}	Map (pc)[b]	Other Molecules
L1529	$04^h29^m43^s.4$	24°16'54"	140[c]	6	109	1.6	^{12}CO, HC_3N
L1534	04 38 39.0	25 35 00	140[c]	6	80	1.0	^{12}CO
Orion	05 40 00.0	-02 00 00	450	9	170	80.0	
NGC 2068	05 44 10.5	00 01 45	450[d]	10	60	2.0	
NGC 2071	05 44 30.3	00 20 18	450[d]	9	156	10.0	$C^{18}O$, ^{12}CO, HC_3N
S255	06 10 01.0	18 00 00	2500[e]	7			^{12}CO, HC_3N
S140	22 17 42.0	63 05 45	910[f]	-7	110	8.5	$C^{18}O$, ^{12}CO, HC_3N

Notes

[a] Distance to the source.

[b] Length of approximately square ^{13}CO map centered at reference position.

[c] Elias (1978).

[d] Assumed distance to Orion molecular cloud.

[e] Evans et al. (1977).

[f] Blair et al. (1978).

TABLE 2

OBSERVING PARAMETERS

Transition	Frequency (MHz)	Antenna[a]	Beam[b] (″)	T_{rec}[c] (K)	η_b[d]	Filter (km s^{-1})
^{12}CO J=1-0	115271.201	OVRO	62	700	0.75	0.26
^{13}CO J=1-0	110201.368	OVRO	65	380	0.75	0.27
^{13}CO J=1-0	110201.368	12NRAO	60	400	0.80	0.27
^{13}CO J=1-0	110201.368	COL	480	400	0.80	0.68
$C^{18}O$ J=1-0	109782.180	OVRO	65	700	0.75	0.27
HC_3N J=11-10	100466.106	11NRAO	70	420	0.60	0.09,0.30,0.75
HC_3N J=9-8	81881.458	11NRAO	85	400	0.60	0.11,0.37,0.91

Notes

[a] OVRO -- Owens Valley Radio Observatory 10.4m antenna.

11NRAO -- National Radio Astronomy Observatory 11m antenna at Kitt Peak.

12NRAO -- National Radio Astronomy Observatory 12m antenna at Kitt Peak.

COL -- Columbia University 4 ft antenna.

[b] Antenna beam full width at half maximum (FWHM).

[c] Single sideband receiver noise temperature.

[d] Beam efficiency used to calculate T_A^*. η_b is an estimate for beam to source coupling efficiency based on knowledge of source size and beam pattern.

TABLE 3

CO VELOCITY DISPERSIONS

	.... Observed Line Widths[a]........			^{13}CO A(Δv) Results
	$\Delta V(^{12}CO)$	$\Delta V(^{13}CO)$	$\Delta V(C^{18}O)$	ΔV_f
L1529	3.6	1.4	...	0.5
L1529C		1.4	0.6[b]	0.4
L1534	2.9	1.4	...	0.6
NGC 2068	...	1.9	...	0.9
NGC 2071	...	2.3	1.9	1.3
NGC 2071BW	5.0[c]	2.9	1.9	1.6
S255	4.0	2.6	...	...
S140	...	2.4	...	1.2
S140BW	6.3	3.3	2.5	extended
S140(3,15)	...	2.3	...	1.0

All ΔV are in km s^{-1} and are corrected for instrumental broadening.

Notes

[a] Line width $\Delta V = \int T_A^*(v)dv/T_A^*(\mathrm{peak})$ and equals $1.06\Delta V_{FWHM}$ for a Gaussian profile. Values are average ΔV over the region.

[b] Myers et al. (1980)

[c] Prominently self-reversed profiles make determination of FWHM uncertain.

TABLE 4

HC_3N OBSERVATIONS

	Corrected ΔV (km s^{-1})		FWHM Source Size (pc)	
	J=9-8	J=11-10	J=9-8	J=11-10
L1529[a]	0.37	0.19	0.08	....
L1534	0.44[b]	....	0.6 X 0.08[c]	....
NGC 2071	1.5	1.5	$\leq$ 0.14	$\leq$ 0.14
S140	2.1	2.1	0.4	0.4
S255	2.2	2.1	....	....

Notes

[a] At (0,2) position where HC_3N emission peaks.

[b] Vanden Bout et al. (1983).

[c] Avery et al. (1982)

TABLE 5

CLOUD FRAGMENTS PER ARCMIN ANTENNA BEAM

		n_{tot}	n^*_{tot}
L1529C	(0.5 pc core)	72	80
L1529	(all)	26	12
L1534	(1.0 pc size)	30	16
NGC 2068	(2.0 pc size)	31	34
NGC 2071BW	(1.5 pc core)	28	30
NGC 2071	(all)	8	6
S140BW	(2.0 pc core)	10	14
S140(3,15)	(1.9 pc size)	40	12
S140	(all)	6	3

REFERENCES

Aller, L.H. 1951, Ap.J., 113, 120.

Anderson, R.L. 1942, Annals of Math.Stat., 13, 1.

Arons, J., and Max, C.E. 1975, Ap.J.(Letters), 196, L77.

Avery, L.W. 1980, in IAU Symposium 87, Interstellar Molecules, ed. B.H. Andrew (Dordrecht: Reidel), p. 47.

Avery, L.W., MacLeod, J.M., and Broton, N.W. 1982, Ap.J., 254, 116.

Baker, P.L. 1973, Astr.Ap., 23, 81.

Baker, P.L. 1976, Astr.Ap., 50, 327.

Bally, J. 1982, Ap.J., 261, 558.

Bally, J., and Lada, C.J. 1983, Ap.J., 265, 824.

Bania, T.M., and Lyon, J.G. 1980, Ap.J., 239, 173.

Baran, G.P. 1982, unpublished Ph.D. thesis, Columbia University.

Bash, F.N. 1979, Ap.J., 233, 524.

Bash, F., Hausman, M., and Papaloizou, J. 1981, Ap.J., 245, 92.

Beichman, C.A., Becklin, E.E., and Wynn-Williams, C.G. 1979, Ap.J.(Letters), 232, L47.

Bendat, J.S., and Piersol, A.G. 1971, Random Data: Analysis and Measurement Procedures (Wiley-Interscience: N.Y.).

Blair, G.N., Evans, N.J., Vanden Bout, P.A., and Peters, W.L. 1978, Ap.J., 219, 896.

Boland, W., and de Jong, T. 1982, Ap.J., 261, 110.

Bujarrabal, V., Guelin, M., Morris, M., and Thaddeus, P. 1981, Astr.Ap., 99, 239.

Calamai, G., Felli, M., and Giardinelli, S. 1982, Astr.Ap., 109, 123.

Chandrasekhar, S. 1949, *Ap.J.*, 110, 329.

Clark , F.O., and Johnson, D.R. 1982, *Ap.J.*, 263, 160.

Dixon, W.J. 1944, *Annals of Math. Stat.*, 15, 119.

Edwards, S., and Snell, R.L. 1982, *Ap.J.*, 261, 151.

Elias, J.H. 1978, *Ap.J.*, 224, 857.

Evans, N.J. 1980, in *Interstellar Molecules*, ed. Andrews (Dordrecht: Reidel), 1.

Evans, N.J., Blair, G.N., and Beckwith, S. 1977, *Ap.J.*, 217, 448.

Fleck, R. 1980, *Ap.J.*, 242, 1019.

Fleck, R. 1981, *Ap.J.(Letters)*, 246, L151.

Franco, J. 1983, *Ap.J.*, 264, 508.

Frenkiel, F.N., and Schwarzschild, M. 1955, *Ap.J.*, 121, 216.

Frerking, M.A., and Langer, W.D. 1982, *Ap.J.*, 256, 523.

Gilmore, W. 1980, *A.J.*, 85, 894.

Goldreich, P., and Kwan, J. 1974, *Ap.J.*, 189, 441.

Goldreich, P., and Lynden-Bell, D. 1965, *M.N.R.A.S.*, 130, 125.

Green, S., and Chapman, S. 1978, *Ap.J.(Suppl.)*, 37, 169.

Hachenberg, O., and Mebold, U. 1974, in *Stars and the Milky Way System*, ed. L.N. Mavridis (N.Y.: Springer-Verlag), p. 120.

Hackwell, J.A., Grasdalen, G.L., and Gehrz, R.D. 1982, *Ap.J.*, 252, 250.

Hartmann, L., and MacGregor, K.B. 1982, *Ap.J.*, 259, 180.

Ho, P.T.P., Martin, R.N., and Barrett, A.H. 1981, *Ap.J.*, 246, 761.

Hunter, J.H. 1979, *Ap.J.*, 233, 946.

Hunter, J.H., and Fleck, R.C. 1982, *Ap.J.*, 256, 505.

Kaplan, S.A. 1966, *Interstellar Gas Dynamics* (Oxford: Pergamon).

Knobloch, E., and Rosner, R. 1981, *Ap.J.*, 247, 300.

Kutner, M.L., Leung, C.M. Machnik, D.E., and Mead, K.N. 1982, *Ap~~.~~J~~.~~(Letters)*, 259, L35.

Kwan, J. 1978, *Ap.J~~.,~~* 223, 147.

Lada, C.J. 1976, *Ap.J~~.~~Suppl~~.,~~* 32, 603.

Lada, C.J., and Gautier, T.N. 1982, *Ap.J~~.~~*, 261, 161.

Lada, C.J., Gottlieb, C.A., Litvak, M.M., and Lilley, A.E. 1974, *Ap.J~~.,~~* 194, 609.

Larson, R.B. 1981, *M.N~~.~~R~~.~~A~~.~~S~~.~~*, 194, 809.

Leung, C.M., Kutner, M.L., and Mead, K.N. 1982, *Ap.J~~.~~*, 262, 583.

Lichten, S.M. 1982a, *Ap.J~~.~~*, 253, 593.

Lichten, S.M. 1982b, *Ap.J~~.~~(Letters)*, 255, L119.

Linke, R.A., and Goldsmith, P.F. 1980, *Ap.J~~.,~~* 235, 437.

Loren, R.B. 1976, *Ap.J~~.~~*, 209, 466.

Loren, R.B. 1977, *Ap.J~~.~~*, 215, 129.

Loren, R.B. 1981, *Ap.J~~.,~~* 249, 550.

Loren, R.B., Plambeck, R.L., Davis, J.H., and Snell, R.L. 1981, *Ap.J~~.,~~* 245, 495.

Maddelena, R., Morris, M., and Thaddeus, P. 1983 (in preparation).

Masson, C.R. 1982, *Astr~~.~~Ap.*, 114, 270.

McKee, C.F., and Ostriker, J.P. 1977, *Ap.J~~.~~*, 218, 148.

Mebold, U., Hachenberg, O., and Laury-Micoulaud, C.A. 1974, *Astr~~.~~Ap.*, 30, 329.

Milman, A.S., Knapp, G.R., Kerr, F.J., and Knapp, S.L. 1975, *A.J~~.~~*, 80, 93.

Morris, M., Snell, R.L., and Vanden Bout, P. 1977, *Ap.J~~.,~~* 216, 738.

Munch, G. 1958, *Rev~~.~~Mod~~.~~Phys.~~,~~* 30, 1035.

Myers, P.C., Ho, P.T.P., and Benson, P.J. 1979, *Ap.J~~.~~(Letters)*, 233, L141.

Myers, P.C., Buxton, R.B., and Ho, P.T.P. 1980, in *Interstellar Molecules*, ed. Andrews (Dordrecht: Reidel).

Norman, C., and Silk, J. 1980, *Ap.J.*, 238, 158.

Oort, J.H., and Spitzer, L. 1955, *Ap.J.*, 121, 6.

Penzias, A.A. 1975, in *Atomic and Molecular Physics and the Interstellar Matter*, ed. R. Balian, P. Encrenaz, and J. Lequeux (Amsterdam: North-Holland Publishing Co.), p. 373.

Plambeck, R.L., Snell, R.L., and Loren, R.B. 1983, *Ap.J.*, 266, 321.

Sargent, A.I., Van Duinen, R.J., Fridlund, C.V.M., Nordh, H.L., and Aalders, J.W.G. 1981, *Ap.J.*, 249, 607.

Scalo, J.M., Pumphrey, W.A. 1982, *Ap.J.(Letters)*, 258, L29.

Scoville, N.Z., and Hersh, K. 1979, *Ap.J.*, 229, 578.

Serkowski, K. 1958, *Acta Astronomica*, 8, 135.

Snell, R.L., and Edwards, S. 1981, *Ap.J.*, 251, 103.

Snell, R.L., Langer, W.D., and Frerking, M.A. 1982, *Ap.J.*, 255, 149.

Snell, R.L., and Loren, R.B. 1977, *Ap.J.*, 211, 122.

Solomon, P.M., Huguenin, G.R., and Scoville, N.Z. 1981, *Ap.J.(Letters)*, 245, L19.

Spitzer, L. 1978, *Physical Processes in the Interstellar Medium* (N.Y.: John Wiley and Sons).

Stuart, F.E., and Rush, J.H. 1954, *Ap.J.*, 120, 245.

Thaddeus, P. 1982, in *Symposium on the Orion Nebula to Honor Henry Draper*, ed. A.E. Glassgold, P.J. Huggins, and E.L. Schucking (N.Y.: N.Y. Academy of Sciences).

Tolle, F., Ungerechts, H., Walmsley, C.M., Winnewisser, G., and Churchwell, E. 1981, *Astr.Ap.*, 95, 143.

Tucker, K.D., Kutner, M.L., and Thaddeus, P. 1973, Ap.J~~.~~ ~~(Letters)~~, 186, L13.

Vanden Bout, P.A., Loren, R.B., Snell, R.L., and Wootten, A. 1983, Ap.J~~.~~ (in press).

Walsh, J.E. 1947, Anna~~ls~~ ~~of~~ Ma~~th.~~ ~~Stat.~~, 18, 88.

Wannier, P.G., Lichten, S.M., and Morris, M. 1983, Ap.J~~.,~~ 268, 727.

Wannier, P.G., Morris, M., and Lichten, S.M. 1983 (in preparation).

Wannier, P.G., Scoville, N.Z., and Barvainis, R. 1983, Ap.J~~.,~~ 267, 126.

White, G.J., and Phillips, J.P. 1981, M.~~N.R.A.S.~~, 194, 947.

White, R.E. 1977, Ap.J~~.,~~ 211, 744.

Zuckerman, B., and Evans, N. 1974, Ap.J~~.~~ ~~(Letters)~~, 192, L149.

FIGURE CAPTIONS

Figure 1.-Spatial autocorrelation functions of ^{13}CO intensity fluctuations for L1529 are plotted as a function of velocity. In Figures 1-10, graphs labelled "beam" show expected result for totally uncorrelated data, illustrating the minimum autocorrelation which results solely from the slight overlap of antenna beam response patterns at the closest spacings. Scale in pc is also given by the "beam" graph.

Figure 2.-Spatial autocorrelation functions for L1534.

Figure 3.-Spatial autocorrelation functions for NGC 2071. Note the qualitatively different form for velocities less than 10 km s^{-1} as compared to velocities greater than 10 km s^{-1}. The blue (lower) velocity autocorrelations are smooth and wavy, and maxima and minima can be identified with the overall cloud radius or with the smaller fragments of 1-3 pc size. The cycle in the red (higher) velocity autocorrelations is apparently too large to fit on the graph, and considerable finer small-scale waviness are prominently visible. The different autocorrelation patterns for red and blue velocities may be indicative of organized large-scale radial motions which give photons from the turbulent cloud core a greater escape probability on one side of the spectral line than on the other. If this interpretation is correct, then the outer layers of NGC 2071 would be expanding away from the cloud core.

Figure 4.-Spatial autocorrelation functions for S140. As with NGC 2071, the red and blue sides of the ^{13}CO line show different forms for autocorrelations. However in S140, the indicated large-scale radial motion is collapse of the outer layers, opposite that in NGC 2071.

Figure 5.-Spatial autocorrelation functions for the Orion molecular cloud complex. These results are based on the Columbia 30′ resolution data, and therefore show large-scale cloud structure. All other autocorrelation functions shown here are based on 1′ minimum resolution maps from OVRO or Kitt Peak.

Figure 6.-Spatial autocorrelation functions for L1529C, the core region of L1529. Because the total map size affects the shape of the autocorrelation functions, the data in Figures 6-10 show smaller scale structure than do the autocorrelations in Figures 1-4. Note that many autocorrelations in Figures 6-10 are similar to the "beam" autocorrelations, which is indicative of cloud fragments which were unresolved by the 1′ beam.

Figure 7.-Spatial autocorrelation functions for NGC 2071BW, the core region of NGC 2071, including the broad line wing region.

Figure 8.-Spatial autocorrelation functions for NGC 2068, a relatively small region south of NGC 2071.

Figure 9.-Spatial autocorrelation functions for S140BW, the core region of S140, including the broad line wing region.

Figure 10.-Spatial autocorrelation functions for S140(3,15), a part of the northern S140 molecular cloud.

Figure 11.-Velocity autocorrelation functions for S140, NGC 2071, NGC 2068, and the Taurus nebulae. The NRAO filter width (0.27 km s^{-1}) is shown where the autocorrelations were computed from data taken with the Kitt Peak telescope; otherwise, the OVRO acousto-optic spectrometer ("aos") response is plotted. The equivalent Gaussian FWHM inferred from these autocorrelations is considerably less than the observed FWHM of the ^{13}CO lines in all cases except S140BW. This result supports our interpretation that molecular line widths are broad due to supersonic relative clump motions, while the internal velocity dispersions of the individual fragments are considerably less.

Figure 12.-Number of cloud fragments [n(v)] and H_2 column density per fragment [<u>N(v)</u>] are plotted as a function of velocity for (a) Taurus nebulae, (b) NGC 2071 and NGC 2068, and (c) S140. Note that the column density at a given velocity can be added to the column density at other velocities to give a total column density. However values of n(v) will have some redundancy with adjacent velocity channels if the internal velocity dispersion for the individual fragments is greater than the 0.27 km s^{-1} channel spacing. The maps of NGC 2071 and S140 cover about 10 pc each and seem to have about ten large fragments per antenna beam. The smaller maps [L1529, L1529C, L1534, NGC 2071BW, NGC 2068, S140BW, S140(3,15)] are 0.5-2 pc in extent and reveal considerably more fine structure, with typically 20-80 smaller clumps per antenna beam.

Figure 13.-Sample HC_3N spectra observed towards (a) L1529(0,2), (b) S255, (c) S140, and (d) NGC 2071. A comparison between HC_3N and CO spectra is made in (d) for NGC 2071 and in (e) for S140, where CO broad line wings are visible. Arrow in (e) shows emission at v = -14 km s^{-1}.

Figure 14.-Effective size, Θ, of hypothetical cloud fragments as deduced from spatial autocorrelations in Figures 1-10. The larger maps (NGC 2071 and S140) are dominated by intensity fluctuations whose correlation lengths are about 1-2 pc. The autocorrelations of the smaller regions [L1529, L1529C, L1534, NGC 2071BW, NGC2068, S140BW, and S140(3,15)], whose diameters are about 0.5-2 pc, show evidence for additional fragmentation on size scales of less than 0.5 pc. Θ has been corrected for instrumental resolution; Θ = 0 indicates that the structure is unresolved by the antenna beam. In the Taurus nebulae, NGC 2071 and 2068, and S140 the antenna main beam FWHM is 0.04 pc, 0.14 pc, and 0.27 pc.

Figure 15.-(a) Theoretical form for spatial autocorrelation function calculated for a Poisson distribution of cloud fragment sizes and separations. (b) Form for spatial autocorrelation function calculated for a periodic pattern with random phases. The Poisson distribution gives rise to an exponential autocorrelation, while the periodic distribution gives rises to a Bessel function.

Figure 16.-Thermal H I line width computed from the minimum cloud edge temperature is plotted against the observed ^{13}CO line width towards the molecular cloud core. Sources are from the sample of Wannier, Lichten, and Morris 1983 (Chapter 3). The expected H I thermal line

width appears to be correlated with the observed molecular line width, indicative of a connection between the cloud edge temperatures and internal molecular gas motions.

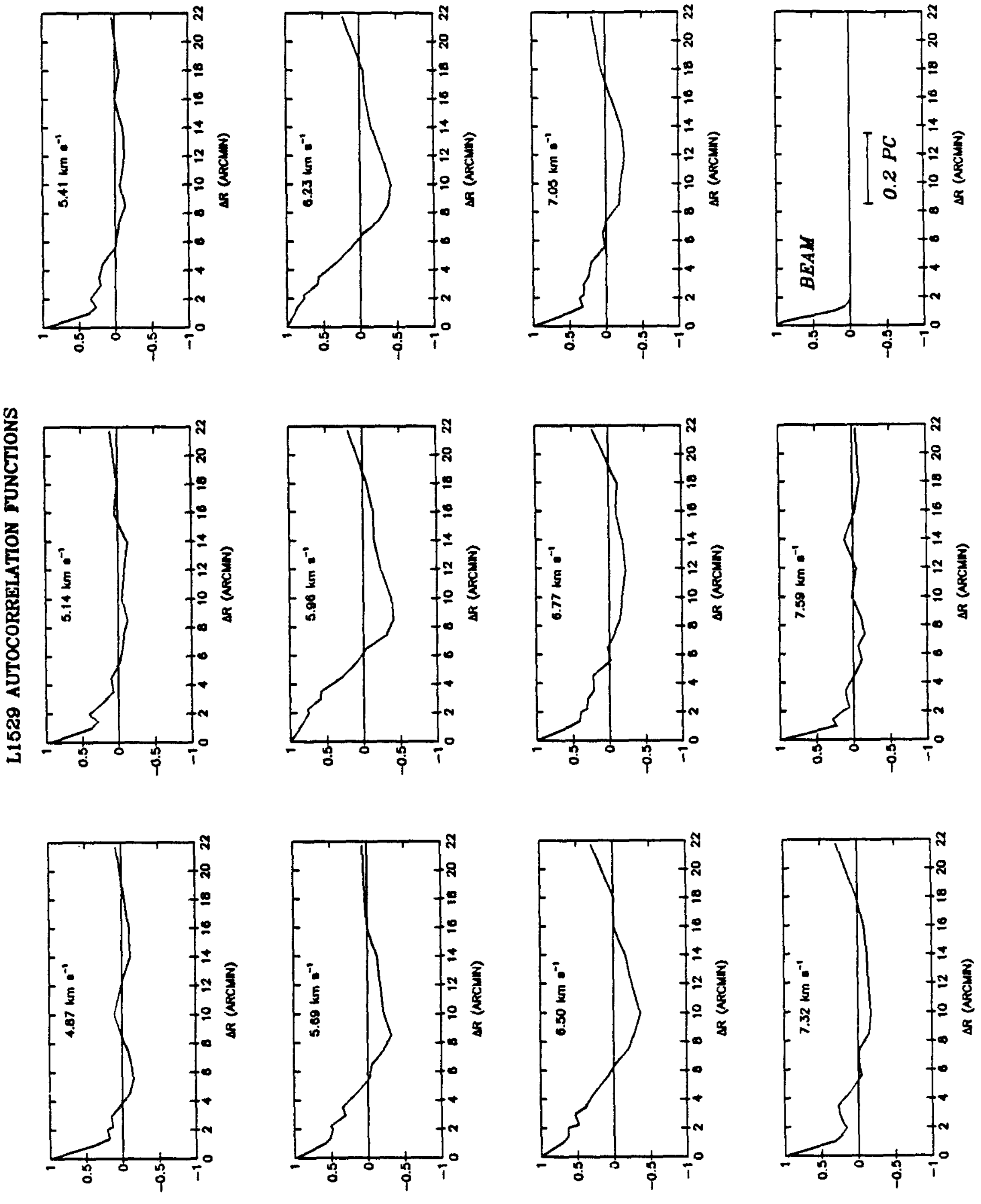
L1529 AUTOCORRELATION FUNCTIONS
4.87 km s^{-1}
5.14 km s^{-1}
5.41 km s^{-1}
5.69 km s^{-1}
5.96 km s^{-1}
6.23 km s^{-1}
6.50 km s^{-1}
6.77 km s^{-1}
7.05 km s^{-1}
7.32 km s^{-1}
7.59 km s^{-1}
BEAM
0.2 PC
ΔR (ARCMIN)
0 2 4 6 8 10 12 14 16 18 20 22
1
0.5
0
-0.5
-1

Figure 1

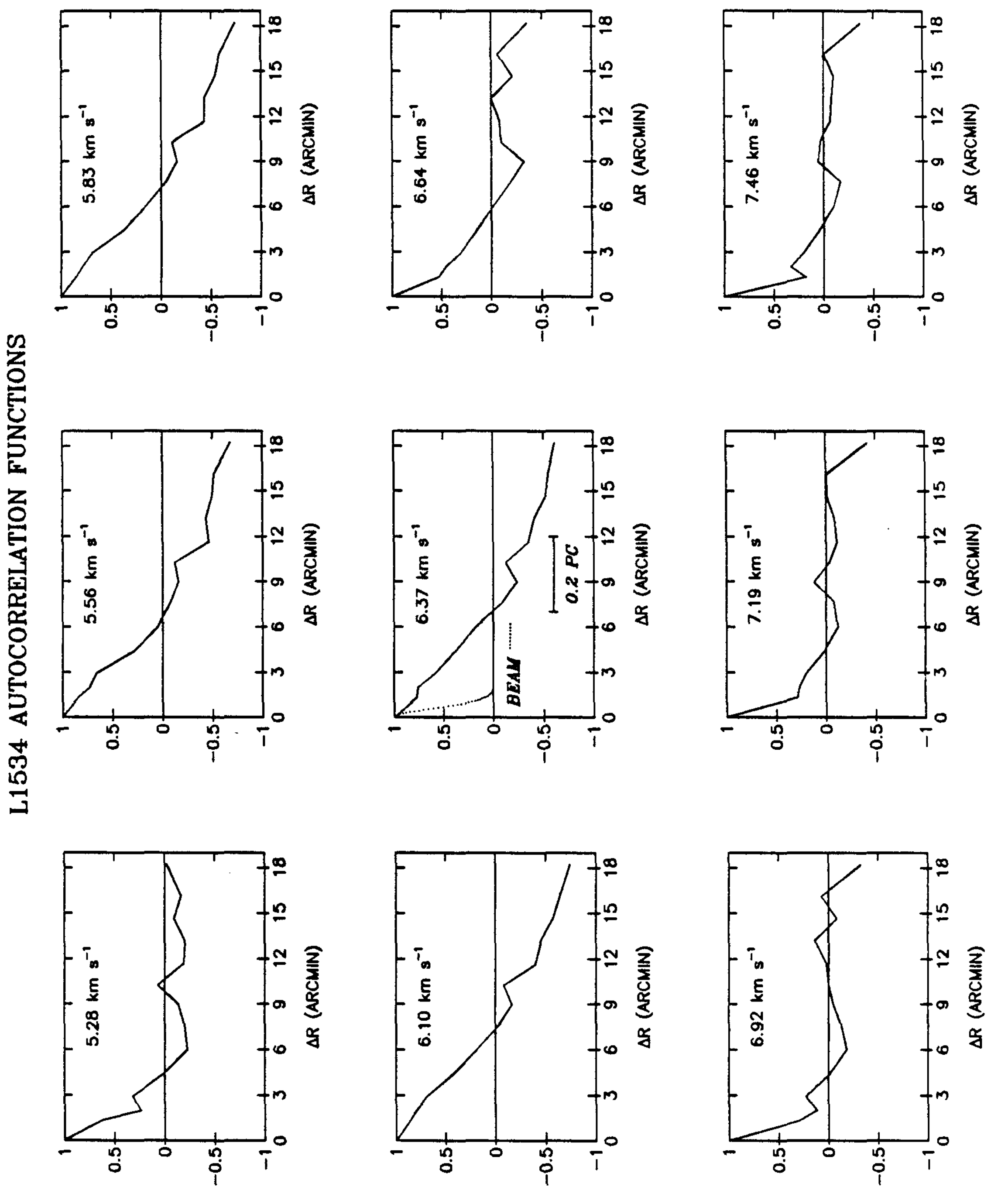
L1534 AUTOCORRELATION FUNCTIONS

Figure 2

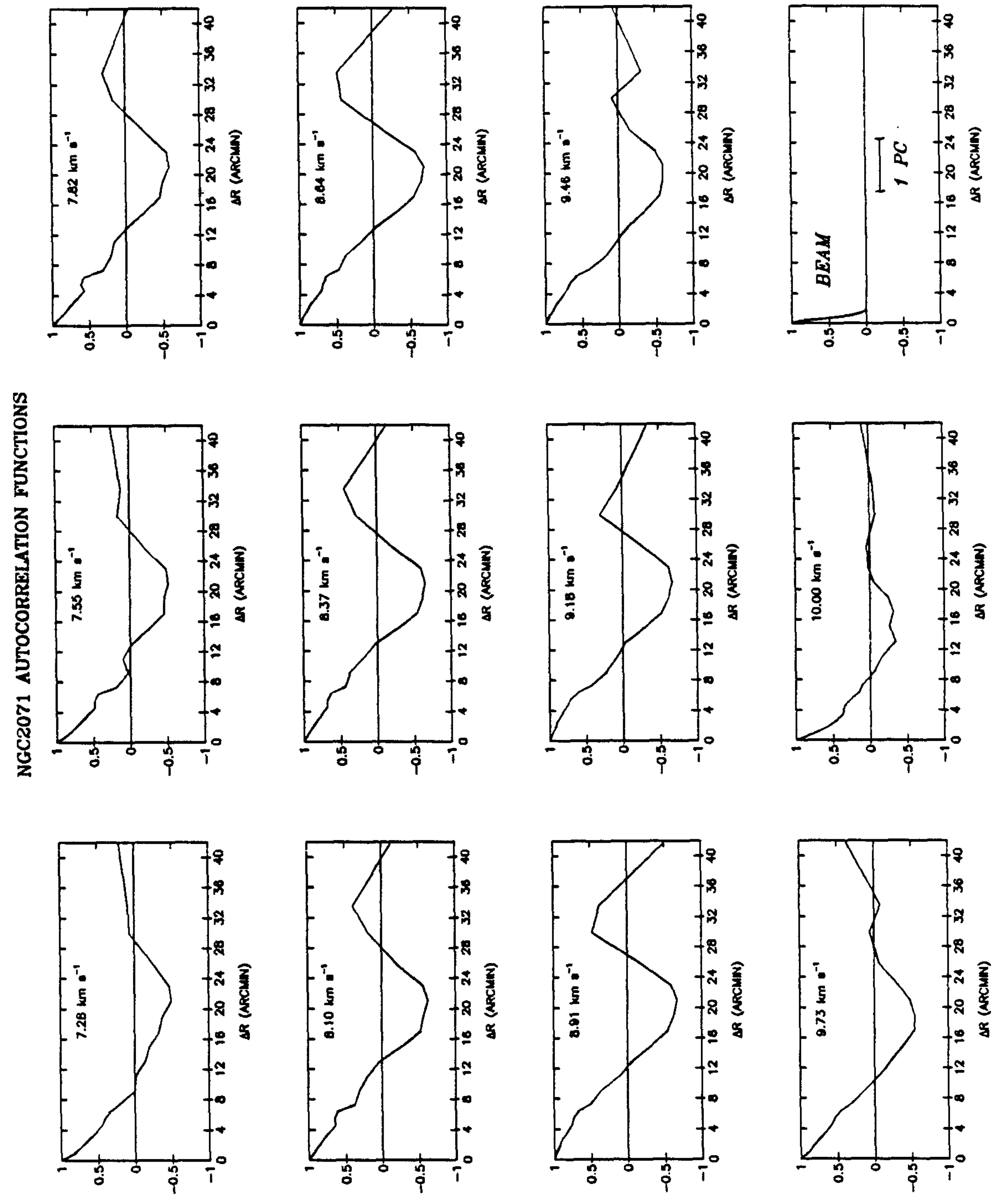
NGC2071 AUTOCORRELATION FUNCTIONS
7.28 km s⁻¹
7.55 km s⁻¹
7.82 km s⁻¹
8.10 km s⁻¹
8.37 km s⁻¹
8.64 km s⁻¹
8.91 km s⁻¹
9.18 km s⁻¹
9.46 km s⁻¹
9.73 km s⁻¹
10.00 km s⁻¹
BEAM
1 PC
1
0.5
0
-0.5
-1
0
4
8
12
16
20
24
28
32
36
40
ΔR (ARCMIN)

Figure 3

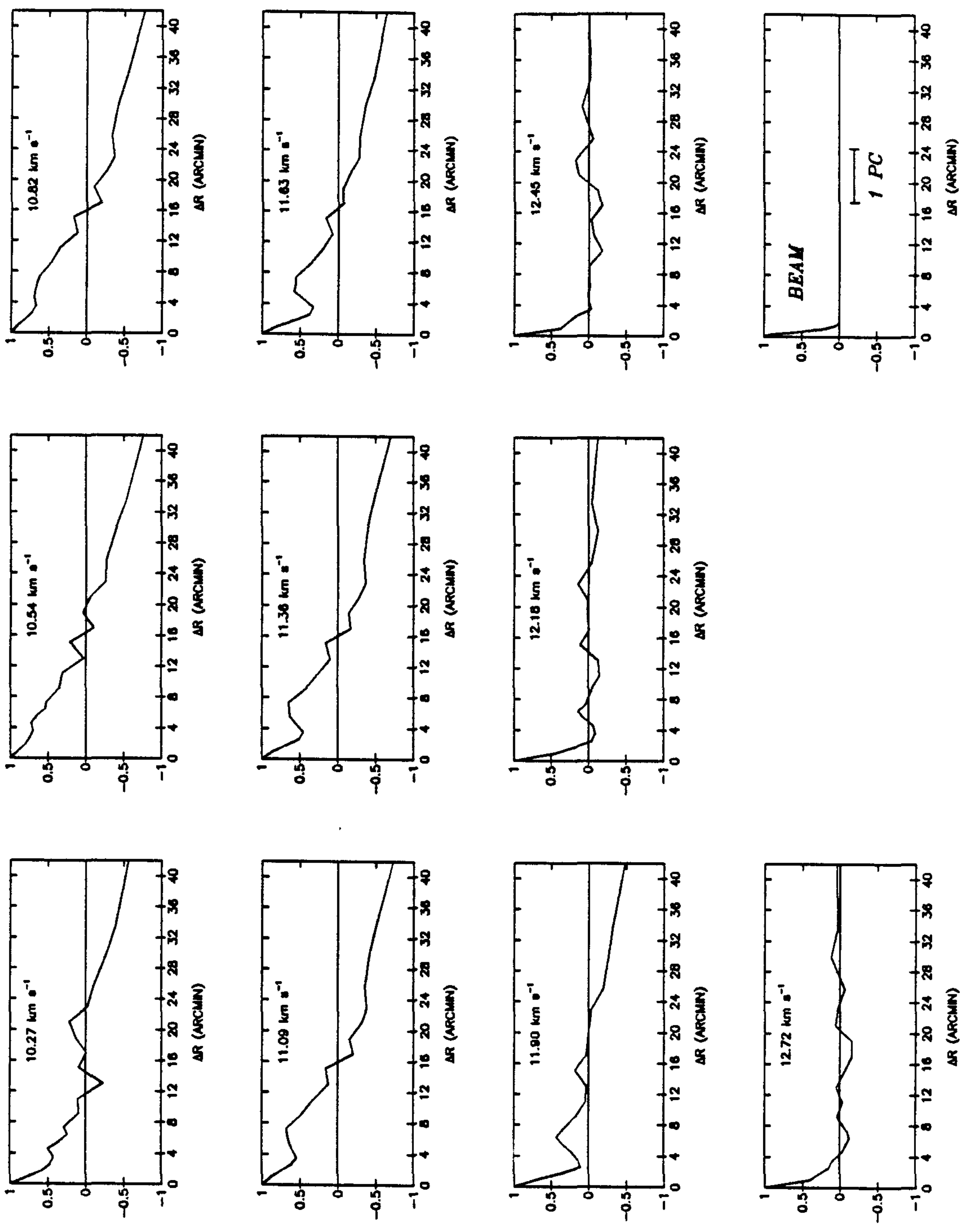

Figure 3

(continued)

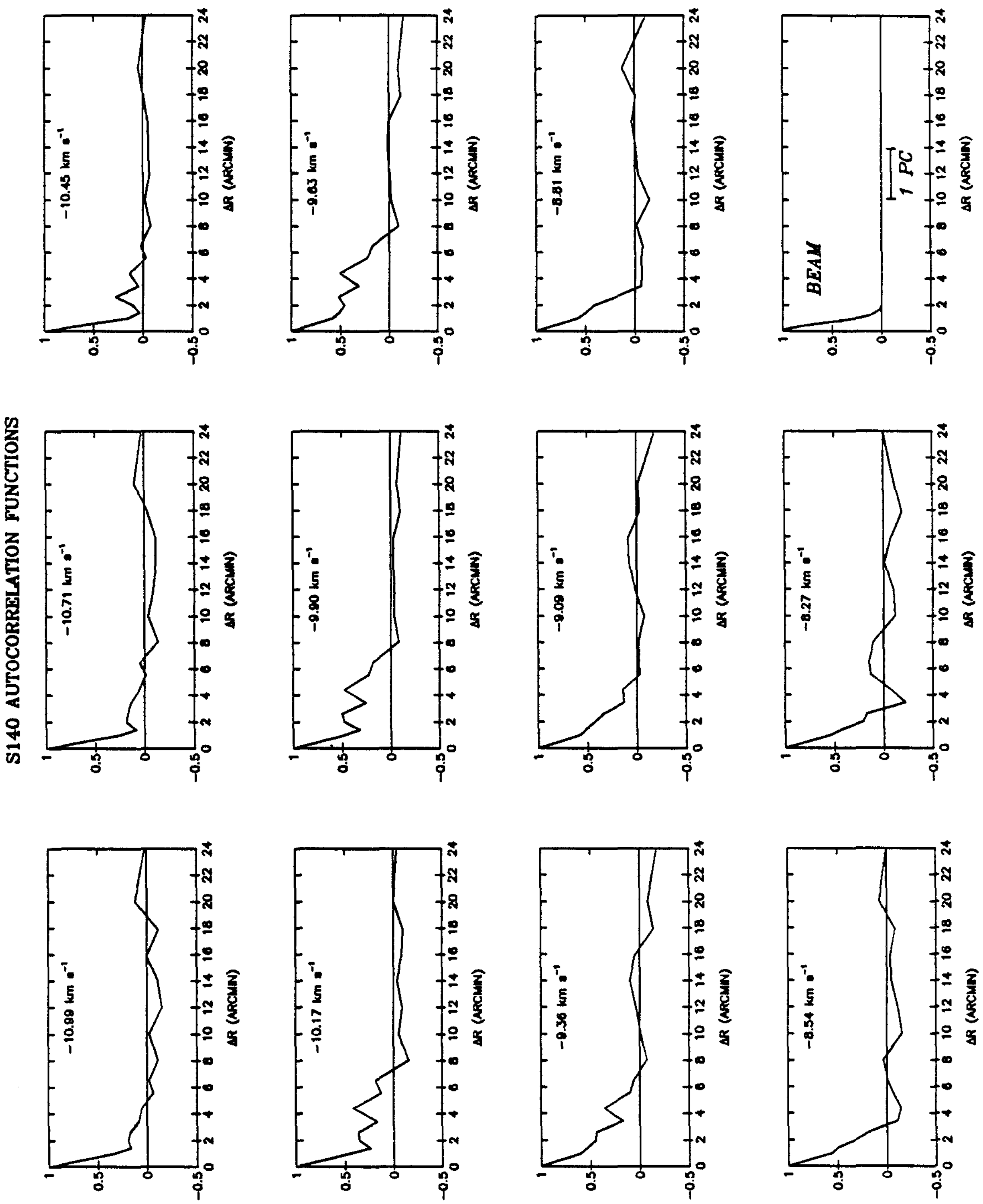
S140 AUTOCORRELATION FUNCTIONS
−10.99 km s^{-1}
−10.71 km s^{-1}
−10.45 km s^{-1}
−10.17 km s^{-1}
−9.90 km s^{-1}
−9.63 km s^{-1}
−9.36 km s^{-1}
−9.09 km s^{-1}
−8.81 km s^{-1}
−8.54 km s^{-1}
−8.27 km s^{-1}
BEAM
1 PC
1
0.5
0
−0.5
0 2 4 6 8 10 12 14 16 18 20 22 24
ΔR (ARCMIN)

Figure 4

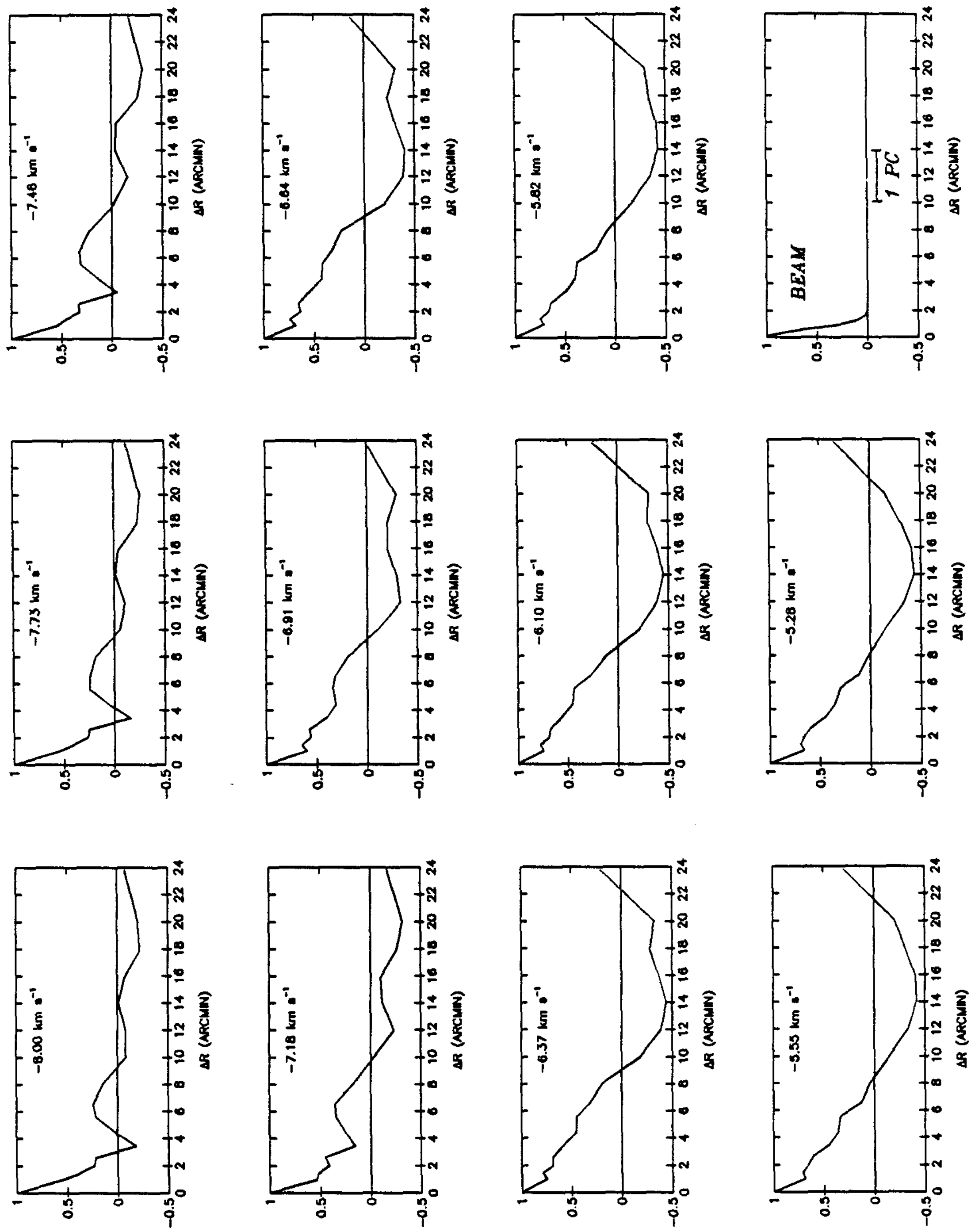

Figure 4

(continued)

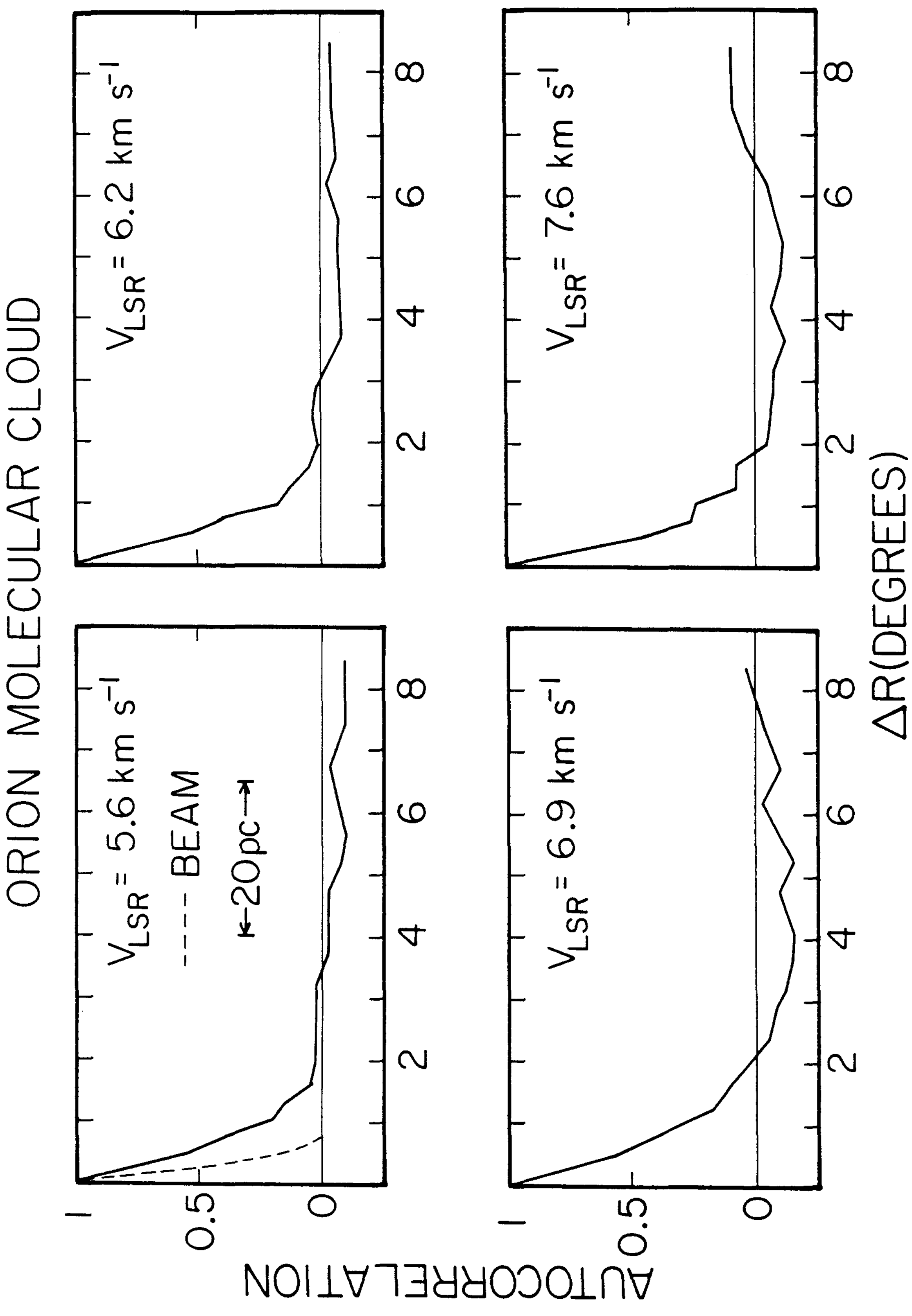
ORION MOLECULAR CLOUD
V_LSR = 5.6 km s^-1
---- BEAM
←20pc→
V_LSR = 6.2 km s^-1
V_LSR = 6.9 km s^-1
V_LSR = 7.6 km s^-1
1
0.5
0
2
4
6
8
ΔR(DEGREES)
AUTOCORRELATION

Figure 5

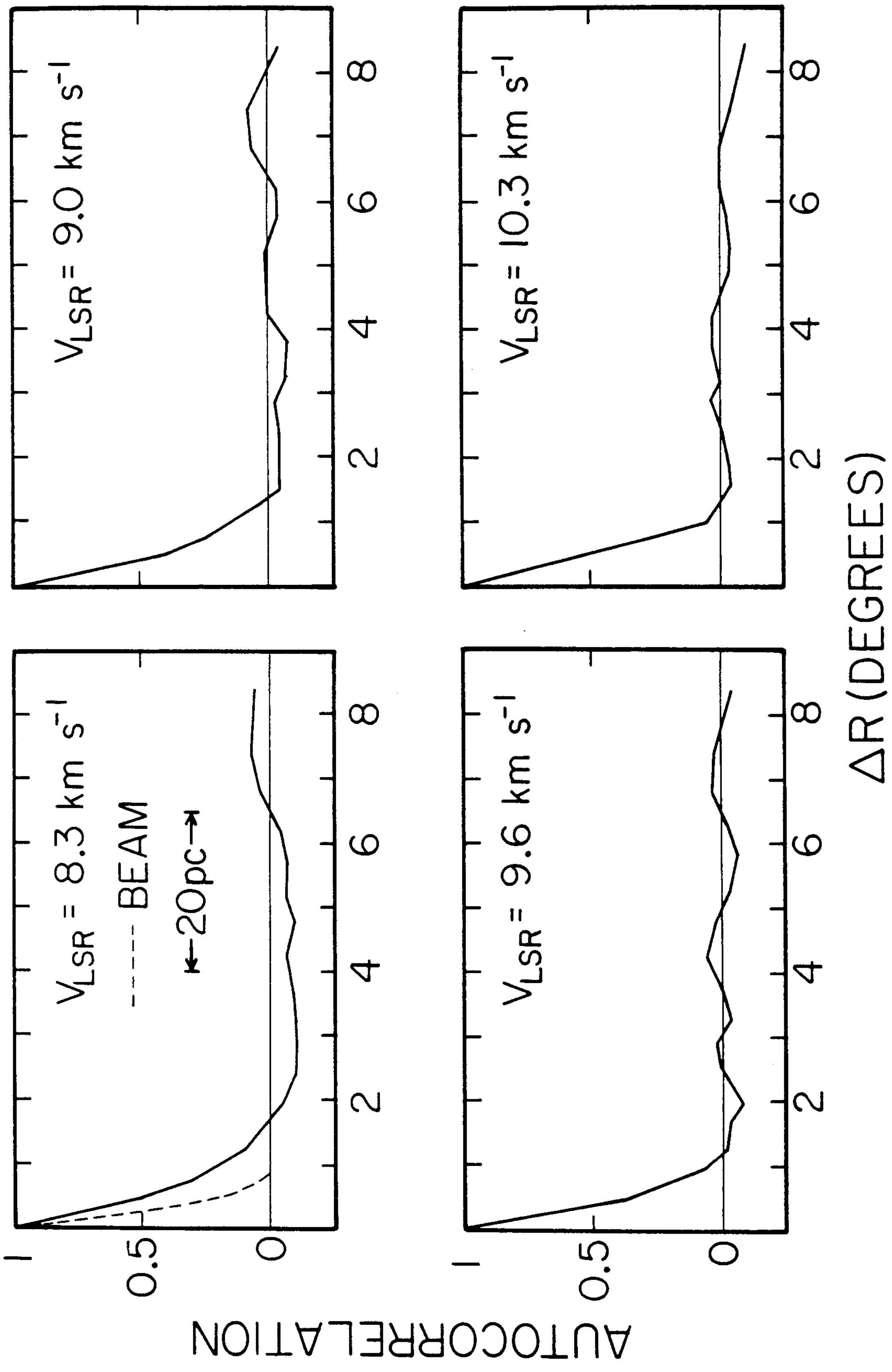

Figure 5 (continued)

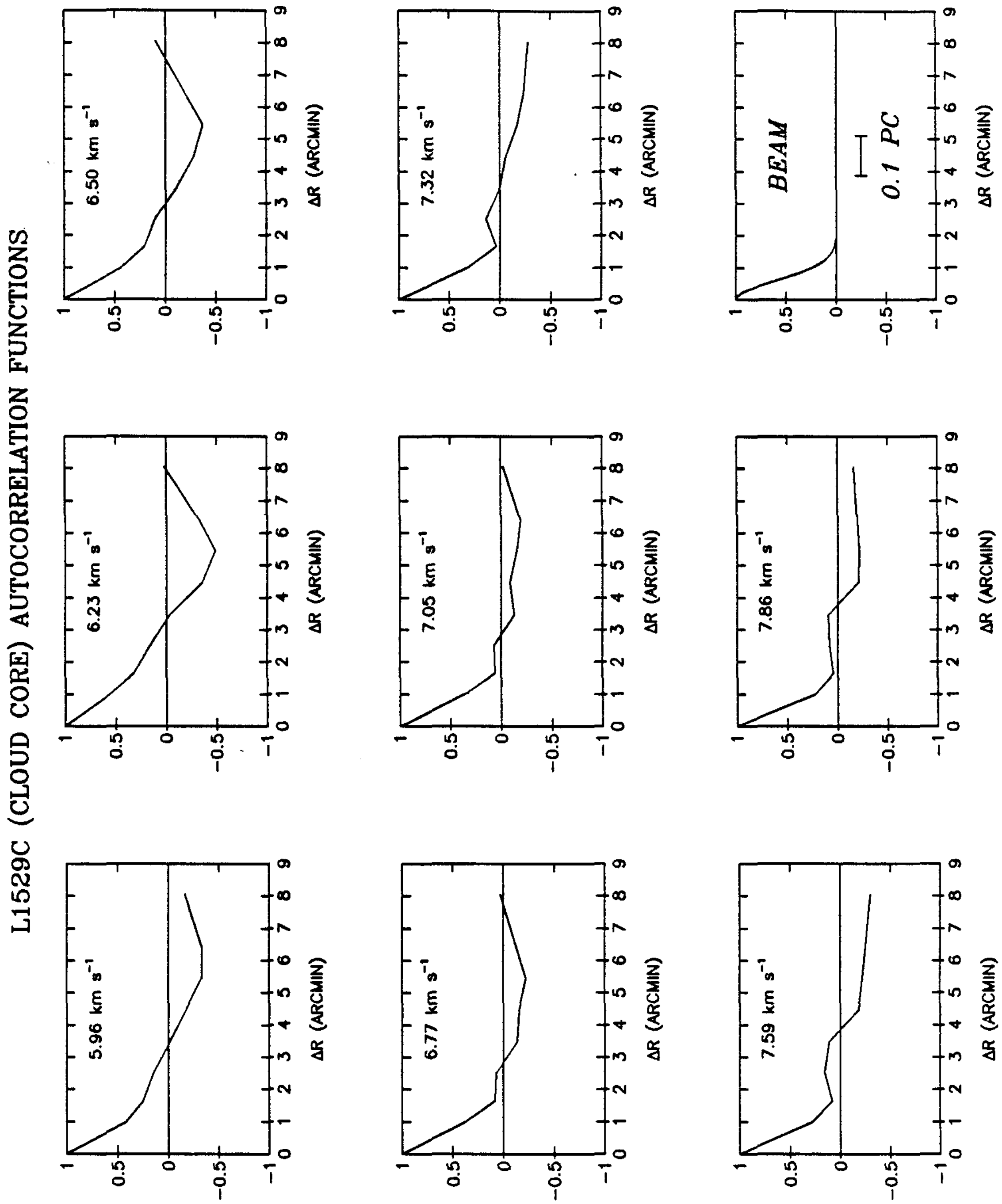
L1529C (CLOUD CORE) AUTOCORRELATION FUNCTIONS
5.96 km s^{-1}
6.23 km s^{-1}
6.50 km s^{-1}
6.77 km s^{-1}
7.05 km s^{-1}
7.32 km s^{-1}
7.59 km s^{-1}
7.86 km s^{-1}
BEAM
0.1 PC
1
0.5
0
-0.5
-1
0 1 2 3 4 5 6 7 8 9
ΔR (ARCMIN)

Figure 6

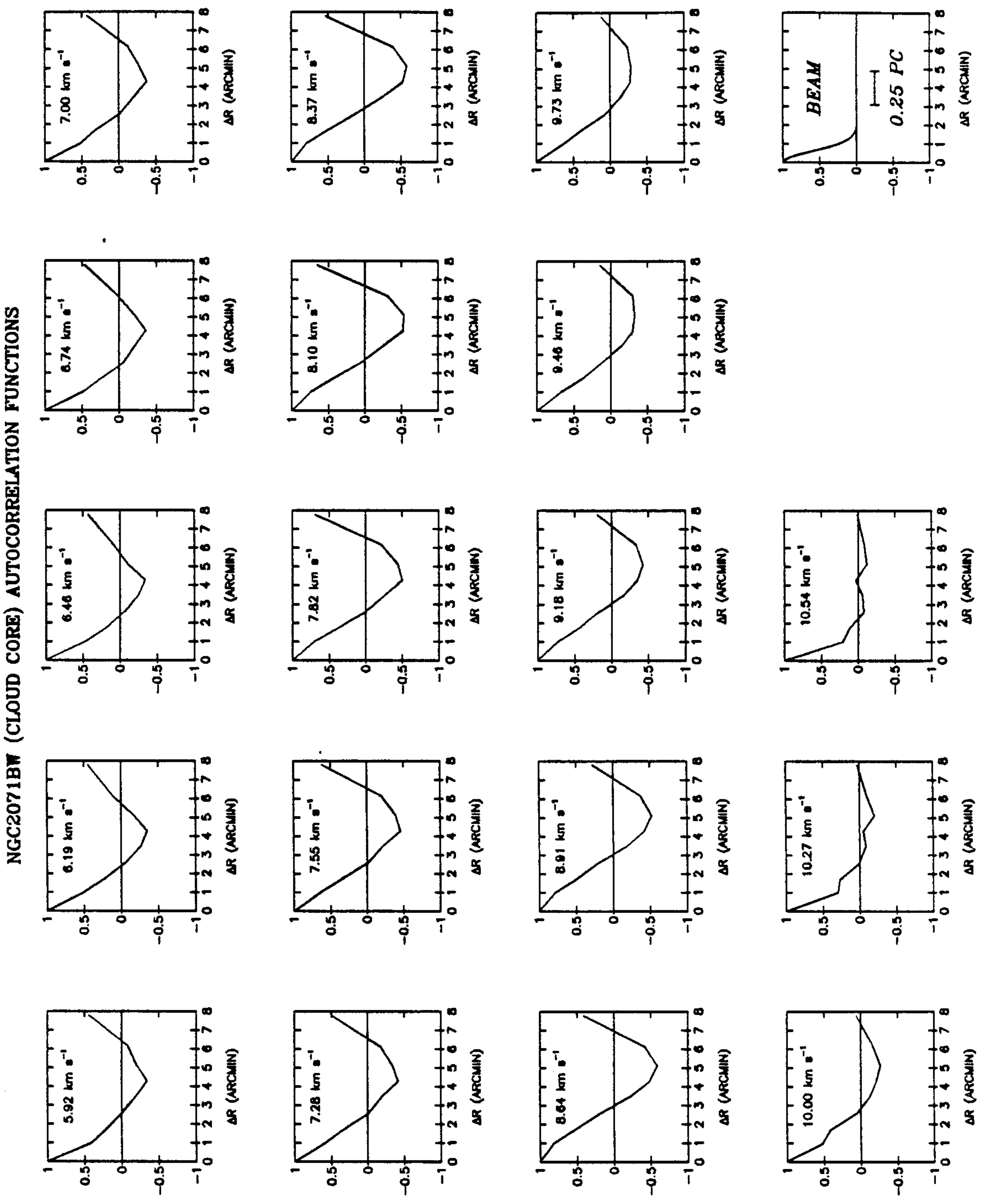
NGC2071BW (CLOUD CORE) AUTOCORRELATION FUNCTIONS
5.92 km s⁻¹
6.19 km s⁻¹
6.46 km s⁻¹
6.74 km s⁻¹
7.00 km s⁻¹
7.28 km s⁻¹
7.55 km s⁻¹
7.82 km s⁻¹
8.10 km s⁻¹
8.37 km s⁻¹
8.64 km s⁻¹
8.91 km s⁻¹
9.18 km s⁻¹
9.46 km s⁻¹
9.73 km s⁻¹
10.00 km s⁻¹
10.27 km s⁻¹
10.54 km s⁻¹
BEAM
0.25 PC
1
0.5
0
-0.5
-1
0 1 2 3 4 5 6 7 8
ΔR (ARCMIN)

Figure 7

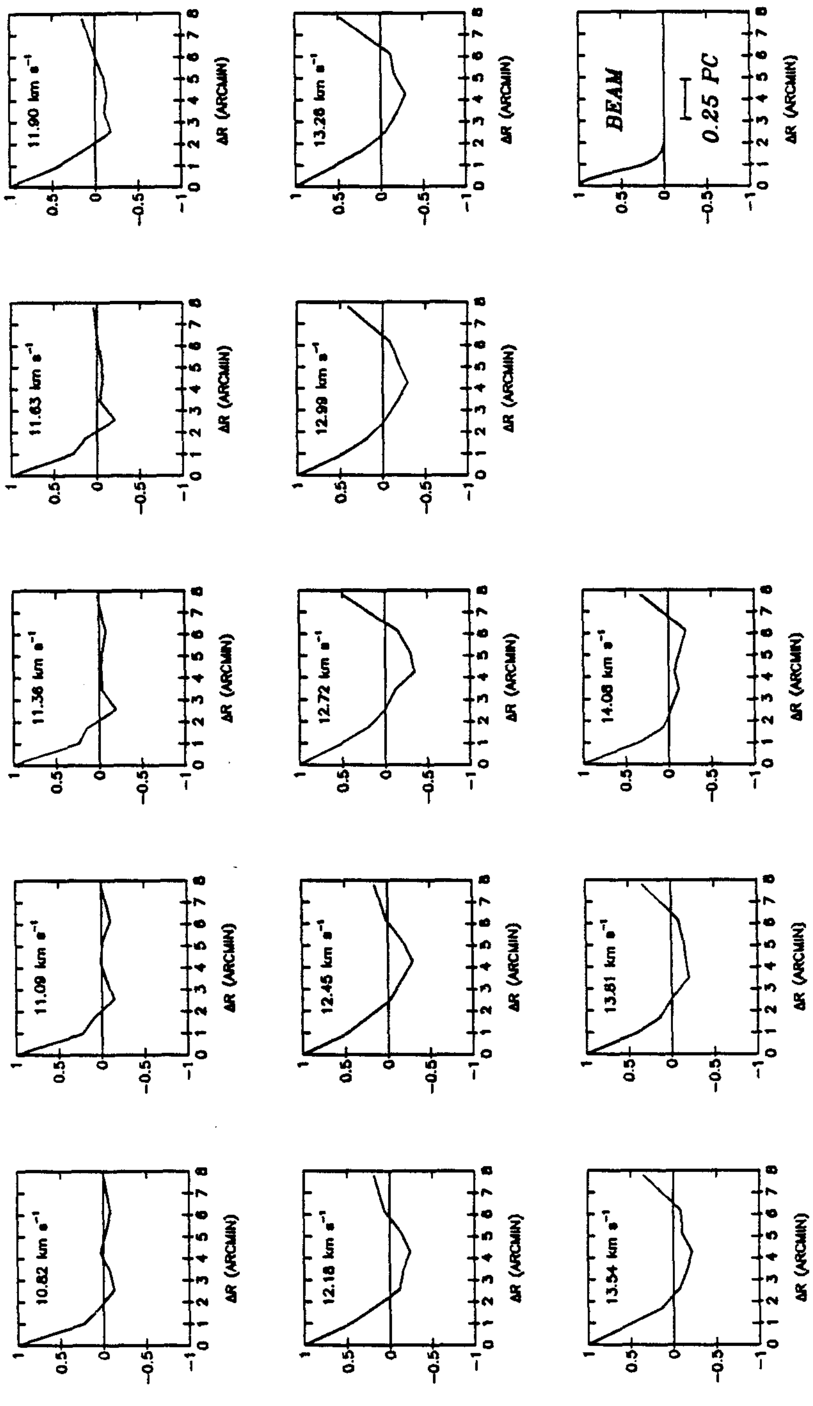

Figure 7

(continued)

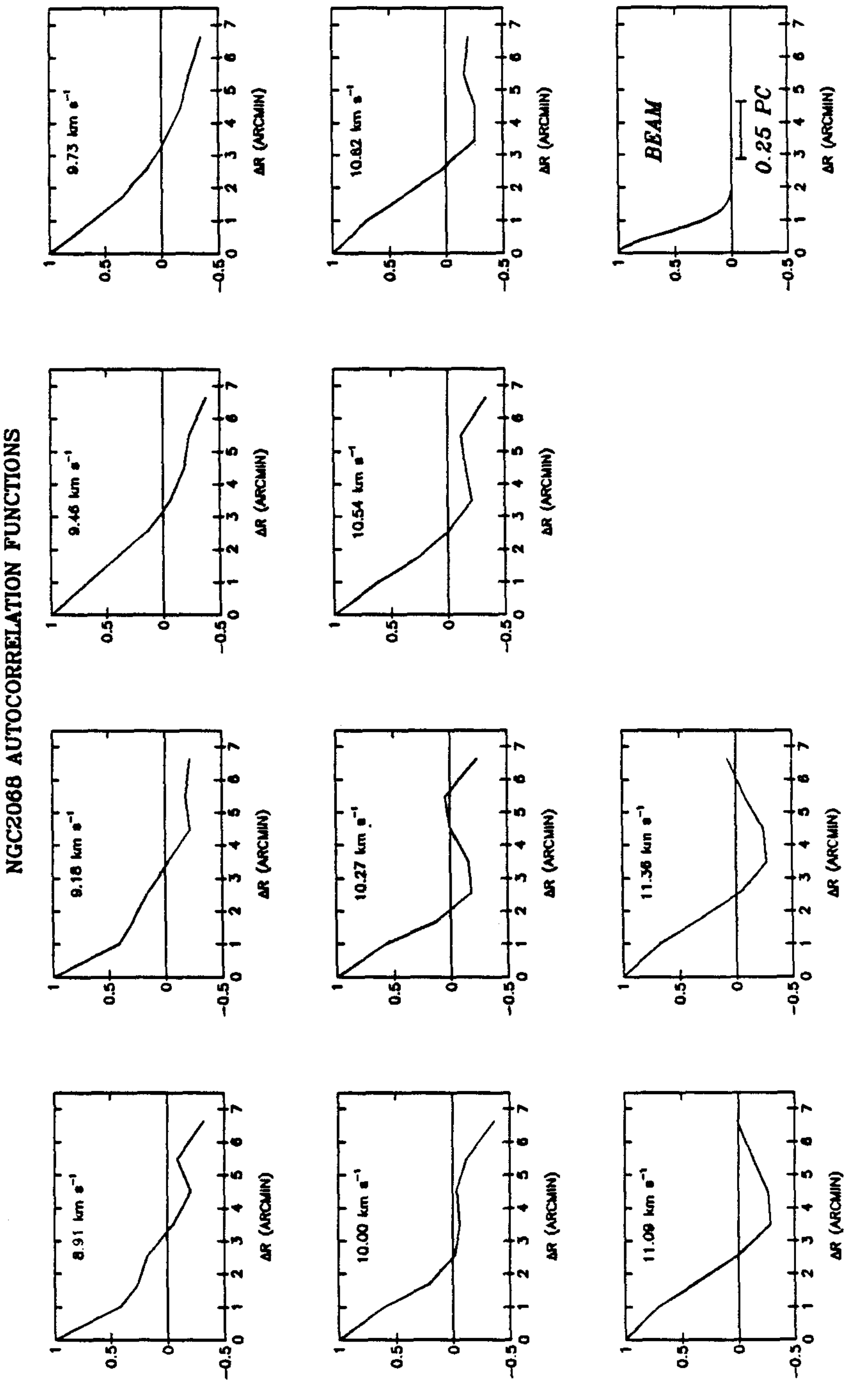
NGC2068 AUTOCORRELATION FUNCTIONS
8.91 km s⁻¹
9.18 km s⁻¹
9.46 km s⁻¹
9.73 km s⁻¹
10.00 km s⁻¹
10.27 km s⁻¹
10.54 km s⁻¹
10.82 km s⁻¹
11.09 km s⁻¹
11.36 km s⁻¹
BEAM
0.25 PC
ΔR (ARCMIN)
0 1 2 3 4 5 6 7
1
0.5
0
-0.5

Figure 8

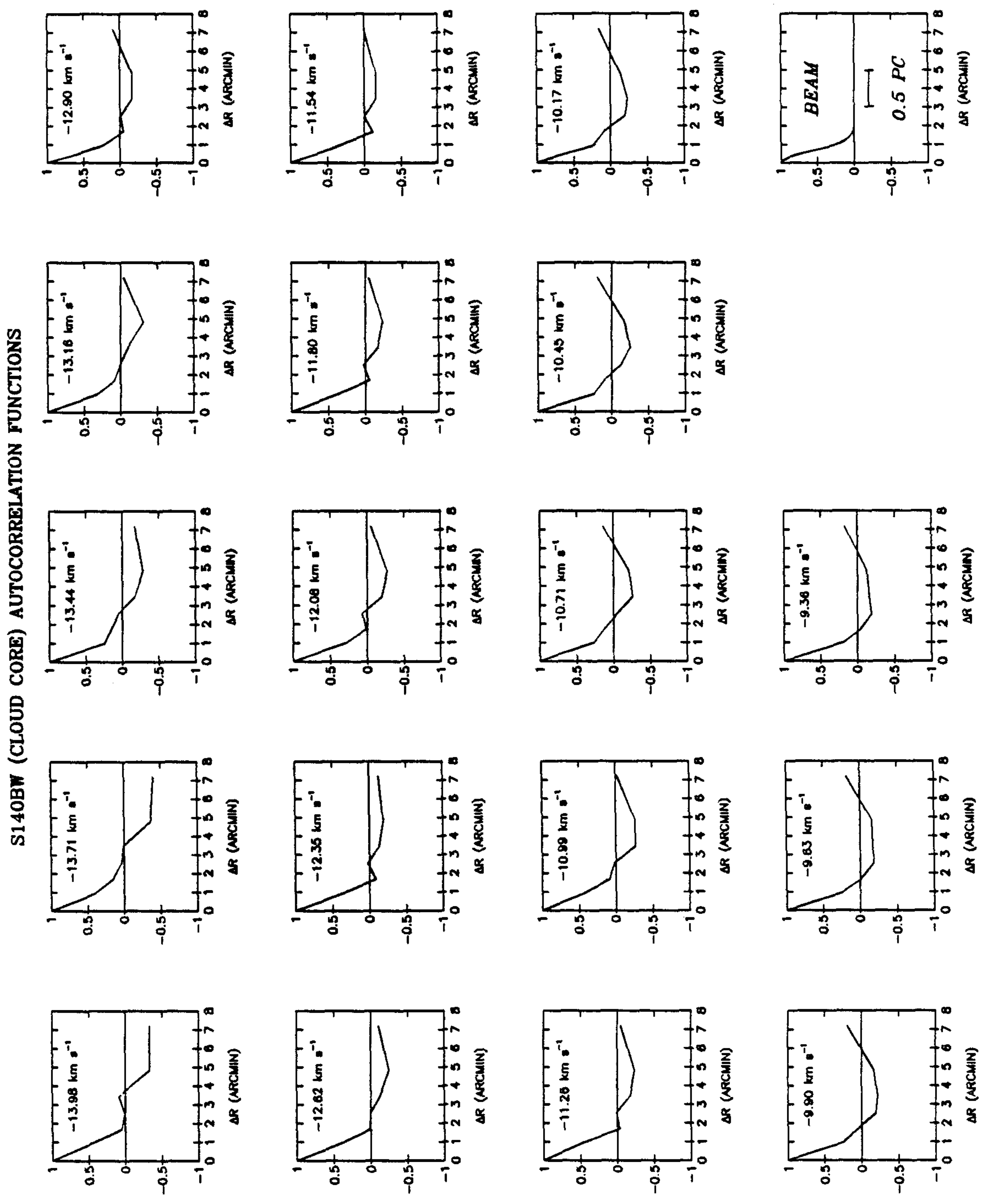
S140BW (CLOUD CORE) AUTOCORRELATION FUNCTIONS

Figure 9

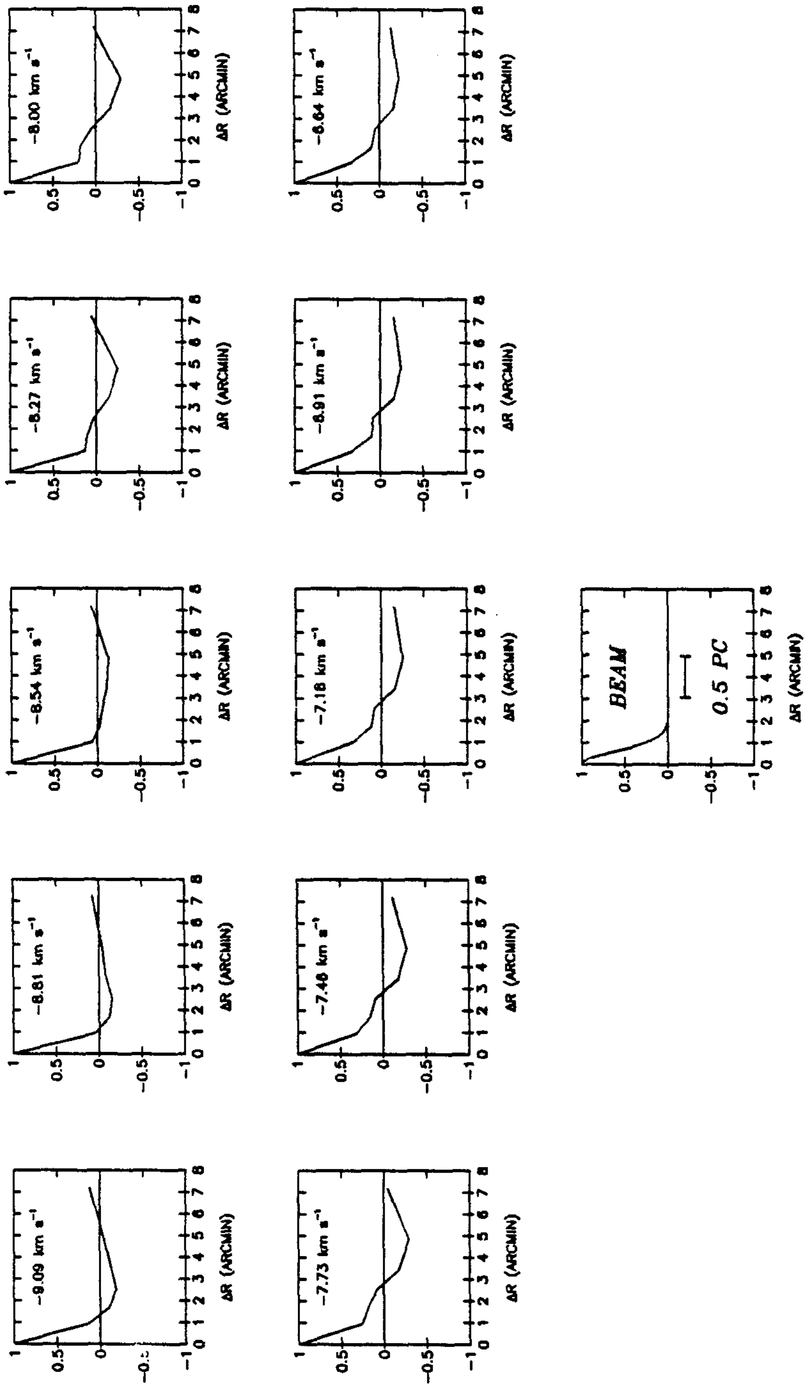

Figure 9

(continued)

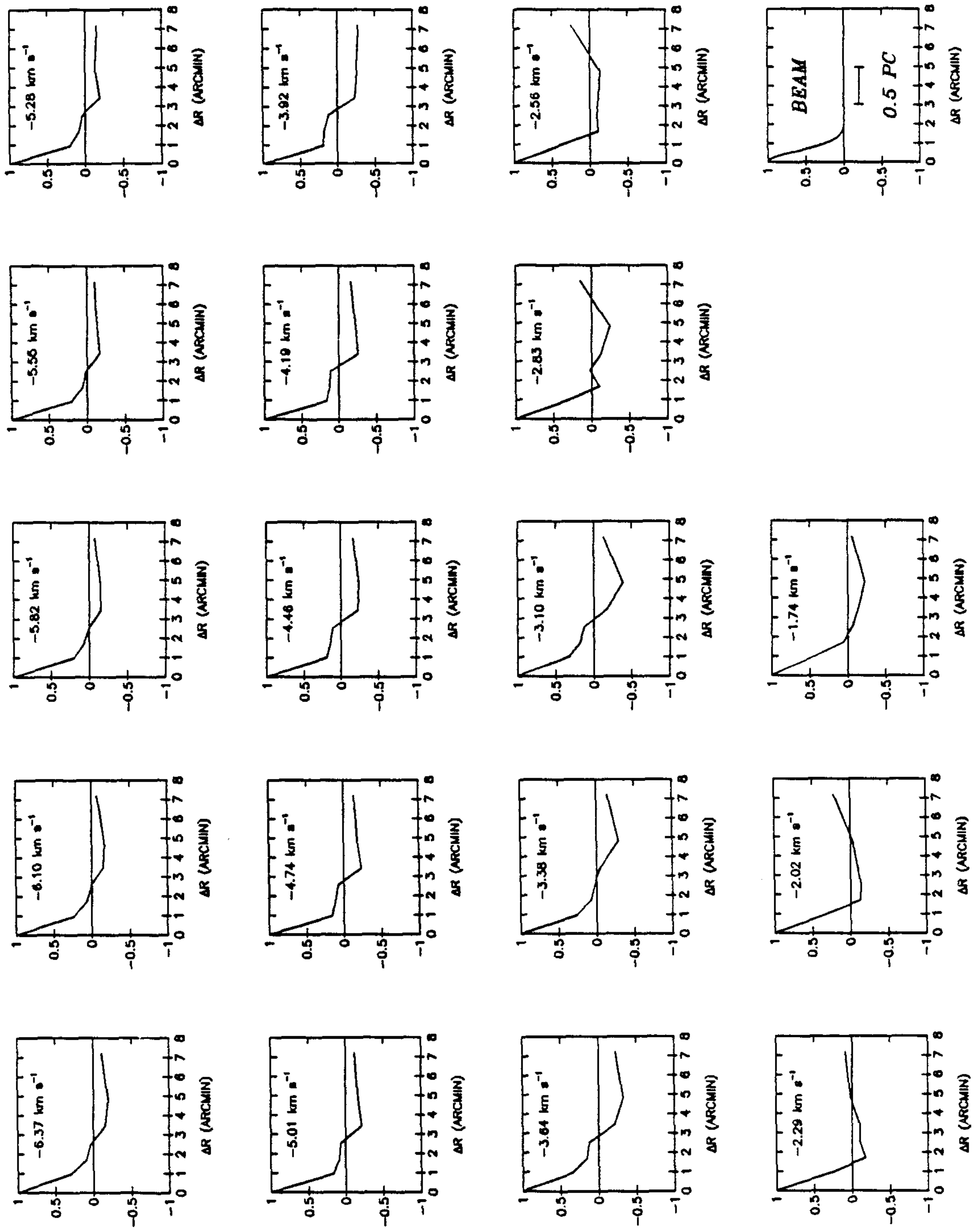

Figure 9

(continued)

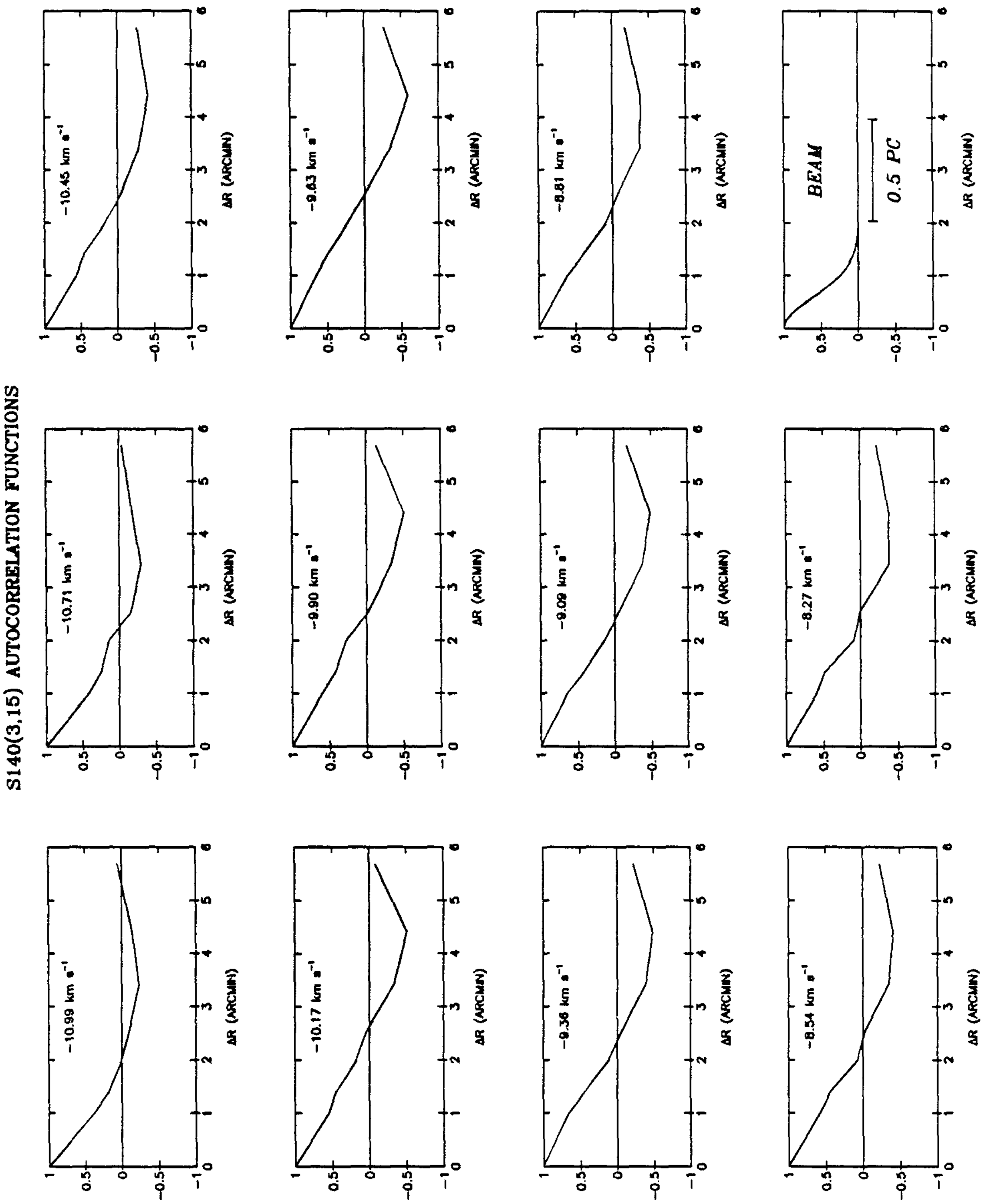
S140(3,15) AUTOCORRELATION FUNCTIONS
−10.99 km s^{-1}
−10.71 km s^{-1}
−10.45 km s^{-1}
−10.17 km s^{-1}
−9.90 km s^{-1}
−9.63 km s^{-1}
−9.36 km s^{-1}
−9.09 km s^{-1}
−8.81 km s^{-1}
−8.54 km s^{-1}
−8.27 km s^{-1}
BEAM
0.5 PC
ΔR (ARCMIN)
0
1
2
3
4
5
6
1
0.5
0
−0.5
−1

Figure 10

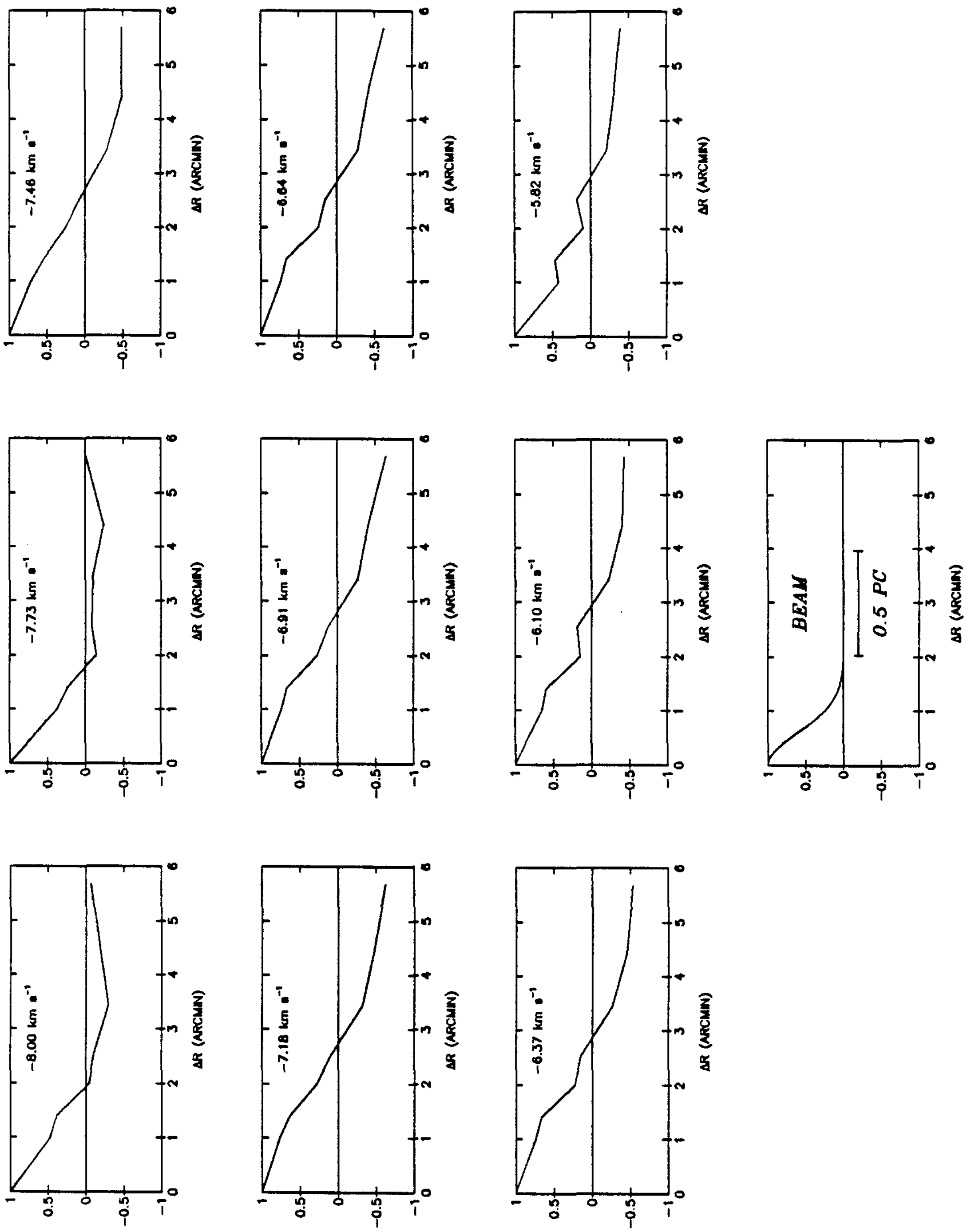

Figure 10

(continued)

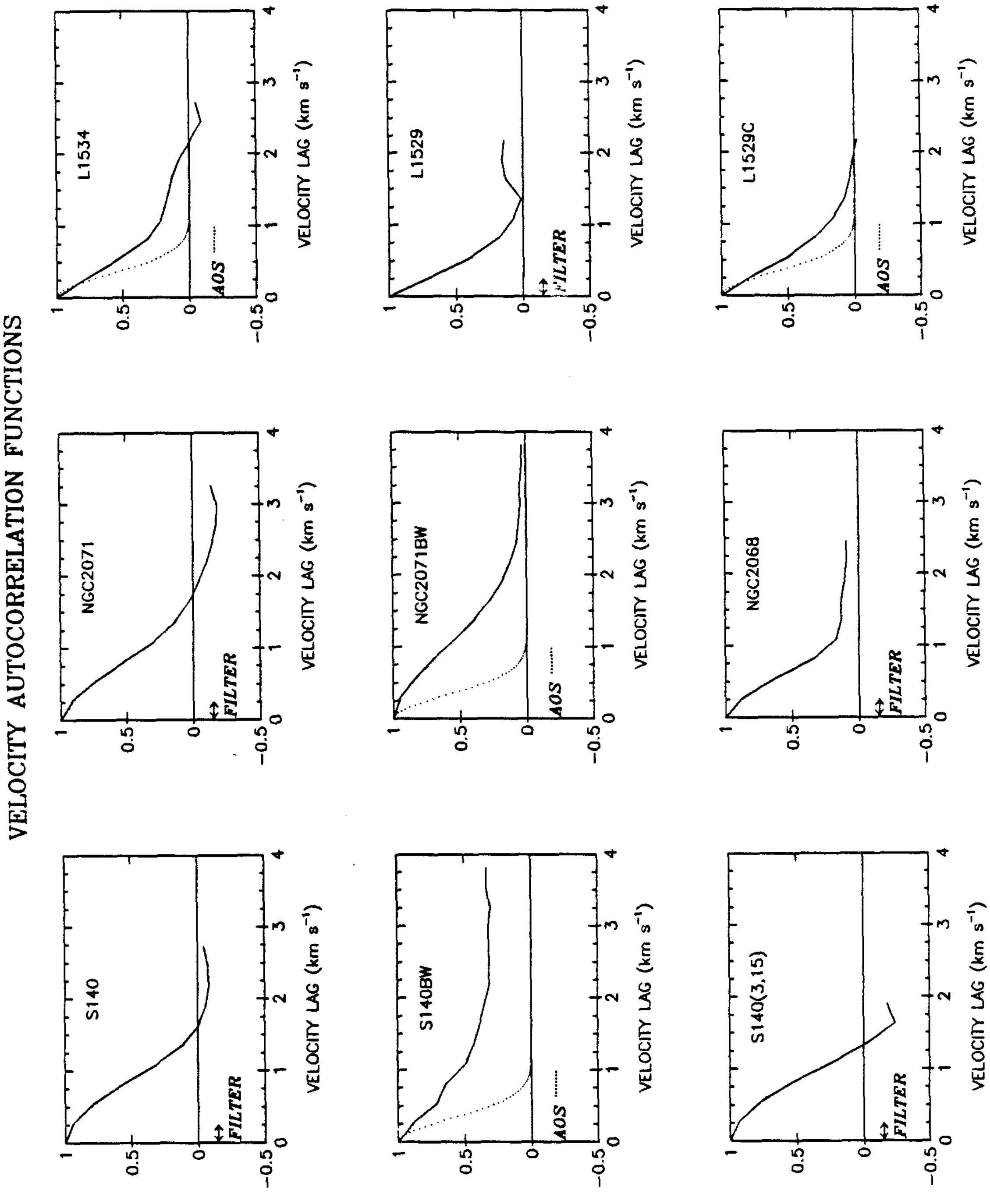
VELOCITY AUTOCORRELATION FUNCTIONS

Figure 11

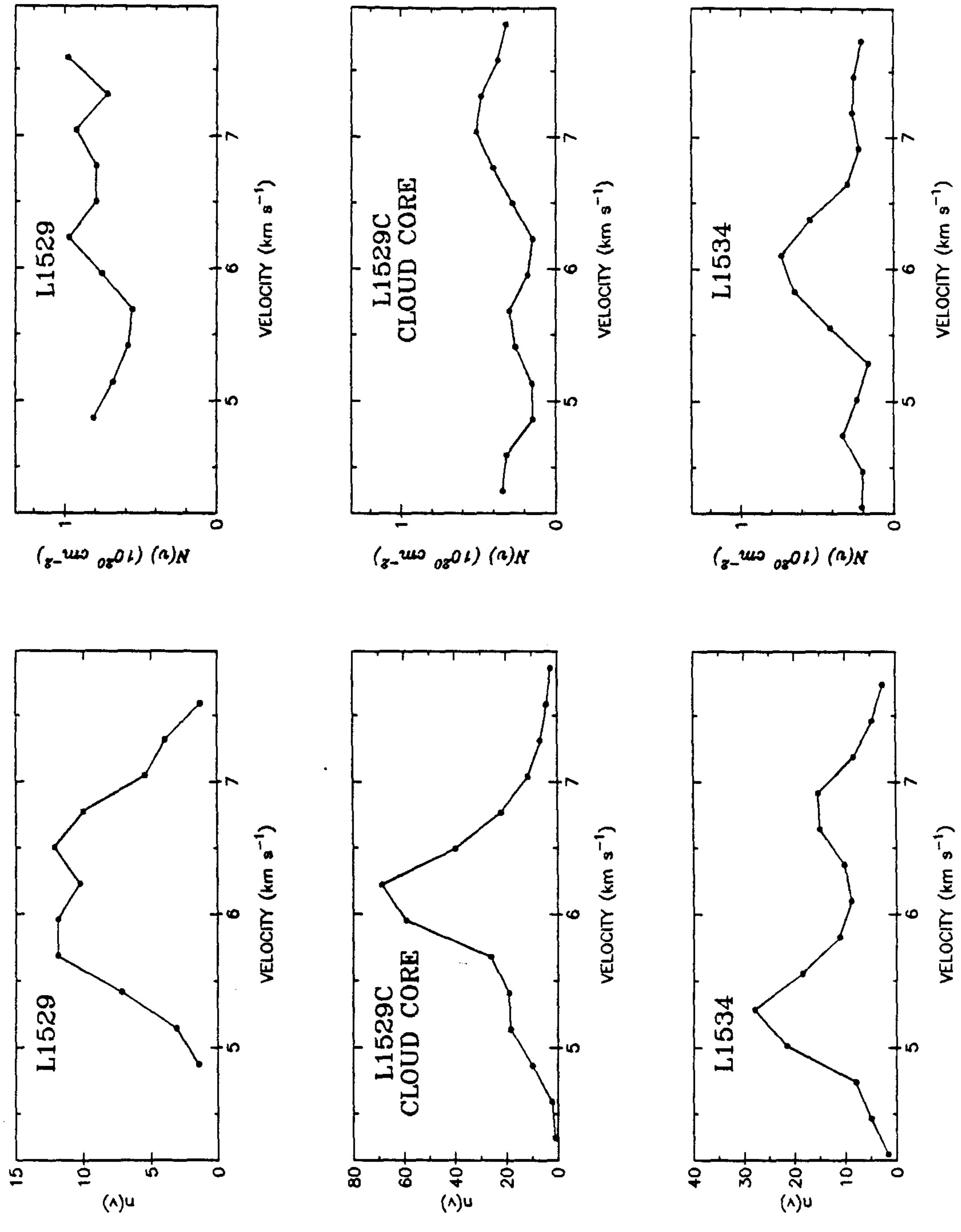
L1529
L1529C
CLOUD CORE
L1534
L1529
L1529C
CLOUD CORE
L1534
$N(v)$ (10^{20} cm^{-2})
$n(v)$
VELOCITY (km s^{-1})
0
1
5
6
7
0
5
10
15
0
20
40
60
80
0
10
20
30
40

Figure 12a

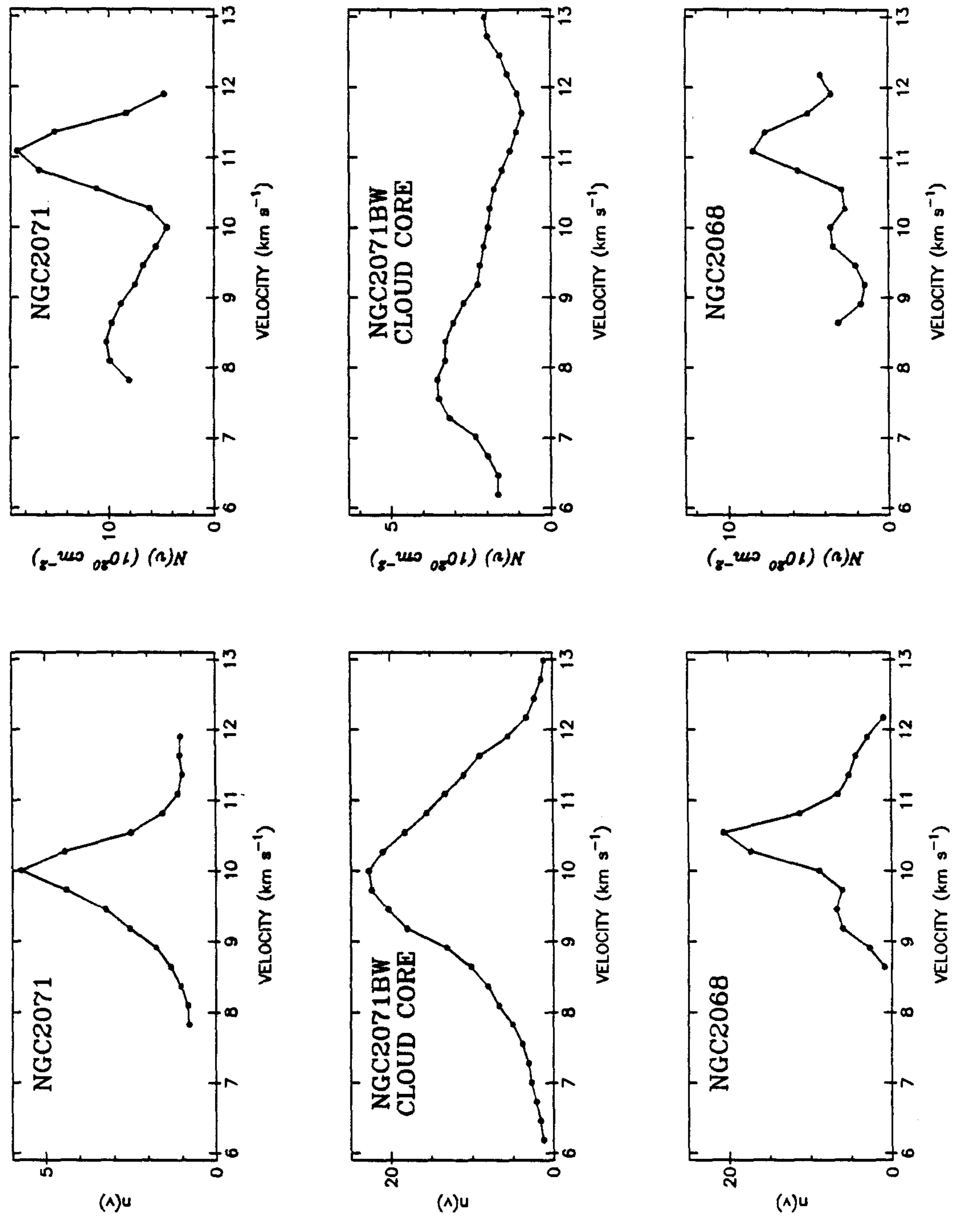
NGC2071
NGC2071BW CLOUD CORE
NGC2068
NGC2071
NGC2071BW CLOUD CORE
NGC2068
N(υ) (10^20 cm^-2)
n(v)
VELOCITY (km s^-1)
6
7
8
9
10
11
12
13
0
5
10
20

Figure 12b

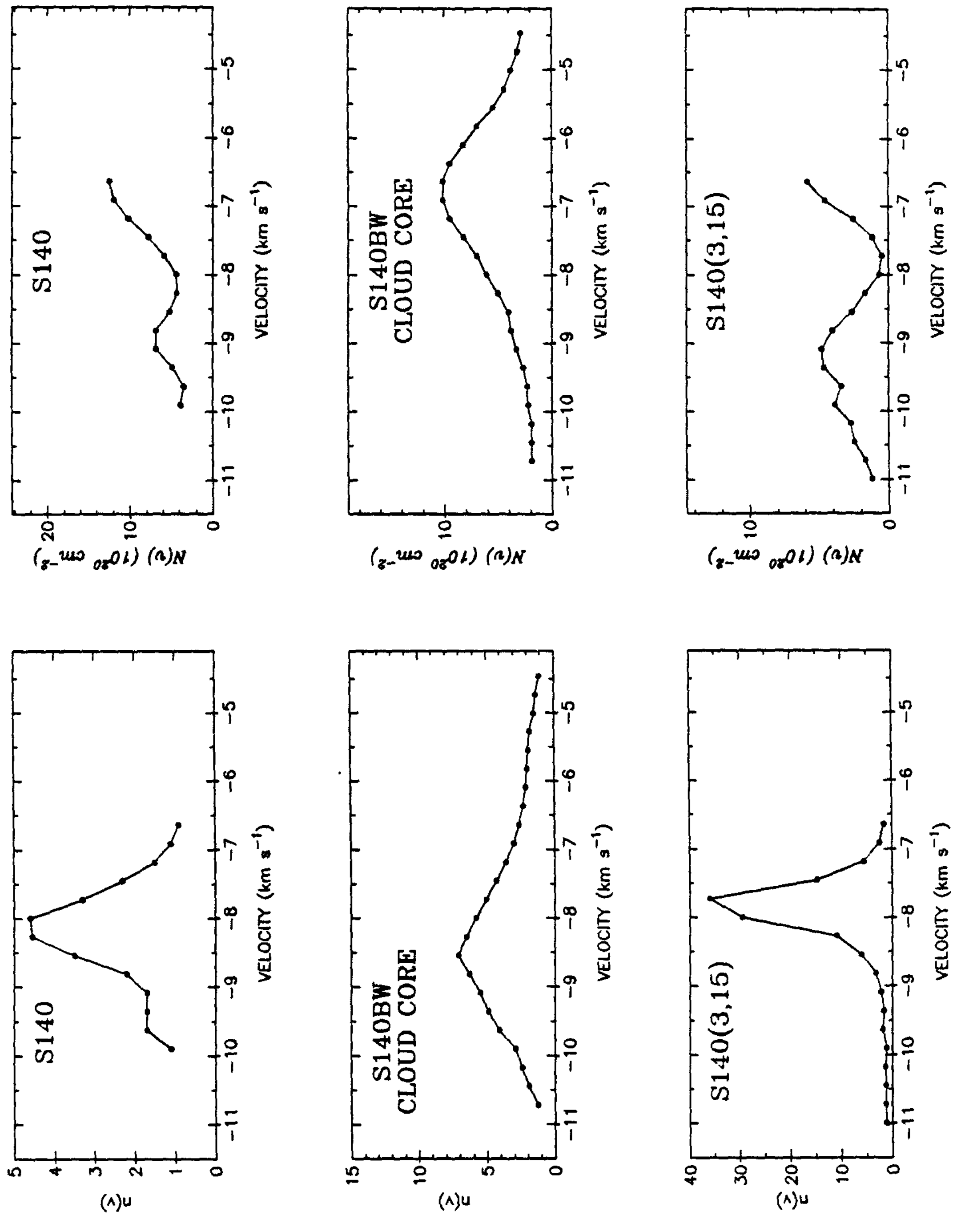
S140
S140BW
CLOUD CORE
S140(3,15)
N(v) (10^20 cm^-2)
n(v)
VELOCITY (km s^-1)
-11
-10
-9
-8
-7
-6
-5
0
10
20
1
2
3
4
5
15
30
40

Figure 12c

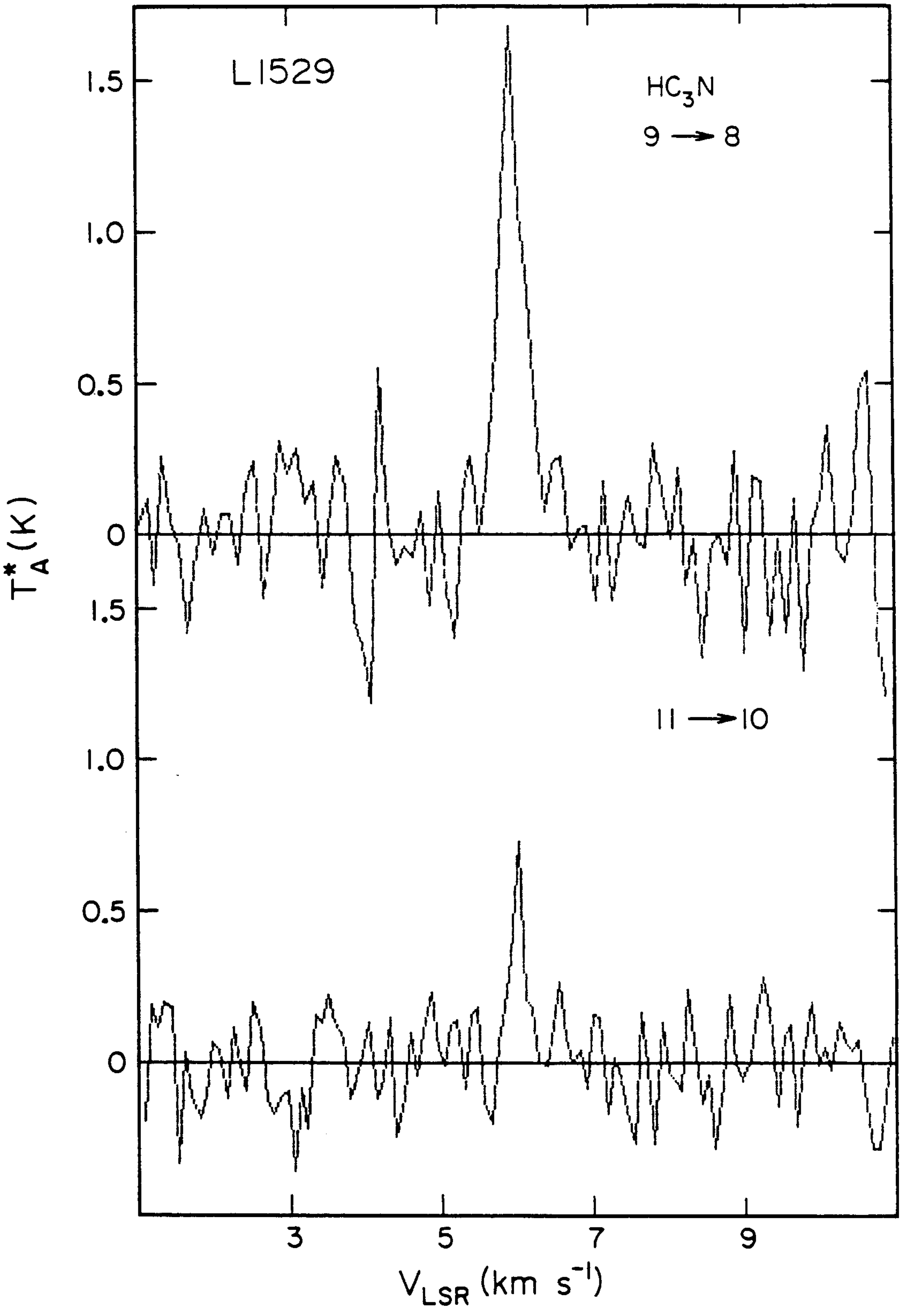

Figure 13a

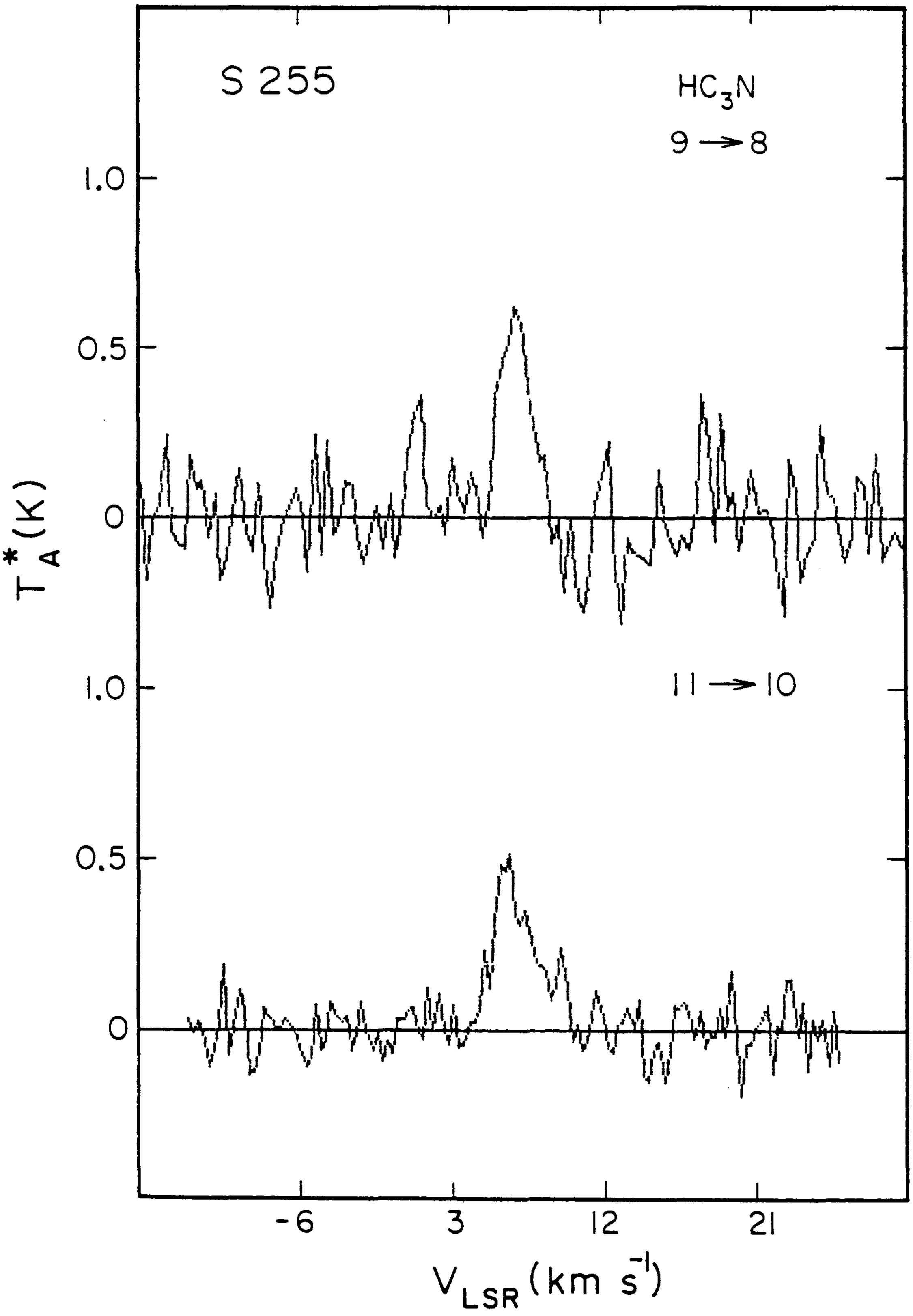

Figure 13b

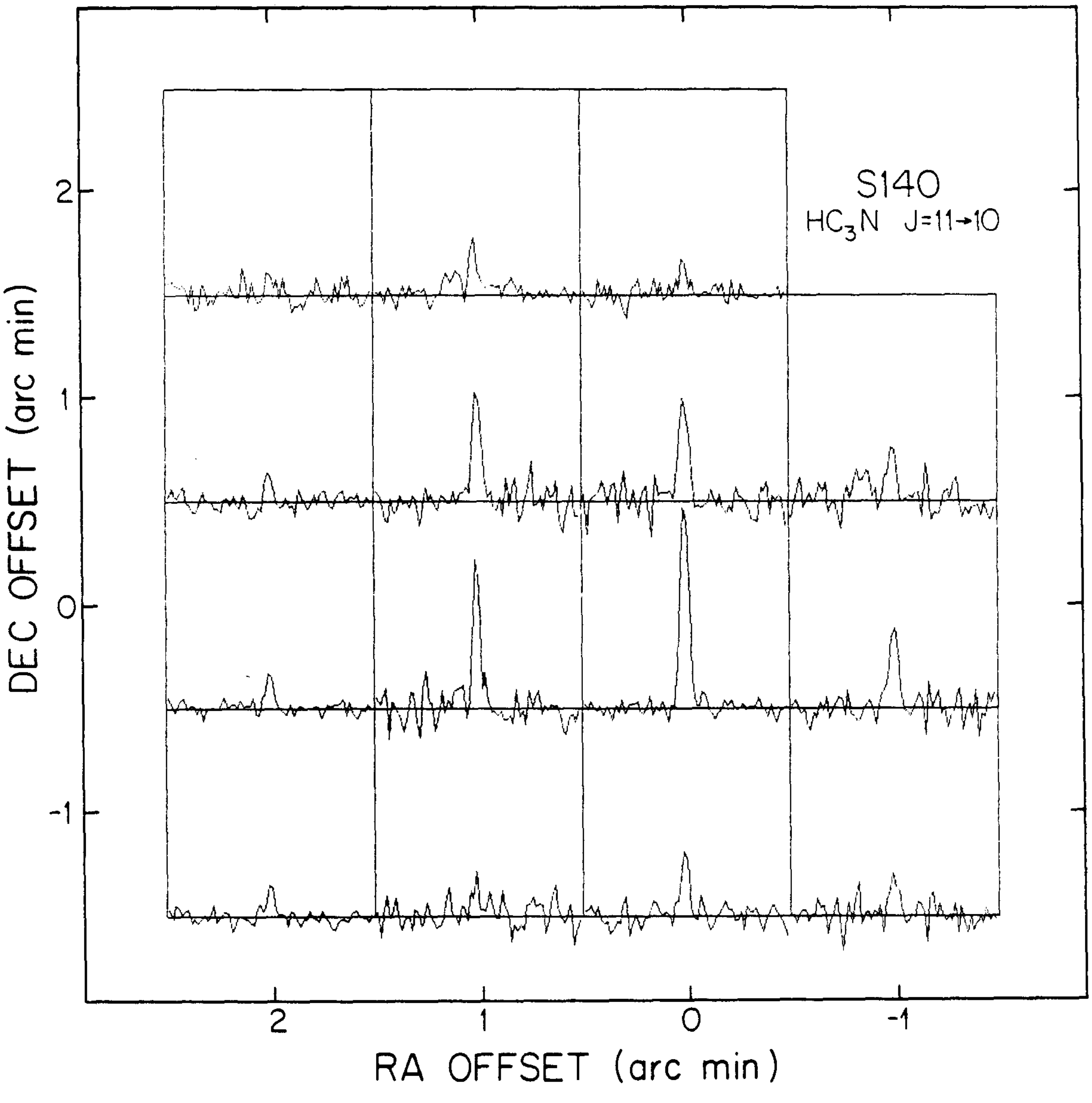
S140
HC_3N J=11→10
DEC OFFSET (arc min)
2
1
0
-1
RA OFFSET (arc min)
2
1
0
-1

Figure 13c

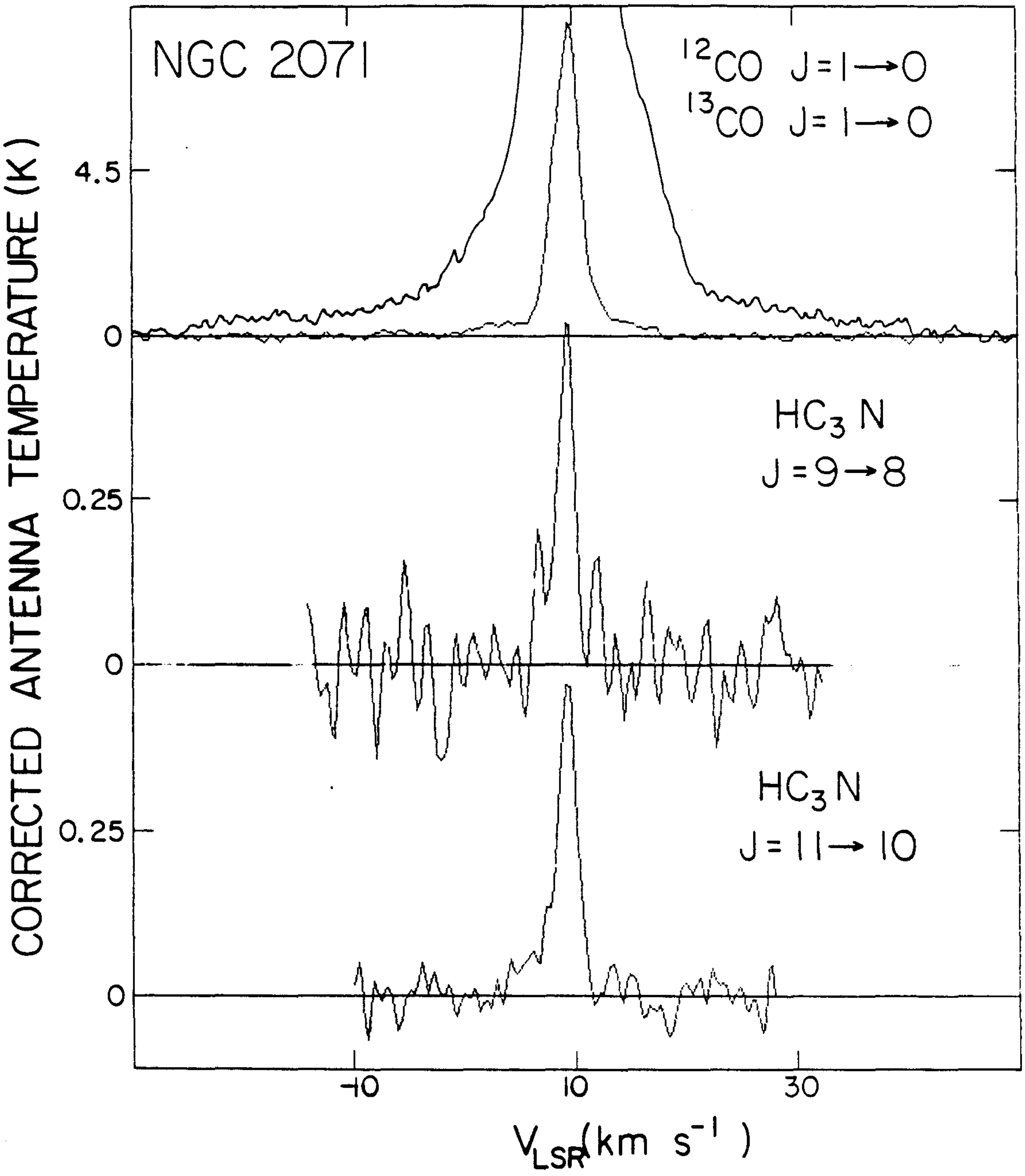
NGC 2071
^{12}CO J=1→0
^{13}CO J=1→0
HC$_3$N
J=9→8
HC$_3$N
J=11→10
CORRECTED ANTENNA TEMPERATURE (K)
4.5
0
0.25
0
0.25
0
-10
10
30
V$_{LSR}$(km s^{-1})

Figure 13d

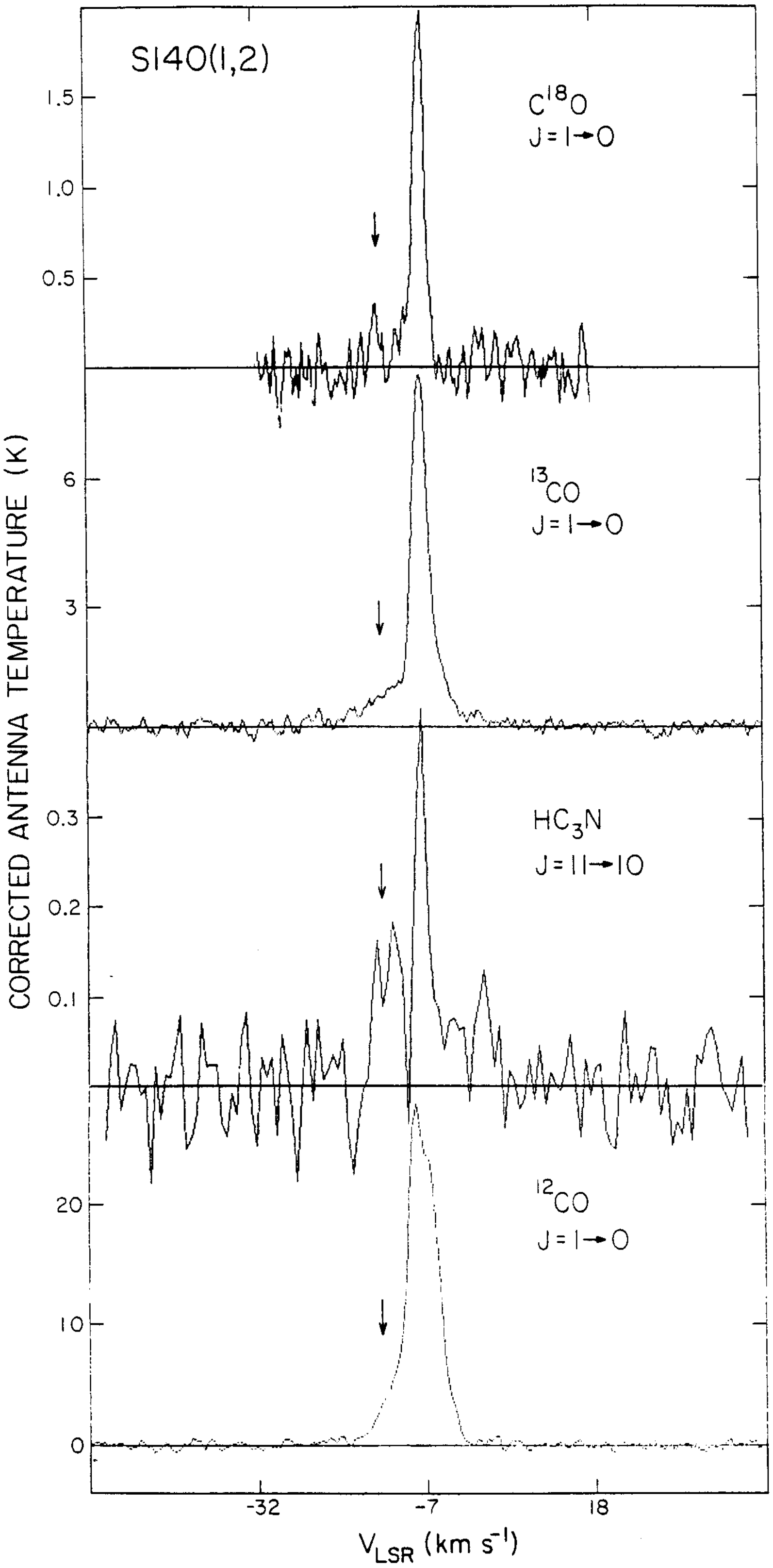
S140(1,2)
$C^{18}O$
J = 1→0
1.5
1.0
0.5
^{13}CO
J = 1→0
6
3
HC_3N
J = 11→10
0.3
0.2
0.1
^{12}CO
J = 1→0
20
10
0
CORRECTED ANTENNA TEMPERATURE (K)
-32
-7
18
V_{LSR} (km s^{-1})

Figure 13e

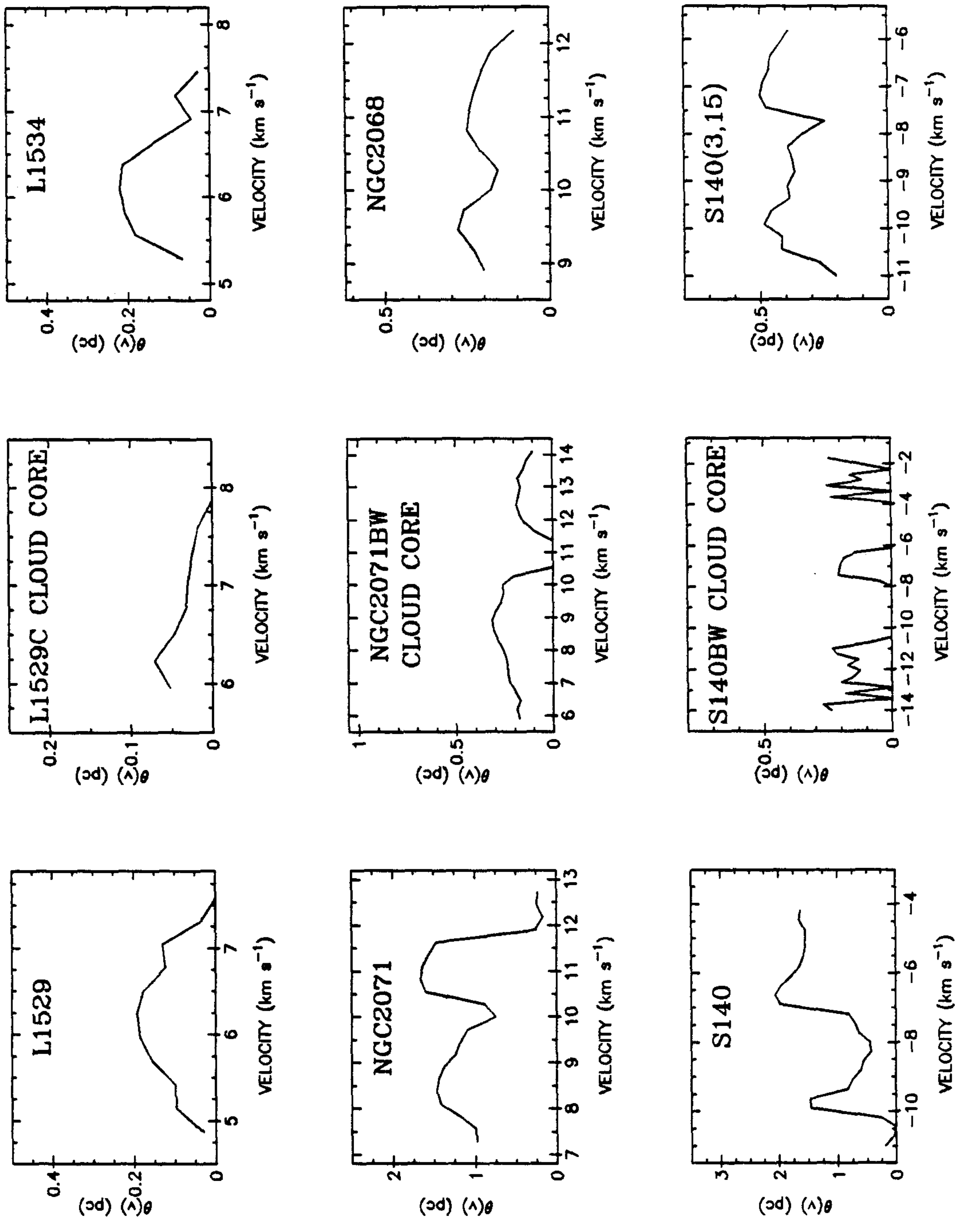
L1529
L1529C CLOUD CORE
L1534
NGC2071
NGC2071BW CLOUD CORE
NGC2068
S140
S140BW CLOUD CORE
S140(3,15)
θ(v) (pc)
VELOCITY (km s⁻¹)
0
0.2
0.4
0.1
0.5
1
2
3
5
6
7
8
9
10
11
12
13
14
−14
−12
−10
−8
−6
−4
−2
−11
−9
−7

Figure 14

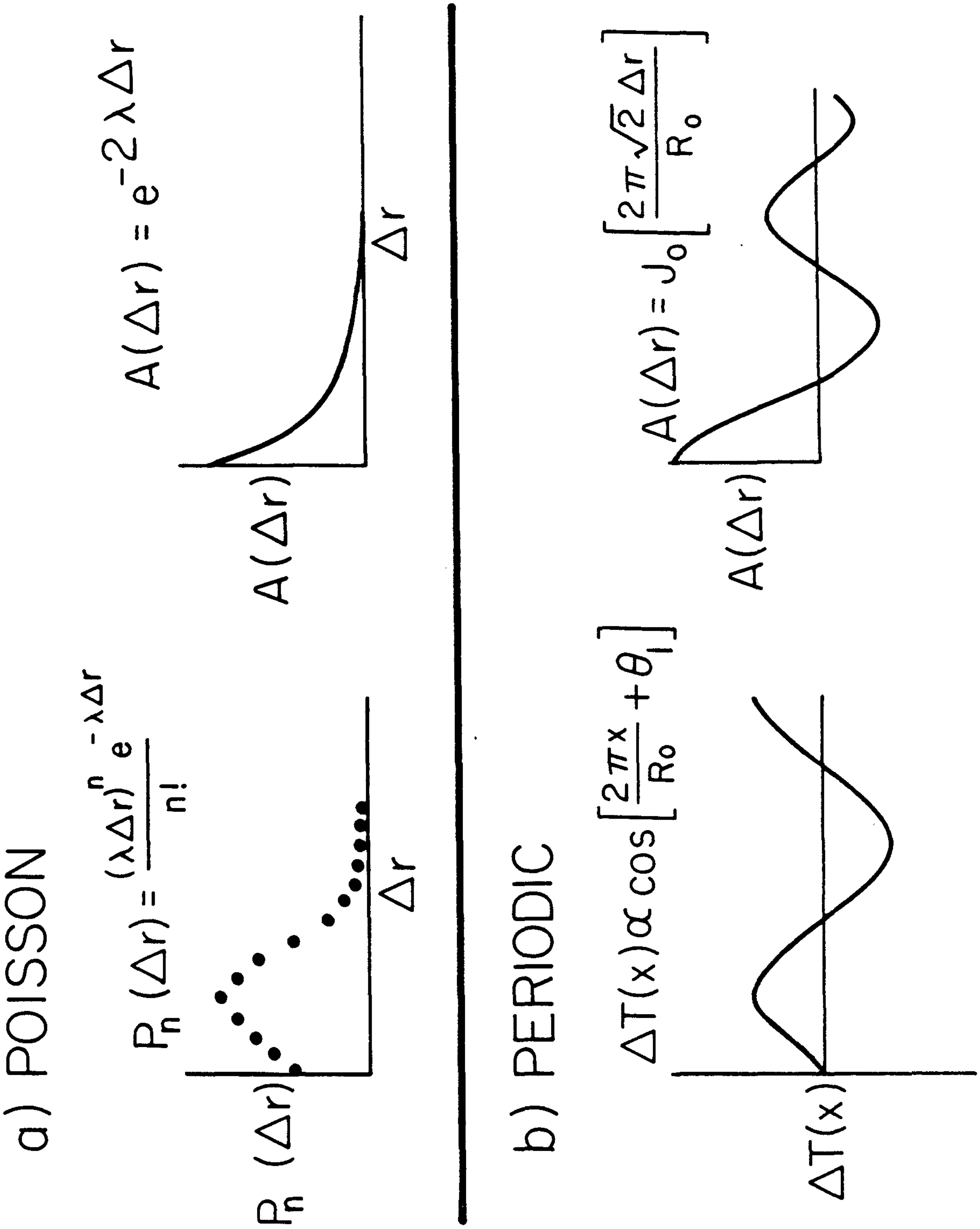
a) POISSON
$P_n(\Delta r) = \frac{(\lambda \Delta r)^n e^{-\lambda \Delta r}}{n!}$
$P_n(\Delta r)$
Δr
$A(\Delta r) = e^{-2\lambda \Delta r}$
$A(\Delta r)$
Δr
b) PERIODIC
$\Delta T(x) \propto \cos\left[\frac{2\pi x}{R_o} + \theta_1\right]$
$\Delta T(x)$
$A(\Delta r) = J_o\left[\frac{2\pi\sqrt{2}\,\Delta r}{R_o}\right]$
$A(\Delta r)$

Figure 15

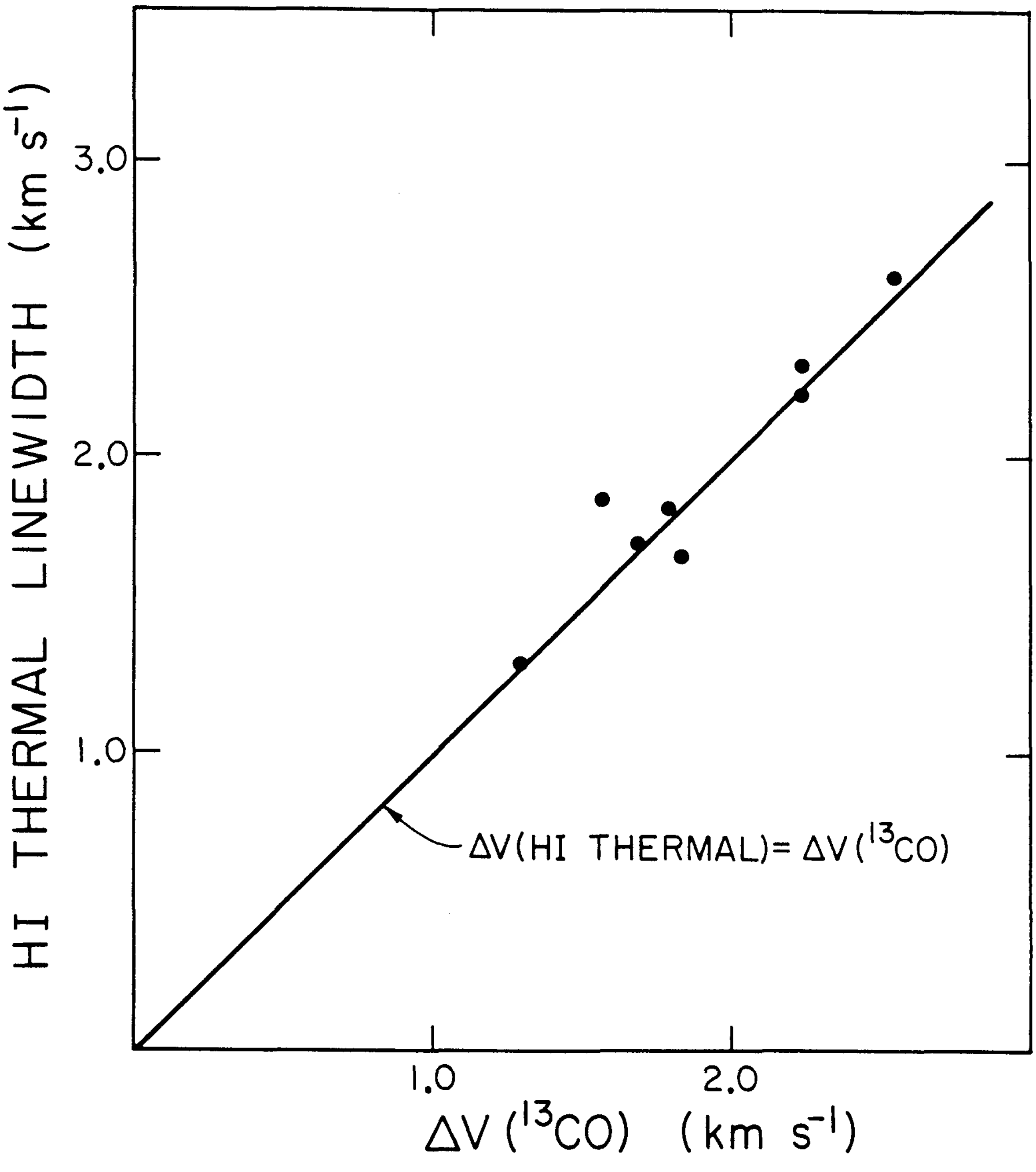
HI THERMAL LINEWIDTH (km s^{-1})
3.0
2.0
1.0
1.0
2.0
ΔV (^{13}CO) (km s^{-1})
ΔV(HI THERMAL)= ΔV(^{13}CO)

Figure 16

CHAPTER 5

VELOCITY FLUCTUATIONS AND TURBULENCE IN MOLECULAR CLOUDS

ABSTRACT

A study of supersonic turbulence in several molecular clouds has been made by examining the increase in velocity dispersion with spatial scale over a range of 0.04 to 40 pc. We find evidence for substantial energetic input at small scales. Although large-scale organized mass flows (such as collapse, expansion, or rotation) are clearly present, we argue that violent small-scale motions are more likely to be the dominant reason for the apparently widespread existence of supersonic turbulence in galactic molecular clouds.

We argue on observational and theoretical grounds that molecular cloud turbulence is dominated by shock dissipation and gas compression resulting from supersonic gas kinematics. The Kolmogoroff theory of a dissipationless energy cascade from larger to smaller scales which might be expected in an incompressible turbulent fluid with a high Reynolds number, is of doubtful relevance to interstellar conditions, although this theory has been favored recently in the literature.

High velocity mass outflow from young stellar objects can enduce cloud fragmentation and is a plausible source of energetic input originating at small scales which might be sufficient to balance turbulent energy dissipation in molecular clouds. Clumpiness in the ambient cloud material as well as in the outflowing matter is necessary for this mechanism to maintain internal cloud motions.

I. INTRODUCTION: THE THEORY OF INCOMPRESSIBLE TURBULENCE

The ground work for modern understanding of turbulence was laid by Taylor (1935), who proposed that turbulent motion in a fluid is a random process in which the velocity varies continuously and irregularly with position. Previously, turbulence had been thought of only in terms of collisions between many discrete elements. Two later papers (Taylor 1938a, 1938b) further explored continuous random functions in the study of fluid dynamics and introduced the concept of correlation between velocities at two points, stressing the importance of this correlation in describing the turbulence. Taylor also showed that the Fourier transform of the velocity correlation gives the turbulent energy spectrum and describes the distribution of energy over different wave numbers (corresponding to different spatial scales).

Kolmogoroff (1941) introduced similarity arguments which are still the basis for the classical theory of incompressible turbulence. The ratio of the inertial and viscosity terms in the Navier-Stokes equation of motion in a viscous fluid, is roughly equal to a quantity defined as the Reynolds number:

$$R_\lambda = (v_\lambda)\lambda/(\eta/\rho),$$

where λ is the length scale under consideration, v_λ is the variation in velocity associated with this scale, and η/ρ is the kinematic viscosity. Fully developed turbulence occurs over spatial scales smaller than the overall size L of the region but larger than the scale λ_d for which R_{λ_d} ~ unity (Landau and Lifshitz 1959). At large Reynolds numbers, fully developed turbulence is characterized by irregular variations of fluid velocity with space and time. Large eddies produce smaller and smaller eddies through inertial interaction and energy is thus transferred with little dissipation from large to small scales. At the scale λ_d, energy is finally dissipated. The critical value, R_{λ_d}, generally depends on the geometry of the flow.

An elementary calculation shows that for conditions in molecular clouds, the Reynolds number is large. Using the simple formula for viscosity derived by Reif (1965), we find that in dense clouds composed mainly of H_2,

$$R_\lambda \sim 6 \times 10^5 (v/1 \text{ km s}^{-1})(\lambda/0.1 \text{ pc})(n/1000 \text{ cm}^{-3})(T/20 \text{ K})^{-1/2}.$$

Other methods of computing R_λ give even higher values (Myers 1983); in general the interstellar medium is expected to be turbulent (Von Weizacker 1951; Kaplan and Pikelner 1970). Kaplan and Pikelner have also pointed out that somewhat smaller values of R_λ are expected if magnetic viscous effects dominate over those of kinematic viscosity, but even in this "worst case," $R \simeq 300$.

Kolmogoroff (1941) proposed that due to the nearly dissipationless inertial transfer of energy between eddies of different wave numbers, the turbulent elements exist in a universal statistical equilibrium determined by two boundary conditions:

1) viscosity of the fluid, and 2) the largest-scale structures present in the fluid. The energy is ultimately dissipated in the smallest eddies of size ~ λ_d and must be replenished by a source of turbulence at the rate ε. The famous Kolmogoroff cube-root relation for incompressible turbulence can be derived from a simple dimensional analysis (cf. Landau and Lifshitz 1959):

$$v_\lambda \sim (\varepsilon\lambda)^{1/3}, \text{ for } \lambda_d < \lambda < L.$$

The turbulent spectrum, F(k), is related to the velocity variation, v_λ, at wavelength λ (= $2\pi/k$), by the following expression:

$$v_\lambda{}^2 = \int_k^\infty F(k)dk,$$

so $v_\lambda \sim \lambda^{1/3}$ implies $F(k) \sim k^{-5/3}$.

The Kolmogoroff law is not necessarily applicable for supersonic velocity fields since the assumption of incompressibility is intrinsic to its derivation. There are two differing points of view in the literature: based on comparisons of cloud size and overall cloud velocity dispersion in various molecular lines taken from published works, Larson (1981) argues that in the interstellar medium, $v_\lambda \sim \lambda^{0.38}$ and attributes this to a Kolmogoroff law modified slightly by compressibility. Fleck (1980, 1981), Fleck and Clark (1981), Bash et al. (1981), and Leung et al. (1982) have also attributed supersonic motions in molecular clouds to the Kolmogoroff law originally formulated for incompressible turbulence. On the other hand, Scalo and Pumphrey (1982) have challenged the applicability of the Kolmogoroff dissipationless energy cascade to interstellar matter, claiming that interstellar clouds are comprised of clumps which interact for the most part through dissipative collisions. Myers (1983) has discussed subsonic turbulence in small, dense, cloud cores, but concluded that it is unclear whether there is an energy cascade as in Kolgomoroff turbulence.

The above contrasting views lead to radically different pictures of what constitutes a molecular cloud. It is important to distinguish between them, since a basic understanding of physical conditions in molecular clouds will be required before the process of star formation, which occurs deep within these clouds and depends on velocity fields, is understood. Furthermore, the common use of "microturbulent" and "large-velocity gradient" radiative transfer models -- which are basic tools for deducing temperature, density, and molecular abundances -- is invalid unless the internal velocity fields meet certain conditions. And finally, the study of molecular cloud internal kinematics provides a unique opportunity to study the phenomenon of supersonic turbulence, which is very difficult to study in a laboratory, especially over a dynamic wavelength range of three orders of magnitude.

In this paper, we shall use the 2.7mm data and sources of Chapter 4 to study kinematics on internal molecular cloud scales, with the intent of specifically addressing the problem of the origin and maintenance of supersonic motions. The techniques and basic results are described in §II. Previous studies by Larson (1981) and others are discussed in §III., in which we compare their analytic methods to those employed here. In §IV. we analyze our data and test the applicability of the Kolmogoroff theory to conditions in molecular clouds. §V. is a broader discussion of the implications of this study, and in §VI. we summarize our conclusions.

II. RESULTS: VELOCITY STRUCTURE FUNCTIONS

The ^{13}CO data described in Chapter 4 were used to compute the structure function for each source. The structure function (Kaplan 1966) can be defined as

$$S(\lambda) = \langle [v(\underset{\sim}{r}) - v(\underset{\sim}{r}')]^2 \rangle^{1/2},$$

where the average is taken over all position pairs $(\underset{\sim}{r}, \underset{\sim}{r}')$ separated by distance λ on the sky. $S(\lambda)$ is a root-mean-square measure of velocity dispersion for wavelength λ. Note that only the radial component of velocity is available from the molecular spectra used to calculate $S(\lambda)$.

The resolution of the spectrometer and the data noise level determine the accuracy with which $v(\underset{\sim}{r})$ and $S(\lambda)$ can be computed. The NRAO filter bank spectrometer yielded 100 kHz (0.27 km s^{-1}) resolution. The OVRO acousto-optic spectrometer contains 1024 pixels at 100 kHz spacings, with an effective resolution of about 200 kHz

(0.54 km s^{-1}). The Columbia spectrometer (used for Orion data only) was a filter bank with 250 kHz (0.68 km s^{-1}) resolution. However, several factors permit a much more exact determination of $v(\underset{\sim}{r})$: with the OVRO and Kitt Peak data, 1) each spectral line extends across many (20 to 30) channels; 2) the spectral profiles are fairly symmetrical; 3) the signal/noise ratio is very high, 50-100 in the line core; and 4) the structure function $S(\lambda)$ is computed as an average of typically more than 200 terms of the form $[v(\underset{\sim}{r}) - v(\underset{\sim}{r}')]$ for each λ.

The velocity centroid, v, of each profile was determined by a computer program which iteratively searched over a range initially three times the range used in the final computation. An initial guess was provided by the user and the results of one iteration provided the starting point for the next iteration, which in turn was carried out over a smaller velocity range so as to zero in on the correct line center. The velocity centroid was calculated as

$$v = \frac{\sum_i v_i T_i}{\sum_i T_i} ,$$

where the subscript i refers to the ith channel. The iterative procedure was stopped when the signal/noise ratio in the weakest intensity line channel was 10. This typically occurred at 1-2 times the half-power distance from line core, e.g. the inner 75-98% of integrated line power was used to determine the velocity centroid. The extreme line wings, which are frequently asymmetric, are relatively more noisy, and may reflect gas motions which involve only a very small percentage of the overall cloud mass (such as bipolar outflows; see Chapters 1 and 2, and Bally and Lada 1983), were not used to determine v.

Formal uncertainties in v were estimated from the following expression:

$$\sigma_v^2 = \sum_i \sigma_T^2 (\partial v / \partial T_i)^2,$$

with appropriate corrections for the slight overlap of adjacent spectrometer channels. The noise level, σ_T, was about 0.05-0.1 K at OVRO, while the Kitt Peak and Columbia data noise levels were about 0.2 K. The formal uncertainty in the quantity (v - v') was computed for each source and in general was 0.02-0.05 km s^{-1} for the OVRO and Kitt Peak data, and 0.15 km s^{-1} for the Columbia data, depending on the strength and width of the spectral lines.

An empirical check on the consistency of this method of measuring velocity centroids was made by observing the central position of each source about 60 times over the ~ one week duration of each observing run at OVRO and Kitt Peak. These separate velocity measurements are roughly Gaussian distributed about their means, with standard deviations of 0.04 km s^{-1}, 0.03 km s^{-1}, and 0.02 km s^{-1} for S140, Taurus, and NGC 2071 respectively, which agree with the formal uncertainties quoted above.

The structure functions, $S(\lambda)$, are plotted in Figure 1 for each source as solid filled circles. One would expect $S(\lambda)$ uncertainties to be considerably less than σ_{v-v}, since $S(\lambda)$ is an average of many such terms. Qualitatively, none of the $S(\lambda)$ functions in Figure 1 appear to be significantly corrupted by profile noise down to the lowest levels plotted, about 0.08 km s^{-1} (in L1534) for the OVRO/Kitt Peak data, and 1 km s^{-1} for the Columbia Orion data. It is more likely that the major contribution to irregularities in $S(\lambda)$ is the inherent anisotropy or inhomogeneity of ^{13}CO in the molecular clouds. In principle, each value of $S(\lambda)$ should be corrected for noise by quadratic subtraction of the dispersion due to noise, but since this correction at most amounts to only a few percent change in $S(\lambda)$, we have ignored it.

In all five sources, the velocity dispersion increases with λ. The data were fitted via least-squares to equations of the form

$$\log S(\lambda) = \log a + b \log \lambda.$$

Table 1 shows the results of this procedure and lists the ranges over which the fitted values of a and b are valid, as well as their uncertainties. The fitted structure functions, $S(\lambda) = a\lambda^b$, are also plotted in Figure 1 as solid lines.

III. PREVIOUS STUDIES

Structure functions have been utilized by Munch (1958) in a study of ionized gas motions in Orion, by Kaplan (1958) in studies of radial velocities of interstellar clouds, and by Serkowski (1958) in a statistical analysis of polarization and reddening of the Double Cluster in Perseus. Kaplan (1966) has pointed out that not only velocity fluctuations, but also fluctuations of brightness, of magnetic field strengths, of radio emission intensity, or of other physically meaningful quantities which are linked to the velocity field, are appropriate for analysis with structure functions.

Several observational studies have been made of <u>molecular</u> clouds to determine the dependence of v_λ on λ. Using data previously published in the literature, Larson (1981) found an empirical relationship of the form,

$$\Delta v \sim L^{0.4}$$

over a range of cloud sizes from 0.1 to 100 pc in 56 sources. Leung et al. (1982), from a total of 16 isolated dark globules, found

$$\begin{aligned} v_{turb} &\sim L^{0.48} \quad \text{(all 16 sources)} \\ &\sim L^{0.55} \quad (\text{4 sources, } T_k < 10\text{ K}) \\ &\sim L^{0.31} \quad (\text{12 sources, } T_k > 10\text{ K}). \end{aligned}$$

Given the small sample of Leung et al., consisting only of dark globules, there is some question as to the applicability of that study to other types of molecular clouds. Both Larson (1981) and Leung et al. (1982) have interpreted their data as evidence for a Kolmogoroff turbulent spectrum, attributing the slightly steeper than 1/3 power law dependence of line width on scale size to some additional energy dissipation at large scales by shocks. A recent paper by Myers (1983) examines the dependence of Δv on source size for small, dense cores in dark clouds, but discusses primarily <u>subsonic</u> turbulence, concluding that it is uncertain whether the Kolmogoroff law applies.

A closer examination of the data of Larson (1981) and of Leung et al. (1982) leads to difficulties in comparing their results, since in each study, the line width and the cloud size are interpreted differently. Larson's data consists of previously published maps of many different molecular species (^{13}CO, H_2CO, NH_3, OH, HC_3N, HC_5N, SO, HCO^+, H I, and ^{12}CO) whose widely varying excitation requirements and possibly varying distributions or abundances may affect the reliability of his results. Leung et al. used a more homogeneous set of CO observations, albeit a much smaller sample. In principle, it is rather unusual to invoke the Kolmogoroff relation to explain the observed variation of line width with cloud size since derivation of the Kolmogoroff velocity-scale size 1/3 power law requires incompressibility, a condition which is strongly violated in all observed molecular and atomic clouds. The effects of strong density and temperature variations in the earth's atmosphere, for example, are seen as large deviations from the Kolmogoroff spectrum (Vinnichenko et al. 1973; Scalo 1983). There are other more reasonable explanations for the observed increase of line width with cloud size. If all molecular clouds were dominated by large scale motions (collapse, expansion, or rotation), the projected cloud Δv might increase with cloud size as has been observed, especially for clouds which are centrally condensed (Pumphrey and Scalo 1983; Myers et al. 1978). Furthermore, larger clouds are expected to have a longer line-of-sight, and presumably a greater number of fragments in that line-of-sight. Clearly then, larger clouds have a greater chance of containing one or more of the rarer high velocity fragments, and the line width is expected to increase roughly as the square root of the cloud dimensions, similar to the observed relation (Scalo 1983). Such a relation is not necessarily evidence for Kolgomoroff turbulence, and in fact may have little bearing on the detailed physical processes directly causing velocity fluctuations. Even in dense cloud cores where velocities are subsonic, the applicability of the Kolgomoroff law has been questioned because of the incompressibility condition; in those sources, the Δv-source size relation might be explained simply by the tendency for clouds to be in virial equilibrium with a density $n \propto R^{-1}$ (Myers 1983).

Fully developed turbulence at large Reynolds numbers has highly irregular velocity variations from point to point, resulting in complex fluid particle paths and extensive mixing of the fluid (Landau and Lifshitz 1959). In a turbulent fluid, velocities and positions of the particles vary in such a random and complicated way that initial conditions and past history cannot be determined. These requirements seem inappropriate for isolated molecular clouds scattered throughout the Galaxy, since the Milky Way has a highly defined spiral spatial pattern with a unique rotational pattern. It is difficult to justify the hypothesis that the velocity dispersion in an isolated molecular cloud is directly related to conditions in other isolated clouds in other parts of the Galaxy, especially since astronomers do not even agree on whether molecular clouds survive long enough to pass from one spiral arm to another. Casoli and Combes (1982) have carried out numerical simulations for giant molecular cloud kinematics and have concluded that molecular clouds moving in the galactic potential never reach a collisional steady state as an ensemble and cannot be considered as a fluid. Therefore, we restrict our analysis to small-scale turbulence internal to molecular clouds; on galactic scales, gas motions are dominated by the rotation and structure of the Milky Way.

In summary, recent assertions that a Kolgomoroff-type turbulent energy cascade dominates molecular cloud kinematics have theoretical difficulties and seem to be motivated by somewhat inconclusive line width-source size studies. Comparison of gas velocities and velocity dispersions from position to position <u>within</u> isolated molecular clouds is necessary to determine the characteristics of the turbulence. In this paper, we have accomplished this by computing structure functions for several representative clouds. The structure functions can also be used to determine whether small-scale turbulence or larger-scale velocity flows determine molecular cloud line widths, a long debated question in radio astronomy. For example, in the case of symmetrical cloud collapse or expansion, the structure function will be flat and near-zero over a wide range of spatial scales; however, turbulent disordered motions will produce structure functions whose shape and slope provide clues as to the nature of the energy source.

IV. ANALYSIS OF STRUCTURE FUNCTIONS

The geometry corresponding to observations of an optically thin line towards a molecular cloud is depicted in Figure 2. Two observing positions separated by distance λ projected on the sky are sampled with an antenna of beamwidth Θ_B. Ideally, the structure function is determined by measuring the velocity difference and distance between the material at positions X and Y; in practice, the velocities obtained are actually averages along two nearly parallel columns, A and B, sampled through the cloud by the observation of unsaturated lines.

If $v_\lambda \sim a\lambda^b$, the observed structure function, $S(\lambda)$, will be considerably less than $a\lambda^b$ for an optically thin line, as has been shown by Von Hoerner (1951), Munch (1958), and Kaplan and Klimishin (1964). Let v_A be the observed velocity centroid along column A, and v_B the observed velocity centroid along column B. Then

$$v_A = \int e^{-ks} v_A(s) k ds,$$

$$v_B = \int e^{-ks} v_B(s) k ds,$$

where k is the absorption coefficient. The observed structure function (cf. Munch 1958) is given by

$$[S(\lambda)]^2 = \langle (v_A - v_B)^2 \rangle$$

$$= k^2 \iint e^{-k(s_1+s_2)} \langle v_A(s_1)v_A(s_2)+v_B(s_1)v_B(s_2)-2v_A(s_1)v_B(s_2)\rangle ds_1 ds_2$$

$$= k^2 \iint e^{-k(s_1+s_2)} \langle [v_A(s_1)-v_B(s_2)]^2 - [v_A(s_1)-v_A(s_2)]^2 \rangle ds_1 ds_2 .$$

Munch (1958) and Von Hoerner (1951) identify the first term in brackets as relating velocities in the two columns, A and B, and the second term in brackets is a measure of the velocity dispersion along a single column. These authors also show that if the turbulence has the following form,

$$\langle [v(\underset{\sim}{r}_1)-v(\underset{\sim}{r}_2)]^2 \rangle^{1/2} = C|\underset{\sim}{r}_1-\underset{\sim}{r}_2|^b ,$$

$$C = \text{constant},$$

then we can substitute $t = k|s_1-s_2|$ and simplify the integration above to the following form:

$$[S(\lambda)]^2 = C^2 k^{-2b} \int \Big[[(t^2 + (k\lambda)^2]^b - t^{2b} \Big] e^{-t} dt .$$

This integral can be numerically tabulated (Von Hoerner 1951) and we find:

$$S(\lambda) = C\, \lambda^b\, H(\lambda).$$

The slowly varying function $H(\lambda) \rightarrow 1$ as $k\lambda \rightarrow \infty$, and $H(\lambda) \rightarrow \text{const} \times (k\lambda)^{1/2}$ as $k\lambda \rightarrow 0$. Thus for separations λ much greater than a photon mean free path, $S(\lambda) \simeq v_\lambda \sim \lambda^b$, but for separations over which ^{13}CO would be optically thin, $S(\lambda) < v_\lambda$ and $S(\lambda) \sim \lambda^{(b + 1/2)}$. We thus have a fairly sensitive test for the Kolmogoroff law; $S(\lambda) \sim \lambda^{1/3}$ $(k\lambda > 1)$ or $S(\lambda) \sim \lambda^{5/6}$ $(k\lambda < 1)$.

The distance λ' corresponding to $k\lambda = 1$ for the ^{13}CO line is readily calculated using formulae from Spitzer (1978). We assume that the $^{13}CO/H_2$ abundance ratio is 8.3×10^{-7}:

$$\lambda' \simeq k^{-1} = \frac{(\Delta v_{FWHM}/2 \text{ km s}^{-1})(T/20 \text{ K})}{(n_{H_2}/2000 \text{ cm}^{-3})\ 4(1 - e^{-5.29/T})} \times 8.2 \text{ pc}.$$

Values of λ' for the sources observed in this study are listed in Table 1 along with predicted values, b', for the indices which should have fit the ^{13}CO observations if the true value of b were 1/3. These expected values, b', were computed from the expressions above, using numerically determined values of $H(\lambda)$. Using our estimates of λ' for each source, we have plotted in Figure 1 (dashed lines) the expected form of $S(\lambda)$ based on the Kolmogoroff law of classical turbulence.

In the derivation of $H(\lambda)$ above, we have proceeded as if k, the absorption coefficient, were essentially the same towards different cloud positions. Since k depends on temperature, density, and the velocity field, one might expect some scatter in $S(\lambda)$ if there were large deviations of k from its average value. We minimized this effect in our data by mapping for the structure function in cloud regions where the ^{13}CO emission was fairly homogeneous. The greatest inhomogeneities are in Orion and S140 at $\lambda > 8$ pc. Note that although k is expected to vary more at large λ (large separation of A and B), as λ becomes larger, $H(\lambda)$ becomes more independent of k; the strongest dependence of $H(\lambda)$ on k occurs for small λ, where $H(\lambda)$ is proportional to $(k\lambda)^{1/2}$, but k will vary minimally between two close line-of-sights.

At scales of several pc or less, corrresponding to <u>internal</u> cloud scales, the observed structure functions, $S(\lambda)$, are all less steep in (logarithmic) slope than predicted by the Kolmogoroff law. Furthermore, the observed slopes, b, do not vary with λ; if Kolmogoroff turbulence were present, a significant change in b should occur at the scale λ', corresponding to the distance over which ^{13}CO emission is radiatively decoupled. In Orion, our observations show a change in slope of +0.02 ($\pm$0.03) from $\lambda = 0.15$ pc to $\lambda = 40$ pc; the Kolmogoroff law predicts a change of −0.4 . Overall (volume-averaged) densities of 10^6–10^7 cm^{-3} might bring the Kolmogoroff turbulent models (dashed lines, Figure 1) into better agreement with our data for L1529, L1534, and S140 (Orion would not improve), but then the ^{13}CO opacity would be 100–1000, three orders of magnitude higher than is indicated by observations, and HC_3N 3mm emission would be widespread and strong throughout these sources -- also in disagreement with observations presented in Chapter 4.

Although velocity dispersion does, in general, increase with spatial scale, it does not do so in a way consistent with a simple transfer of turbulent energy from large to small scales. Hierarchies of turbulent eddies have been suggested in the literature (Fleck 1981; Bash et al. 1981; Larson 1981; Leung et al. 1982) to be responsible for the observation that Δv increases with cloud size. We find serious problems with that interpretation based on our observations of internal velocity structure in both warm and dark molecular clouds. The fact that the observed structure function index, b, is fairly constant in a given source over a wide range of λ, is indicative of substantial energetic <u>input</u> at small spatial scales. An extreme example of this is shown in the upper left corner of Figure 1, where $S(\lambda)$ from optical O II and Hγ data from ionized gas in Orion (Munch 1958) are plotted. Munch (1958) noted that the slope of the optical data was much lower than the 5/6 value expected from optically thin gas described by $v_\lambda \sim \lambda^{1/3}$. Figure 1 shows that velocity dispersions at $\lambda \lesssim 1$ pc are too high relative to those at $\lambda \sim 10$–100 pc for inertial transfer of turbulent energy from large to small scales to be occurring. Furthermore, observed values of b vary by more than a factor of two from source to source (Table 1); this casts more doubt on the hypothesis that all molecular clouds are part of a common hierarchy of turbulent eddies.

V. DISCUSSION

The basis for Kolmogoroff's (1941) pioneering work on incompressible turbulence was that the universal statistical equilibrium in which there is a dissipationless energy cascade from large to small scales is determined by two boundary conditions: 1) viscosity of the fluid, and 2) the size of the largest-scale structures present (see §I.). The presence of supersonic gas motions, shocks, and shock dissipation, however, brings in additional important parameters, such as the energy dissipation mechanisms, the cause of the shocks, their particular spatial orientation and geometry, and additional boundary conditions at the shocks themselves. The condition of incompressibility is grossly violated in molecular clouds; for example, as shown in Chapter 4, CO and HC_3N emission were detected towards the same molecular regions at the same LSR velocities, indicative of densities of 10^3 and 10^6 cm^{-3} present in the same general vicinity. Gas compression and shocks must be present in molecular clouds because observations show molecular gas velocities present with Mach numbers of ~ 5-10 (see Table 3, Chapter 4, for CO line widths) to up to well over 100 [Lichten 1982a, 1982b (Chapters 1 and 2); Bally and Lada 1983]. Observations showing the most direct evidence for very energetic shocks in molecular clouds are those of the H_2 infrared lines (Chernoff et al. 1982; Bally and Lane 1982; Simon and Joyce 1983), which have been detected near regions of mass outflows from early-type stars.

In the absence of some other known mechanism which might produce substantial energetic input at small spatial scales in molecular clouds, we shall consider the effects of energetic activity associated with young stellar objects on the surrounding ambient molecular gas. Can origination and maintenance of supersonic turbulence in molecular clouds be attributed to episodes of violent mass loss from young stars? Although we cannot definitively answer this question, we shall endeavor to place reasonable constraints on the physical conditions which determine the effectiveness of this mechanism, and shall suggest how some of the uncertainties could be resolved. An alternative model, in which galactic rotational shear transmits turbulent energy from large (galactic) scales to small (internal molecular cloud) scales, was discussed as potentially relevant in Chapter 4. However, our structure function results in this paper now seem to indicate that internal molecular cloud turbulent velocities are too high to have been derived from an energy cascade from large to small scales.

Most high velocity molecular outflows appear to be loosely collimated bipolar events involving masses of 0.1-100 M_o with velocities of 10-50 km s^{-1}, over distances of ~ 0.4 pc (Bally and Lada 1983). More than 50 such outflows have now been detected as broad wing or high velocity plateau CO sources. The reason for common bipolar appearence of these objects is not well understood; collimation may occur at a stellar surface or from geometric constraints of the surrounding molecular gas (see discussion in Schwartz et al. 1983). Unless the extinctions to the central sources are unusually high, radiatively driven stellar winds can be ruled out in nearly all known cases (Bally and Lada 1983); the actual outflow mechanism is not known.

The preliminary statistics of bipolar outflow sources show that their local formation rate is, in the lower limit, comparable to all stars of spectral type A0 and earlier. Furthermore, many bipolar molecular sources are associated with Herbig-Haro objects, young B stars, and low luminosity objects [Bally and Lada 1983; see also Lichten 1982b (Chapter 2) and references therein], and the phenomenon seems to take place with stars of many different spectral types (Calvet et al. 1983). The dynamical timescales inferred from observed velocities and spatial extents range from 10^3 to 10^5 years.

Perhaps the most comprehensive theoretical analysis of stellar winds driving molecular cloud turbulence is that of Norman and Silk (1980). Although they discussed only spherically symmetric outflows from T-Tauri stars in dark molecular clouds, in principle the same mechanisms could be relevant to physical conditions in warm clouds. Bipolar outflow configurations have been discussed theoretically by Barral and Canto (1981). Their model has two ovoid cavities symmetric with respect to a collimating disk, and an outer shell in which compressed material shocked by the stellar wind moves towards the extreme tips. There is observational evidence cited by Barral and Canto (1981) in support of their model. A similar model is presented by Canto et al. (1981) to explain CO observations of bipolar mass outflow in R Mon, NGC 2261, and HH 39.

Comparisons of different molecular transitions observed directly from material in the outflows show that the molecular gas in the compressed, outflowing shell is probably much denser than the surrounding ambient material and is highly clumped (see Chapter 4, §VI.; also Plambeck et al. 1983). Konigl (1982) has discussed several causes for clumpiness in the dense, outflowing shell. Possibilities include tearing off of fragments in the outflow by the Kelvin-Helmholtz instability, formation of condensations due to thermal instabilities, or simply that the initial conditions in the ambient cloud are clumpy.

Figure 3 qualitatively shows various degrees of fragmentation in molecular clouds and a possible connection to energetic stellar outflows; it is based largely on the autocorrelation results of Chapter 4. A giant cloud complex (such as Orion) is shown schematically in Figure 3a, with an overall size of 75 pc. In Chapter 4, we showed that large-scale mapping of the Orion complex in ^{13}CO reveals a collection of smaller clouds of size ~ 10 pc. The 10 pc clouds could be rotating and/or contracting; if they begin to collapse gravitationally, however, they will fragment according to the Jeans criterion (Hunter 1962), where the fragment size is approximately

$$\lambda_J = 2\pi/k_J = [\gamma\pi kT/\mu G\rho]^{1/2} = 1.5\ (T/25\ K)^{1/2}(n/1000\ cm^{-3})^{-1/2}\ pc.$$

In this expression, k_J = wavenumber for unstable perturbations, k = Boltzmann's constant, T = temperature, γ = ratio of specific heats

(7/5 for a diatomic molecular gas), μ = mean molecular weight ($=2m_H$), G = gravitational constant, and ρ is the mass density. Indeed, in Chapter 4, correlation lengths of several pc were found from the larger ^{13}CO maps (of several 10 pc size regions). In Figure 3b, these smaller cloud sections are shown.

The next level of fragmentation is sketched in Figures 3c,d where we illustrate a means by which energetic outflows from many embedded young stellar objects can further break apart and compress portions of the molecular cloud. Note that these outflows can not only induce cloud clumpiness, but can also cause the dense fragments to move with relative velocities well in excess of their thermal or sound speeds.

It is difficult to detect the cavities thought to result from bipolar outflows, since the expected decrease in column density in the direction of such cavities might be masked by the increase in cloud density often found towards regions of star formation where these objects are located. In Figure 4, we show a strip map of ^{13}CO and C^{18}O integrated intensity across the powerful NGC 2071 bipolar outflow source. The decrease at the bipolar source position is consistent with a cavity, as was expected from theory. NH_3 maps by Schwartz et al. (1983) are also consistent with the existence of cavities "hollowed out" by powerful bipolar outflow sources in several molecular clouds.

When dense, small clumps in a high velocity outflow collide with parts of the ambient molecular cloud, shock fronts are immediately established due to the highly supersonic velocities. Although stellar winds may be 10^2-10^3 km s^{-1}, the bulk of the outflowing molecular material plows through the cloud in a dense, clumpy shell at speeds of 10-30 km s^{-1}. In this molecular gas, the post-shock temperature is $5300(v_{sh}/10 \text{ km s}^{-1})^2$ K (McKee and Hollenback 1980). Cooling via H_2 vibrational-rotational quadrupole transitions is very efficient, and the temperature drops to about 500 K in 10 years for $n \sim 10^3$ cm^{-3} (Shull and Hollenbach 1978; note that H_2 dissociation may be important for higher velocity shocks). Cooling from CO rotational transitions is effective once the temperature reaches a few hundred degrees, and the cooling time is 10^2-10^3 years at temperatures between 200 and 10 K (Gilden 1982). The expectation that molecular material in this portion of the high velocity outflow is rapidly cooled to ambient cloud temperatures is supported by recent observations by Plambeck et al. (1983), and by Loren et al. (1981), whose calculated excitation temperatures in 8 high velocity sources range from 7 to 18 K.

If both the ambient molecular cloud and the outflowing high-velocity material are clumped, fragment collisional interactions are likely to play a major role in the energetics. Cloud fragment collisions, subsequent energy dissipation, and conversion to turbulent energy have been analyzed in much detail by Bash et al. (1981), although in a slightly different context. We shall draw upon their results in the following discussion. As outflowing fragments and cloud fragments collide, most of the center of mass energy may be radiated away if we assume inelastic collisions and isothermal shocks, but momentum conservation will carry these fragments further into the molecular cloud where the remaining energy is further dissipated and eventually converted into turbulent random motions. Estimates of the fraction of a clump's kinetic energy dissipated in the time needed for it to move its own diameter range from 5 to 20% (Scalo and Pumphrey 1982; Bash et al. 1981).

For overall energy balance in the molecular cloud, turbulent dissipation must be balanced by stellar high velocity outflow energetic input:

$$\frac{n_3 V_t^3}{(\xi/20)(\lambda_{18})} \leq \frac{(e/0.1)[n_{hvo}/0.001\ \mathrm{pc}^{-3}](M_{hvo})(V_{hvo,25})^2}{\tau_4},$$

where n_3 is the cloud average density in units of 10^3 cm^{-3}, V_t is the cloud turbulent velocity in km s^{-1}, λ_{18} is the turbulent scale, or typical eddy size in units of 10^{18} cm, M_{hvo} and $V_{hvo,25}$ are the mass and velocity in a typical high velocity outflow in units of M_0 and 25 km s^{-1}, and τ_4 is the lifetime of the typical HVO in units of 10^4 years. In the above expression, ξ is a factor of about 20 which accounts for a slower dissipation rate for supersonic turbulence in a clumped medium, based on N-body simulation results of Scalo and Pumphrey (1982), and e is the efficiency of conversion from outflowing molecular clump energy to turbulent cloud energy. The value of 0.1 results from equating the original and final outflow momenta; the "final" outflow occurs when the velocity has decreased to the cloud turbulent velocity. Thus $e \sim V_t/V_{hvo} \sim 0.1$ [Lada and Gautier (1982) and Solomon et al. (1981) also estimate $e \sim 0.1$].

The quantities ξ, e, and n_{hvo} are the most uncertain in the expression above, and their values are critical to the viability of stellar outflows as a mechanism to maintain turbulence. The factor ξ is best determined by numerical modeling, but depends somewhat on the initial conditions assumed in the model. The efficiency e depends on local processes at the high velocity outflow molecular shock front which plows through the ambient cloud. These processes are poorly understood now because of the difficulty of making sensitive, high-resolution observations of broad wing sources in mm and infrared molecular lines. And finally, n_{hvo} is also uncertain, although as instrumental sensitivity improves, more and more high velocity outflows are being discovered. The value input above was chosen simply to balance the equation; if about 1% of a young stellar object's lifetime is spent in this mass loss phase, we expect the overall space density of young stellar objects to be ~ 0.1 pc^{-3}, corresponding to about 50 young stellar objects in a 10 pc molecular cloud. One might conclude from this that <u>low-mass</u> stars will be very important in this scenario, since they would be sufficiently numerous to provide the required reservoir of energy available to power cloud turbulence. As a point of comparison, the space density of T-Tauri stars in the Taurus-Auriga dark cloud complex is ~ 10 pc^{-3} (Cohen and Kuhi 1979). Beckwith et al. (1983) have reviewed the statistics of energetic outflow sources within 1 kpc of the sun, and conclude that low-mass stars are responsible for most of these energetic outflows in molecular clouds. Although the molecular mass in a high velocity flow may be on the order of 1 $M_{\odot}$, the amount of mass lost from the star itself is much less, since the stellar wind velocities can be 10-100 times higher than the velocity of the shock which it sets up in the molecular cloud. Note that most of the numerous "weak" molecular outflows detected near low-mass objects (Frerking and Langer 1982; Lichten 1982b; Edwards and Snell 1982,1983; Bally and Lada 1983; Rodriguez et al. 1982) are considerably closer to the sun than the stronger ones similar to Orion or NGC 2071; a majority are in nearby nebulae such as Taurus (D=140 pc). If these weaker outflow sources were at Orion's distance (500 pc) or at S140's distance (910 pc), many would not be detectable with current instrumentation. The current count of less powerful outflow sources probably greatly underestimates the true number.

Even if embedded stars can maintain internal molecular cloud turbulence, it is not clear whether stellar outflows could initiate turbulence before the cloud collapses from gravity. The gravitational free-fall time for a cloud is (Spitzer 1978)

$$\tau_{ff} = [3\pi/(32G\rho)]^{1/2} = 2X10^{6}(n_{H_2}/300\ cm^{-3})^{-1/2}\ yrs.$$

τ_{ff} should be compared to the quantity $\tau_{hvo} = E_{turb}/(dE/dt)_{hvo}$, where E_{turb} is the total turbulent energy in a typical molecular cloud, and $(dE/dt)_{hvo}$ is the rate at which HVOs in that cloud can supply turbulent kinetic energy to the gas. τ_{hvo} is a measure of the timescale associated with <u>initiating</u> the turbulence from energetic stellar mass-loss activity. These two timescales may be comparable:

$$\tau_{hvo} = \frac{n_{300}(V_{t,1})^2 \; 2X10^6 \text{ yrs}}{M_{hvo}(n_{hvo}/0.001 \text{ pc}^{-3})(V_{hvo,25})^2(e/0.1)(\tau_4)^{-1}}.$$

n_{300} is the average cloud density in units of 300 cm^{-3}, the turbulent and high velocity outflow (HVO) velocities are in units of 1 and 25 km s^{-1}, M_{hvo} is the average mass involved per HVO event in units of M_o, and the other variables have been defined previously. Since $\tau_{ff} \sim \tau_{hvo}$, energetic stellar outflows <u>may</u> be capable of initiating the observed supersonic cloud turbulence before gravitational collapse occurs. However some additional energy input, e.g. conversion of gravitational energy into turbulent energy, might be required for some clouds, especially very dense ones. The presence of violent small-scale disturbances near stars inside a collapsing cloud would encourage the conversion of ordered gravitational motion to chaotic turbulent motions. This process of "turbulent virialization" has been discussed by Hoyle (1953), Odgers and Stewart (1958), Woolfson (1978), and Scalo and Pumphrey (1982), and is most effective in a clumped environment; unfortunately, it is extremely difficult to parametrize quantitatively and its importance in molecular clouds remains unknown. [Bally and Lada (1983) found $\tau_{ff} << \tau_{hvo}$, but they assumed that the energy input from high velocity outflows is proportional to the associated star's luminosity. Although the strongest outflows are generally found near more luminous stars, we do not believe that a well defined relation can be inferred from their data or from that of

Rodriguez et al. (1982), particularly in light of the paucity of observational data on stars with $L < 20\ L_0$. Most of the energy for turbulence would come from the low-mass stars since they are so much more numerous, so detection of more low-mass star high velocity outflows is critical to resolution of this question.]

Since clumpiness greatly enhances the efficacy of maintenance of turbulence by high velocity outflows (Scalo and Pumphrey 1983), a critical degree of inhomogeneity, or clumpiness, is necessary in a molecular cloud in order for clump-clump collisional interactions to dominate over the effects of drag and deceleration exerted on the cloud fragments by the diffuse, interclump material in which they are embedded. We require that the stopping distance due to this drag be greater than the total molecular cloud radius. We denote the fragment average internal density by n_f and the density of the diffuse, interclump gas by n_d. Let R_{cloud} by the total cloud radius and r_f the fragment average radius. For the stopping distance to be greater than R_{cloud} (Norman and Silk 1980),

$$\frac{4}{3}\,\frac{n_f}{n_d} > \frac{R_{cloud}}{r_f},$$

or

$$\frac{4}{3}\,\frac{r_f}{R_{cloud}} > F.$$

In this expression, $F = n_d/n_f$ is an estimate of the volume filling factor for the dense clumps if their total mass is comparable to the total mass of the diffuse material (Norman and Silk 1980). Thus we need F $\lesssim 0.1$. For $n_d \sim$ several hundred cm^{-3}, we expect that $n_f \sim 10^4$ cm^{-3}. The overall average density would be some intermediate value. Note that the filling factor for the dense clumps cannot be deduced directly from ^{13}CO data due to projection effects and ignorance of cloud geometry. The distance over which significant variations in density occur, however, can be estimated from autocorrelations of ^{13}CO intensity fluctuations across the source, cf. Chapter 4.

In summary, we find that initiation and maintenance of internal cloud turbulence by energetic outflows from young stars deserves serious consideration. The filling factor for dense clumps is a critical factor which is presently not well known. Carefully calibrated maps of molecules such as HC_3N might be a fruitful observational approach to this problem, since the HC_3N molecule has many transitions, each of which is excited over a characteristic density range. The difficulty of such an experiment would be that the high spectral and spatial resolution needed (less than 0.1 km s^{-1} and less than 0.1 pc) and the requirement that multiple transitions be observed mean that long integration times would have to be available on telescopes of different size (so that the beam size remains the same at different frequencies). Unfortunately, CO data are not particularly useful in determination of filling factors, since CO emission is detected from gas over a density range from several hundred to tens of thousands cm^{-3}, and does not distinguish easily between small, dense clumps and extended diffuse material. Once the filling factor is known, other uncertain parameters (ξ, e) in the turbulence energy balance equation can be better determined.

VI. CONCLUSIONS

We have precisely measured velocity fluctuations in several molecular clouds over spatial scales of 0.04-40 pc. Velocity dispersion increases with spatial scale but is substantially higher at small spatial scales than would be possible if internal cloud kinematics were dominated by a turbulent energy cascade from large to small scales, such as occurs in an incompressible turbulent fluid. Shocks, gas compression, and energy dissipation are expected to play important roles in internal cloud kinematics because of the supersonic motions of cloud fragments.

Energetic mass outflows at relatively small spatial scales from young stellar objects may be capable of sustaining internal turbulent cloud motions. This mechanism is fairly effective, however, provided that molecular clouds are sufficiently clumpy and fragmented and contain enough active young stellar objects. Clump filling factors, efficiency of conversion from outflow to turbulent energy, and local shock processes are critical parameters which must be better understood in order to evaluate the possibility that cloud turbulence is maintained by outflows from embedded stars. We expect that many of the observed -- and an even higher percentage of the as of yet unobserved -- energetic mass outflows are from low-mass stars. These stellar outflows may also play a substantial role in stabilizing molecular clouds against gravitational collapse, but more observational data on low-mass outflow sources are needed to evaluate this possibility.

TABLE 1

STRUCTURE FUNCTION PARAMETERS

Source	log a	b	Range (pc)	λ' (pc)	b' (Kolmogoroff)
L1529	−0.53±0.02	0.30±0.02	0.04−0.80	2.5	0.75 (λ=0.1 pc) 0.63 (λ=0.8 pc)
L1534	−0.38±0.03	0.55±0.03	0.04−0.70	2.5	0.75 (λ=0.1 pc) 0.63 (λ=0.8 pc)
Orion	−0.32±0.02	0.60±0.02	0.14−30.0	10	0.78 (λ=0.2 pc) 0.43 (λ = 30 pc)
S140	−0.20±0.03	0.43±0.04	0.26−8.0	7	0.76 (λ=0.25 pc) 0.52 (λ=8 pc)

REFERENCES

Bally, J., and Lada, C.J. 1983, Ap.J., 265, 824.

Bally, J., and Lane, A.P. 1982, Ap.J., 257, 612.

Barral, J.F., and Canto, J. 1981, Rev. Mexicana Astron.Astrof., 5, 101.

Bash, F., Hausman, M., and Papaloizou, J. 1981, Ap.J., 245, 92.

Beckwith, S., Natta, A., Salpeter, E.E. 1983, Ap.J., 267, 596.

Calvet, N., Canto, J., and Rodriguez, L.F. 1983, Ap.J., 268, 739.

Canto, J., Rodriguez, L.F., Barral, J.F., and Carral, P. 1981, Ap.J., 244, 102.

Casoli, F., and Combes, F. 1982, Astr.Ap., 110, 287.

Chernoff, D.F., Hollenbach, D.J., and McKee, C.F. 1982, Ap.J.(Letters), 259, L97.

Cohen, M., and Kuhi, L.V. 1979, Ap.J.Suppl., 41, 743.

Edwards, S., and Snell, R.L. 1982, Ap.J., 261, 151.

Edwards, S., and Snell, R.L. 1983, Ap.J.(in press July 15).

Fleck, R. 1980, Ap.J., 242, 1019.

Fleck, R. 1981, Ap.J.(Letters), 246, L151.

Fleck, R., and Clark, F.O. 1981, Ap. J., 245, 898.

Frerking, M.A., and Langer, W.D. 1982, Ap.J., 256, 523.

Gilden, D.L. 1982, unpublished Ph.D. thesis, University of Texas at Austin.

Hoyle, F. 1953, Ap.J., 118, 513.

Hunter, C. 1962, Ap.J., 135, 594.

Kaplan, S.A. 1958, in IAU Symposium No. 6: Electromagnetic

Phenomena in Cosmical Physics (Cambridge: University Press), p. 504.

Kaplan, S.A. 1966, Interstellar Gas Dynamics, (Oxford: Pergamon).

Kaplan, S.A., and Klimishin, I.A. 1964, Sov. Astr. A.J., 8, 210.

Kaplan, S.A., and Pikelner, S.B. 1970, The Interstellar Medium, (Cambridge: Harvard University Press).

Kolmogoroff, A.N. 1941, C.R. Acad.Sci. USSR, 30, 301.

Konigl, A. 1982, Ap.J., 261, 115.

Lada, C.J., and Gautier, T.N. 1982, Ap.J., 261, 161.

Landau, L.D., and Lifshitz, E.M. 1959, Fluid Mechanics, (Oxford: Pergamon).

Larson, R.B. 1981, M.N.R.A.S., 194, 809.

Leung, C.M., Kutner, M.L., and Mead, K.N. 1982, Ap.J., 262, 583.

Lichten, S.M. 1982a, Ap.J., 253, 593.

Lichten, S.M. 1982b, Ap.J.(Letters), 255, L119.

Loren, R.B. 1981, Ap.J., 249, 550.

Mckee, C.F., and Hollenbach, D.J. 1980, Ann.Rev.Astron.Ap., 18, 219.

Munch, G. 1958, Rev.Mod.Phys., 30, 1035.

Myers, P.C. 1983, Ap.J., 270, 105.

Myers, P.C., Ho, P.T.P., Schneps, M.H., Chin, G., Pankonin, V., and Winnberg, A. 1978, Ap.J., 220, 864.

Norman, C., and Silk, J. 1980, Ap.J., 238, 158.

Odgers, G.J., and Stewart, R.W. 1958, Rev.Mod.Phys., 30, 1017.

Plambeck, R.L., Snell, R.L., and Loren, R.B. 1983, Ap.J., 266, 321.

Pumphrey, W.A., and Scalo, J.M. 1983, Ap.J., 269, 531.

Reif, F. 1965, Fundamentals of Statistical and Thermal Physics, (N.Y.: McGraw-Hill).

Rodriguez, L.F., Carral, P., Ho, P.T.P., and Moran, J. 1982, Ap.J., 260, 635.

Scalo, J.M. 1983, Ap.J.(submitted).

Scalo, J.M., and Pumphrey, W.A. 1982, Ap.J.(Letters), 258, L29.

Schwartz, P.R., Waak, J.A., and Smith, H.A. 1983, Ap.J.(Letters), 267, L109.

Serkowski, K. 1958, Acta Astronomica, 8, 135.

Shull, J.M., and Hollenbach, D.J. 1978, Ap.J., 220, 525.

Simon, T., and Joyce, R.R. 1983, Ap.J., 265, 864.

Solomon, P.M., Huguenin, G.R., and Scoville, N.Z. 1981, Ap.J.(Letters), 245, L19.

Spitzer, L. 1978, Physical Processes in the Interstellar Medium, (N.Y.: John Wiley and Sons).

Taylor, G.I. 1935, Proc.Roy.Soc. A, 151, 421.

Taylor, G.I. 1938a, Proc.Roy.Soc. A, 164, 15.

Taylor, G.I. 1938b, Proc.Roy.Soc. A, 164, 476.

Vinnichenko, N.K., Pinus, N.Z., and Shmeter, S.M. 1973, Turbulence in the Free Atmosphere (N.Y.: Plenum Pub. Corp.).

Von Hoerner, S. 1951, Zs.f.Astroph., 30, 17.

Von Weizacker, C.F. 1951, Ap.J., 114, 165.

Woolfson, M.M. 1978, in The Origin of the Solar System, ed. S.F. Dermott (New York: Interscience), p. 163.

FIGURE CAPTIONS

Figure 1.-Structure functions, $S(\lambda)$, plotted logarithmically as filled circles for a) L1529, b) L1534, c) Orion, and d) S140, where λ is the spatial lag in pc. In Orion, the circled dots are structure functions based on Columbia large-scale, coarse-resolution data, while the filled circles are based on high-resolution maps of NGC 2071 and 2068 in the northeast section of the Orion molecular cloud complex. Solid lines represent least-squares fitted solutions to $\log S(\lambda) = a + b\log \lambda$. The slope of each line, b, is shown. Dashed lines are theoretical appearence for classical turbulence which obeys the Kolmogoroff law, and expected values of the slope are indicated in parentheses for various values of λ. At very large scales ($\log \lambda > 2$), the Kolmogoroff slope approaches the value of 1/3, while at very small scales, it tends to a value of 5/6. The observed slopes are generally less steep, suggestive of higher velocity dispersion at small scales than predicted by the Kolmogoroff theory of turbulence. Note that in Orion, at large scales, the observed slope is more steep than the Kolmogoroff value.

Figure 2.-Geometry corresponding to observation of an optically thin line through a molecular cloud of total extent L (see text). It would be optimal to determine the velocity difference between points X and Y. In practice, an antenna with beam θ_B is pointed at positions A and B; the velocities measured are actually averaged along columns through the cloud in the directions s.

Figure 3.-Different levels of molecular cloud fragmentation are drawn schematically. Darker shades indicate higher gas density. a) A giant molecular cloud complex of size ~ 75 pc. b) A smaller molecular cloud of size ~ 10 pc contains still smaller, denser fragments several pc in size. c) Effects of young stellar objects' high velocity outflows are depicted, showing bipolar cavities and compressed, dense clumps near shock fronts which form when outflowing material impacts ambient molecular cloud. d) More detailed cross-sectional view of a bipolar outflow containing de Laval nozzles (cf. Konigl 1982). Compressed gas near working surfaces of outflowing streams contain dense, clumped fragments.

Figure 4.-Observational evidence for a bipolar outflow-created cavity in the NGC 2071 cloud core: integrated ^{13}CO and C^{18}O intensities, which are proportional to the line of sight column densities, markedly decrease at the location of the high velocity bipolar outflow. HC$_3$N 9-8 and 11-10 emission was searched for over this region and was detected only at the indicated positions, showing that dense ($n > 10^5$ cm^{-3}) gas is associated with the HVO source. The decrease in CO column density and association of HC$_3$N emission with the HVO source is consistent with the model described in the text; the HVO creates a cavity and highly compresses molecular gas in the vicinity.

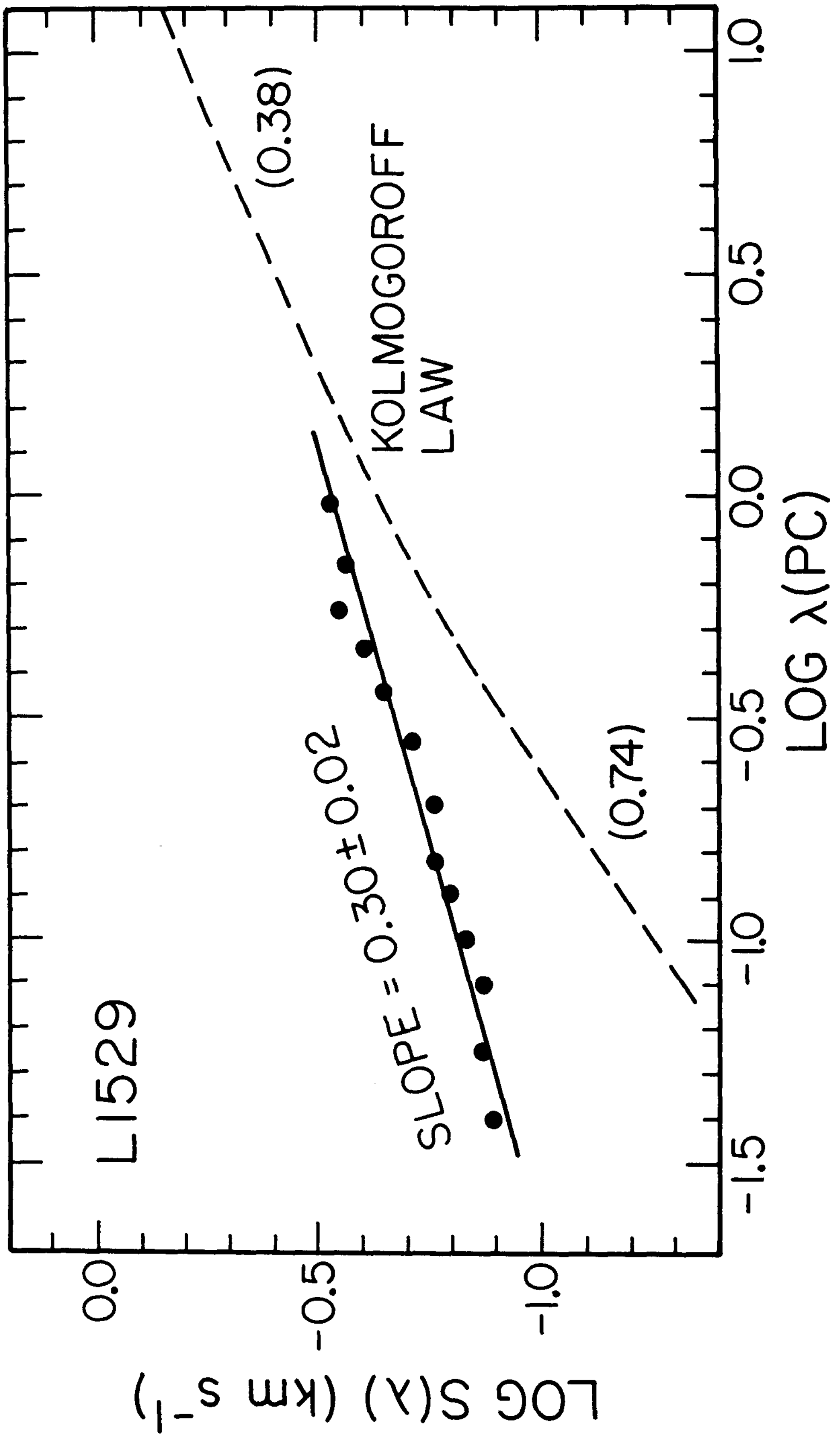
L1529
SLOPE = 0.30 ± 0.02
KOLMOGOROFF LAW
(0.38)
(0.74)
LOG λ(PC)
LOG S(λ) (km s^{-1})
−1.5
−1.0
−0.5
0.0
0.5
1.0
0.0
−0.5
−1.0

Figure 1a

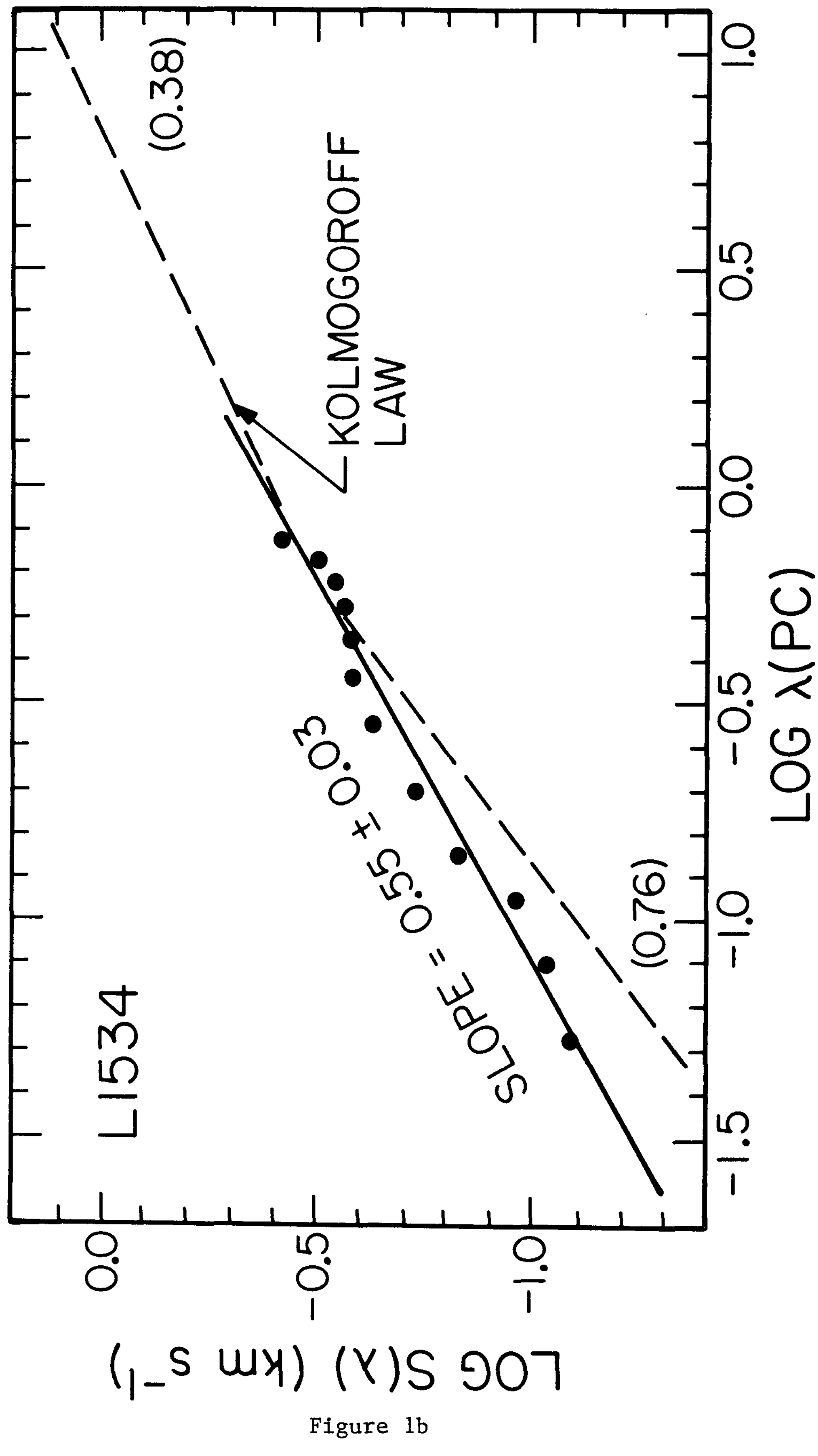
L1534
SLOPE = 0.55 ± 0.03
KOLMOGOROFF LAW
(0.38)
(0.76)
LOG λ(PC)
-1.5
-1.0
-0.5
0.0
0.5
1.0
LOG S(λ) (km s^{-1})
0.0
-0.5
-1.0

Figure 1b

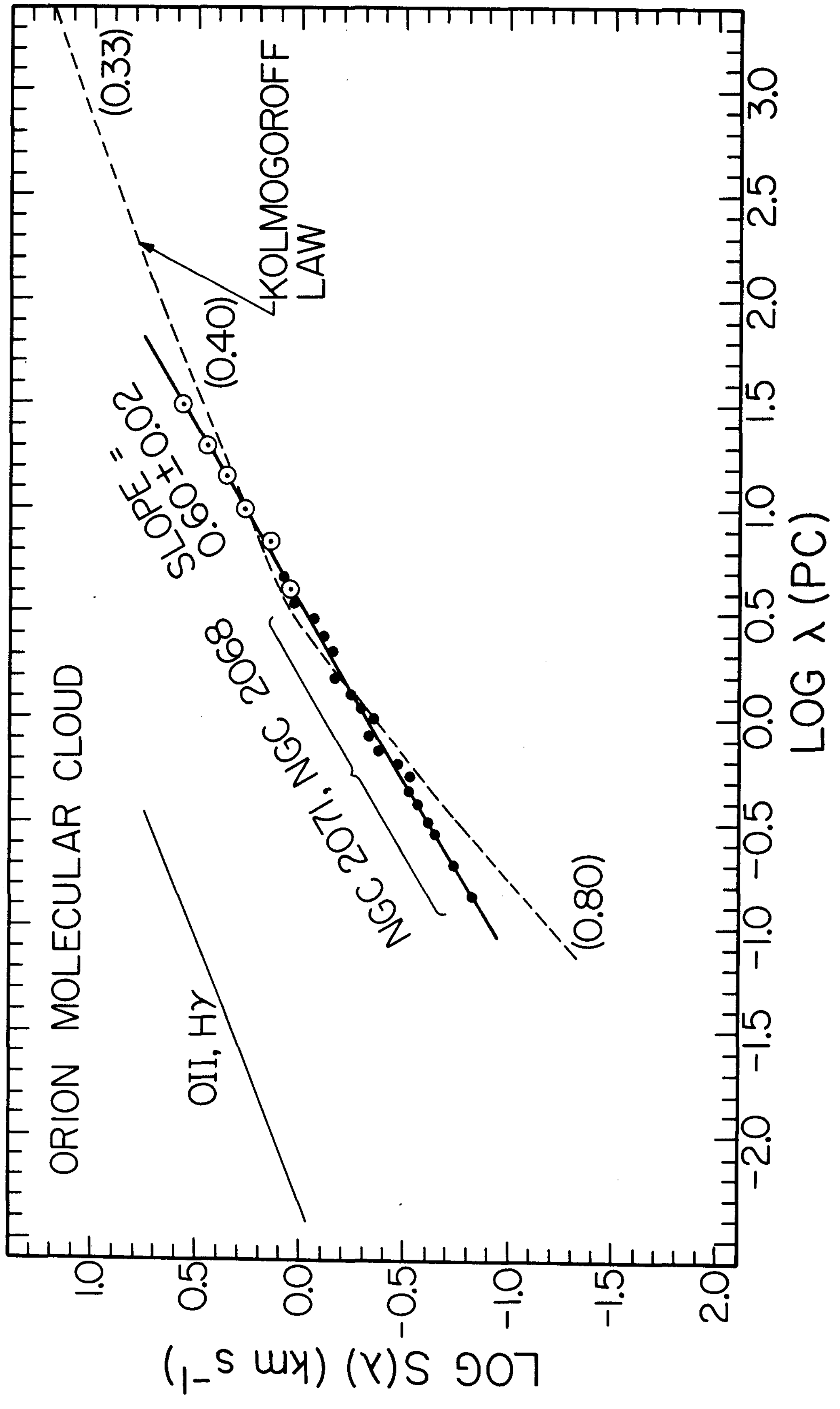
ORION MOLECULAR CLOUD
OII, Hγ
NGC 2071, NGC 2068
SLOPE = 0.60 ± 0.02
(0.40)
(0.33)
KOLMOGOROFF LAW
(0.80)
-2.0
-1.5
-1.0
-0.5
0.0
0.5
1.0
1.5
2.0
2.5
3.0
LOG λ (PC)
1.0
0.5
0.0
-0.5
-1.0
-1.5
2.0
LOG S(λ) (km s⁻¹)

Figure 1c

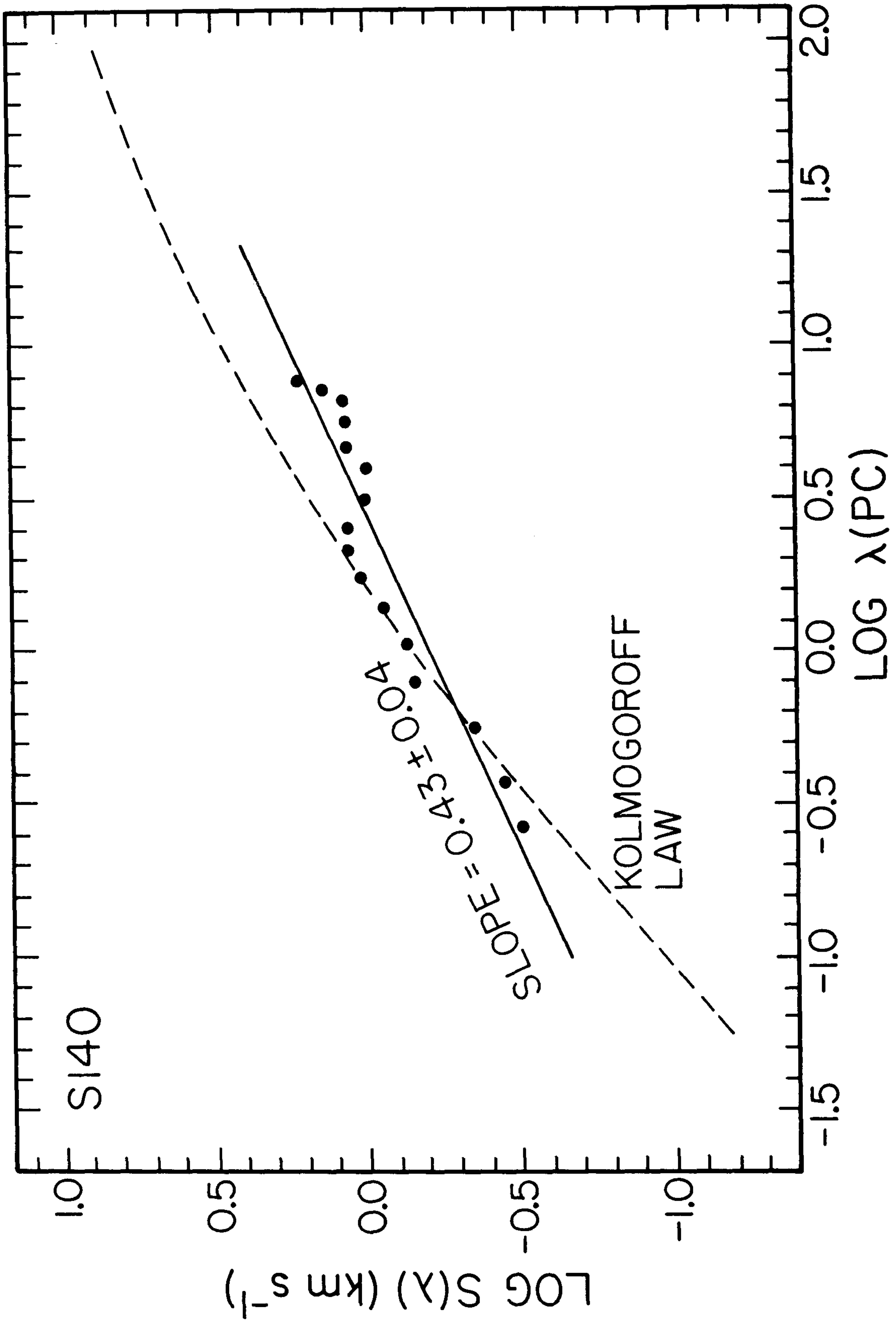
S140
SLOPE = 0.43 ± 0.04
KOLMOGOROFF LAW
LOG λ(PC)
-1.5
-1.0
-0.5
0.0
0.5
1.0
1.5
2.0
LOG S(λ) (km s^{-1})
1.0
0.5
0.0
-0.5
-1.0

Figure 1d

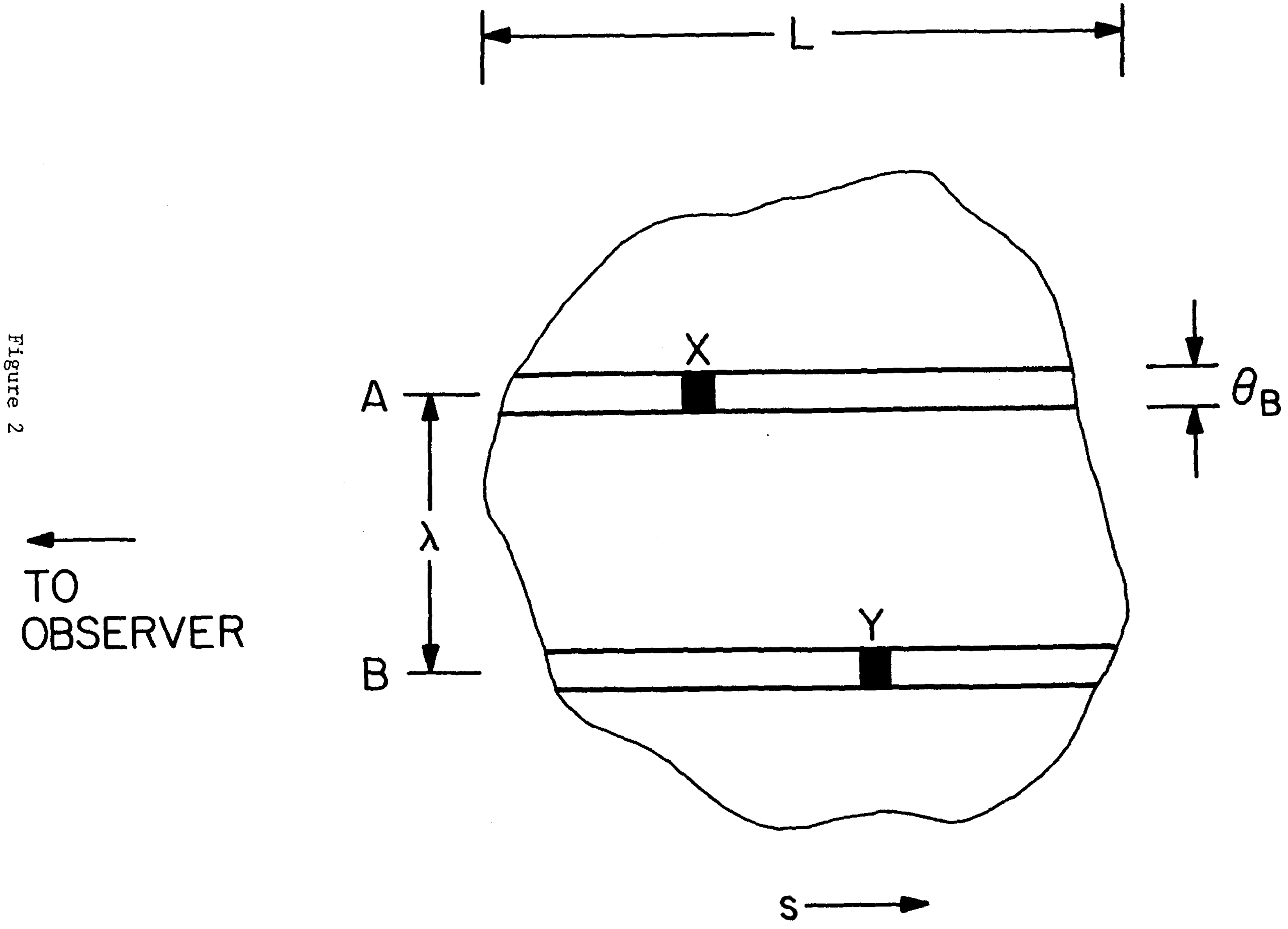

Figure 2

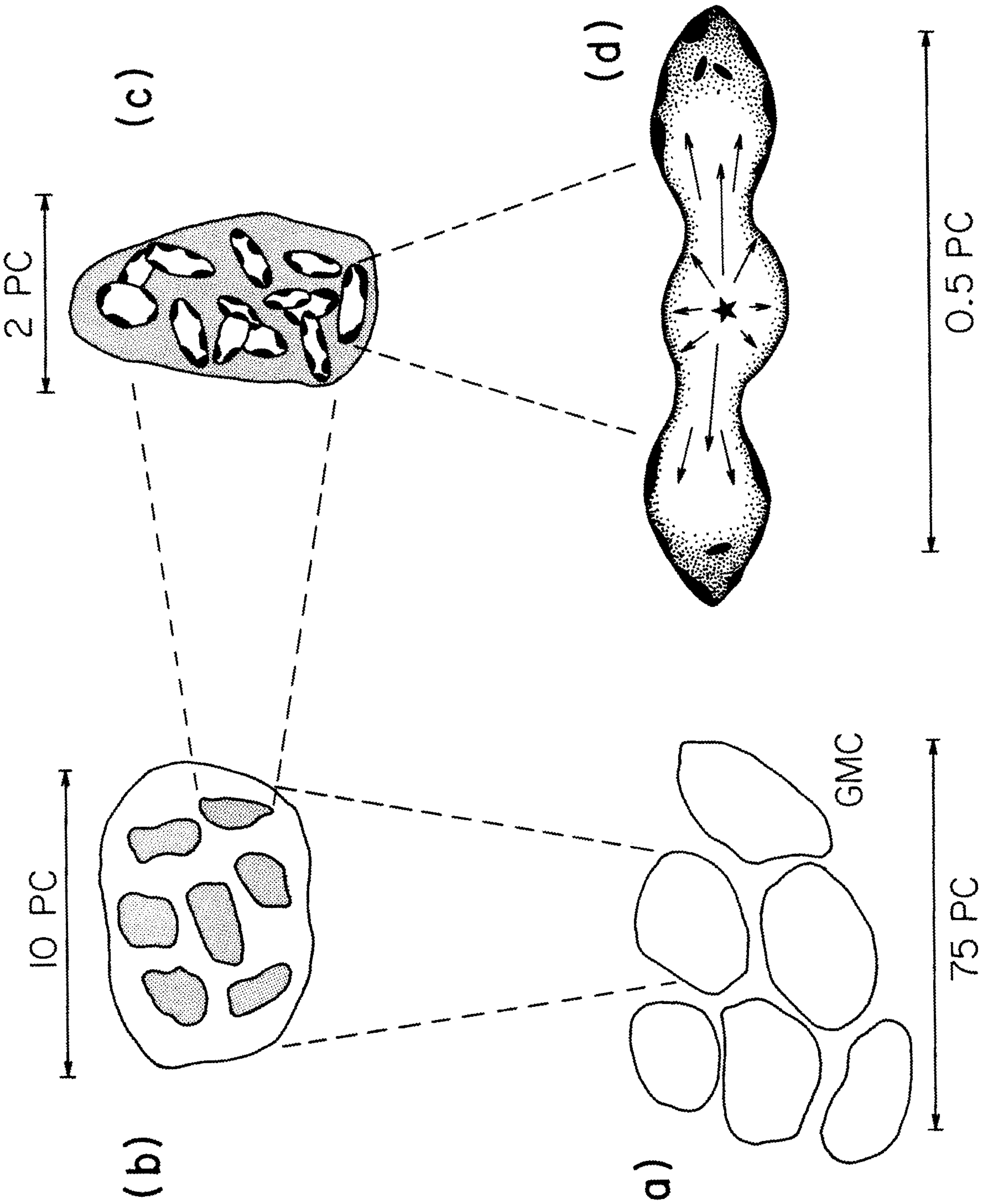

Figure 3

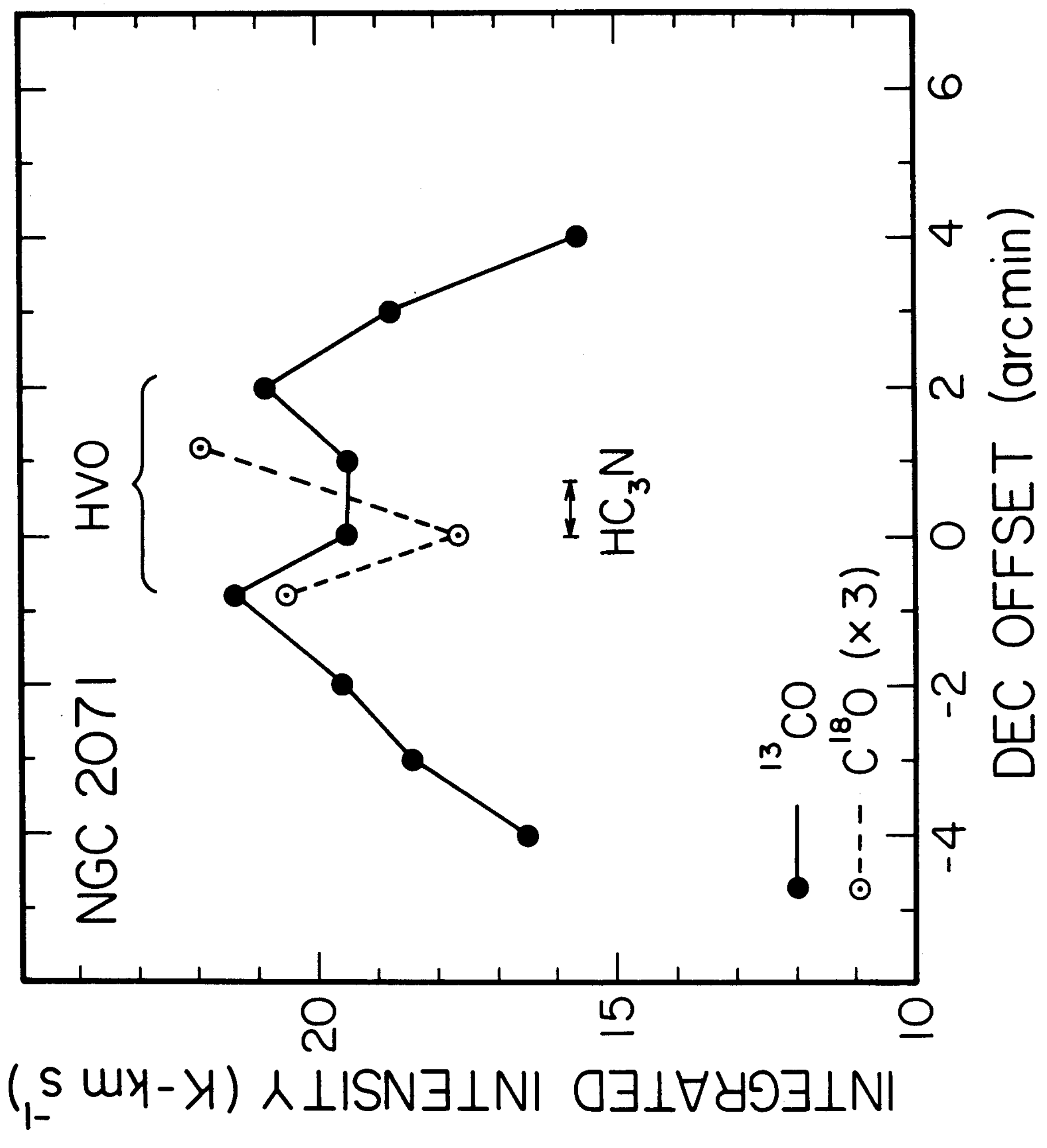
NGC 2071
HVO
HC$_3$N
^{13}CO
C^{18}O (×3)
-4
-2
0
2
4
6
DEC OFFSET (arcmin)
10
15
20
INTEGRATED INTENSITY (K-km s^{-1})

Figure 4